

# Broadband Antennas and Antenna Arrays

Guest Editors: Wenbin Dou, Zhongxiang Shen, Xiuping Li,  
and Shaoqiu Xiao





---

# **Broadband Antennas and Antenna Arrays**

International Journal of Antennas and Propagation

---

## **Broadband Antennas and Antenna Arrays**

Guest Editors: Wenbin Dou, Zhongxiang Shen, Xiuping Li,  
and Shaoqiu Xiao



---

Copyright © 2014 Hindawi Publishing Corporation. All rights reserved.

This is a special issue published in "International Journal of Antennas and Propagation." All articles are open access articles distributed under the Creative Commons Attribution License, which permits unrestricted use, distribution, and reproduction in any medium, provided the original work is properly cited.

## Editorial Board

Mohammad Ali, USA  
Jaume Anguera, Spain  
Charles Bunting, USA  
Felipe Cátedra, Spain  
Dau-Chyrh Chang, Taiwan  
Deb Chatterjee, USA  
Z. N. Chen, Singapore  
Michael Y. W. Chia, Singapore  
Shyh-Jong Chung, Taiwan  
Lorenzo Crocco, Italy  
Tayeb A. Denidni, Canada  
Francisco Falcone, Spain  
Miguel Ferrando Bataller, Spain  
Vincenzo Galdi, Italy  
Wei Hong, China  
Tamer S. Ibrahim, USA  
Nemai Karmakar, Australia

Se-Yun Kim, Republic of Korea  
Ahmed A. Kishk, Canada  
Selvan T. Krishnasamy, India  
Ju-Hong Lee, Taiwan  
Byungje Lee, Republic of Korea  
Joshua Le-Wei Li, China  
J.S. Mandeep, Malaysia  
Atsushi Mase, Japan  
Giuseppe Mazarella, Italy  
C. F. Mecklenbrucker, Austria  
Mark Mirotznik, USA  
A. S. Mohan, Australia  
P. Mohanan, India  
Pavel Nikitin, USA  
Symeon Nikolaou, Cyprus  
A. D. Panagopoulos, Greece  
Matteo Pastorino, Italy

M. Pieraccini, Italy  
Sembiam R. Rengarajan, USA  
Ahmad Safaai-Jazi, USA  
S. Safavi-Naeini, Canada  
M. Salazar-Palma, Spain  
Stefano Selleri, Italy  
Zhongxiang Shen, Singapore  
John J. Shynk, USA  
Seong-Youp Suh, USA  
Parveen Wahid, USA  
Yuanxun Ethan Wang, USA  
Tat Soon Yeo, Singapore  
Young Joong Yoon, Korea  
Jong-Won Yu, Republic of Korea  
Anping Zhao, China

# Contents

**Broadband Antennas and Antenna Arrays**, Wenbin Dou, Zhongxiang Shen, Xiuping Li, and Shaoqiu Xiao  
Volume 2014, Article ID 307304, 2 pages

**Miniaturized Wideband Aperture Coupled Microstrip Patch Antenna by Using Inverted U-Slot**,  
Amandeep Singh and Surinder Singh  
Volume 2014, Article ID 306942, 7 pages

**Broadband Loop Antenna on Soft Contact Lens for Wireless Ocular Physiological Monitoring**,  
Ssu-Han Ting, Bo-Ming Jeng, Wen-Shan Chen, Jin-Chern Chiou, and Ching-Hsing Luo  
Volume 2014, Article ID 952746, 7 pages

**A Low-Profile WLAN Antenna with Inductor and Tuning Stub for Broadband Impedance Matching**,  
Woo-Su Kim, Sunho Choi, and Gye-Taek Jeong  
Volume 2014, Article ID 452160, 6 pages

**Radiation Efficiency Improvement Method for Multifeed Circular Polarization Antenna Array with Mutual Coupling Effect**, Zijian Xing, Ling Wang, Jianying Li, and Kun Wei  
Volume 2014, Article ID 241846, 10 pages

**Suppression of Cross-Polarization of the Microstrip Integrated Balun-Fed Printed Dipole Antenna**,  
Huang Jingjian, Zhang Xiaofa, Xie Shaoyi, Wu Weiwei, and Yuan Naichang  
Volume 2014, Article ID 765891, 8 pages

**A New Agile Radiating System Called Electromagnetic Band Gap Matrix Antenna**, Hussein Abou Taam,  
Moustapha Salah Toubet, Thierry Monediere, Bernard Jecko, and Mohammad Rammal  
Volume 2014, Article ID 342518, 7 pages

**A Broadband Conformal Phased Array Antenna on Spherical Surface**, Dan Sun, Rong Shen,  
and Xuequan Yan  
Volume 2014, Article ID 206736, 5 pages

**Application of Novel Printed Dipole Antenna to Design Broadband Planar Phased Array**,  
Jie Xu and Wenbin Dou  
Volume 2014, Article ID 946763, 5 pages

**A Stacked Microstrip Antenna Array with Fractal Patches**, Xueyao Ren, Xing Chen, Yufeng Liu, Wei Jin,  
and Kama Huang  
Volume 2014, Article ID 542953, 10 pages

## Editorial

# Broadband Antennas and Antenna Arrays

Wenbin Dou,<sup>1</sup> Zhongxiang Shen,<sup>2</sup> Xiuping Li,<sup>3</sup> and Shaoqiu Xiao<sup>4</sup>

<sup>1</sup> State Key Laboratory of Millimeter Waves, Southeast University, Nanjing 210096, China

<sup>2</sup> School of Electrical and Electronic Engineering, Nanyang Technological University, 50 Nanyang Avenue, Singapore 639798

<sup>3</sup> Beijing University of Posts and Telecommunications, Beijing 100876, China

<sup>4</sup> University of Electronic Science and Technology of China, Chengdu 610054, China

Correspondence should be addressed to Wenbin Dou; njdouwb@163.com

Received 22 May 2014; Accepted 22 May 2014; Published 12 June 2014

Copyright © 2014 Wenbin Dou et al. This is an open access article distributed under the Creative Commons Attribution License, which permits unrestricted use, distribution, and reproduction in any medium, provided the original work is properly cited.

As a key component of any wireless system, antenna plays an important role and must adapt to the rapid demand for more functionalities and high data rate of communication systems. As a result, increasing the operating bandwidth of antennas and arrays has become a research topic gaining growing attention in the past decade. Wideband or multiband antennas and arrays are also finding numerous applications in radar and sensing systems.

Broadband antennas have been studied for several decades; they may be under a different name of frequency-independent antennas. Typical broadband antennas include log-periodic antenna, spiral antenna, and complementary antennas. However, most of these existing broadband antennas are nonplanar and may not be directly mounted on a metallic platform. On the other hand, many new technologies emerged in the recent years, such as system in chip and system on package that may be based on LTCC, Si, GaAs, and other substrates and used in various radar, communication, and sensor systems. For such emerging technologies, planar antennas and antennas in package are preferred solutions for realizing a compact radio system. However, broadband antennas required by these emerging systems cannot be implemented using log-periodic antenna or spiral antenna. New antenna structures and design methodologies must be proposed to achieve broadband operation with a compact size. Furthermore, different radio systems may have different specifications, which may employ different antennas and arrays to meet the system requirements.

This special issue provides a platform for researchers around the world to present their research findings and achievements in the design of broadband antennas or broadband antenna arrays. For this issue 18 manuscripts were

received, and after the rigorous review process 9 papers have been recommended for publication.

Enhancing the bandwidth of phased arrays is an interesting and important topic and two papers are concerned with this bandwidth issue. J. Xu and W. Dou's paper adopts a novel printed dipole to achieve broadband performance, while D. Sun et al.'s paper studies conformal phased array on a spherical surface.

The radiation efficiency of multifeed circularly polarized antenna array will deteriorate due to the mutual coupling between different feeds. Z. Xing et al.'s paper deals with the problem of how to improve the radiation efficiency of such multifeed antenna arrays.

Microstrip integrated balun-fed printed dipole antenna is widely used in communication and radar systems due to its suitability for integration with other circuit modules. However, its cross-polarization levels (about  $-20$  dB) may be high for some application. H. Jingjian et al.'s paper describes a method to suppress the cross-polarization to  $-35$  dB.

Microstrip patch antenna array has been extensively studied for many years because of its many attractive features. It is well known that the bandwidth of microstrip antennas is inherently narrow. Much effort has been made to increase the bandwidth of microstrip arrays in the past. X. Ren et al.'s paper employs Giuseppe Peano fractal antenna array to improve the bandwidth. And A. Singh and S. Singh's paper describes another approach based on aperture coupled inverted U-slot patch antenna with small steps at the edges.

A new agile antenna system named as electromagnetic band gap (EBG) matrix antenna is presented in H. Abou Taam et al.'s paper. EBG antennas can potentially enhance the directivity of a single source and realize beam-forming

capability, dual-band operation, bandwidth enhancement, and polarization diversity.

New antenna designs suitable for WLANs are gaining growing attention because the limited space available for the antenna poses a trade-off between bandwidth and radiation efficiency of the antenna. W.-S. Kim et al.'s paper presents a low-profile multiband antenna suitable for WLANs, using a chip inductor and tuning stub for broadband impedance matching.

S.-H. Ting et al.'s paper describes a novel loop antenna exhibiting broadband characteristics suitable for wireless ocular physiological monitoring systems. The proposed antenna may also be potentially useful for soft contact lens and communications within MEMS.

For the topic of broadband antennas and antenna arrays, though this special issue provides only a small portion of relevant research work, it will definitely benefit researchers working on similar topics. It is our hope that the proposed antenna structures and the addressed issues may inspire more researchers to work on these problems and come up with new and innovative ideas to design better antennas and arrays with wider bandwidth in the near future.

*Wenbin Dou  
Zhongxiang Shen  
Xiuping Li  
Shaoqiu Xiao*

## Research Article

# Miniaturized Wideband Aperture Coupled Microstrip Patch Antenna by Using Inverted U-Slot

Amandeep Singh<sup>1</sup> and Surinder Singh<sup>2</sup>

<sup>1</sup> Department of ECE, CT Institute of Engineering Management & Technology, Jalandhar, India

<sup>2</sup> Department of ECE, Sant Longowal Institute of Engineering and Technology, Longowal 148106, India

Correspondence should be addressed to Surinder Singh; [surinder\\_sodhi@rediffmail.com](mailto:surinder_sodhi@rediffmail.com)

Received 13 October 2013; Revised 3 February 2014; Accepted 12 February 2014; Published 4 May 2014

Academic Editor: Shaoqiu Xiao

Copyright © 2014 A. Singh and S. Singh. This is an open access article distributed under the Creative Commons Attribution License, which permits unrestricted use, distribution, and reproduction in any medium, provided the original work is properly cited.

This paper presents a linear polarized aperture coupled inverted U-slot patch antenna with small steps at the edges. The proposed design exhibits wideband behavior, acceptable return loss, VSWR, gain, small size, and less complexity. The theoretical analysis is based on the finite element method (FEM). This design has wide bandwidth, good return loss, VSWR, and radiation characteristics by implanting the inverted U-shaped stepped slots on a single aperture coupled patch. The proposed antenna design shows the measured return loss within acceptable range throughout the band (11.08 GHz–13.25 GHz) and maximum return loss is achieved with proper impedance matching. In this paper, the design considerations are presented and results are validated by the calculated and measured parameters.

## 1. Introduction

The microstrip patch antenna has been popularized because it is being utilized in many modern communication systems for its tremendous characteristics such as light weight, small size, low cost and easy fabrication [1, 2]. Pozar [3] has proposed the aperture coupled microstrip antenna first time in 1985. The title aperture coupled is assigned to the antenna as per its different feeding mechanism in which there is no galvanic contact between the patch antenna and feedline. The aperture is usually providing the magnetic coupling between antenna and feedline and exhibits numerous advantages. For instance, the spurious feed radiation can be reduced up to a specified level or eliminated by introducing a ground plane between the patch and feedline. Recently, the aperture coupled microstrip antenna attracted much attention of the researchers [4–6]. However, further investigations should be carried on to enhance the gain and bandwidth of this kind of antenna for the practical applications. The performance parameters of the proposed design are to be achieved by aperture couple feeding mechanism and implanting inverted

U-shaped slotted structure stepped at the corners and dimensions of the aperture slot. The resonant frequencies at different return losses throughout the band can be achieved by varying the dimensions of the slots as well as stub length of the feedline. Several antenna parameters are analyzed with the full wave analysis by using transmission line model. In recent times, a lot of research has been proposed for the advancement of the aperture coupled antennas as Ku band  $16 \times 16$  aperture coupled array was presented by Song and Bialkowski in 1998 [7], Gao et al. proposed a broadband dual-polarized microstrip patch antenna with aperture coupling in 2003 [8] and Wong and Tung [9] demonstrated an inverted U-shaped patch antenna for compact operation in 2003. In 2004, Rao and Johnston [10] proposed a modified aperture coupled microstrip antenna in which they employed a back cavity to block radiations from the slot. In 2005, Rao et al. [11] presented a new aperture coupled microstrip slot antenna to improve the radiation performance. Sim et al. [12] experimentally studied dual-feed dual-polarized aperture coupled patch antenna with low cross-polarization and high isolation structure in 2009. In 2012, Qin et al. [13]

proposed an aperture coupled microstrip antenna with corrugated ground plane in which they demonstrated the gain enhancement and radiation pattern. Our proposed antenna design is simple in construction as compared to [13, 14], miniaturized (7.40 mm × 6.03 mm) in size, low cost and increase in bandwidth [6, 12]. Therefore, in the present work, the design considerations are presented and results are validated by numerical simulations.

## 2. Design Essentials of Aperture Coupled Microstrip Patch Antenna

Similar to electromagnetic coupling, aperture coupling is another indirect method of feeding the resonant patch. It was first proposed in 1985 for enhancement of the bandwidth of the microstrip antenna [15]. By optimizing the various parameters including the aperture dimensions, a bandwidth of nearly 15–70% has been achieved. An ACMSA (aperture coupled microstrip antenna) consists of two substrates separated by a ground plane. The top substrate contains the radiating element and the bottom substrate contains the microstrip feedline. A small aperture is cut in the ground plane to allow coupling from the open-circuited microstrip feedline to the radiating patch. The coupling aperture could be small, known as a nonresonant aperture or comparable to a half wavelength, known as a resonant aperture. The design parameters of proposed antenna are calculated by referring to the transmission line model which is detailed in two parts as Part 1 includes the standard available design parameters according to the materials opted and Part 2 describes the calculated design parameters as follows.

*Part 1.* Consider the following:

- patch substrate material used: RT/Duroid 5880;
- feed substrate material used: RT/Duroid 6006;
- thickness of the patch substrate (standard):  $h = 1.575$  mm;
- thickness of the feed substrate (standard):  $h = 0.635$  mm;
- relative permittivity of patch substrate:  $\epsilon_{rp} = 2.2$ ;
- relative permittivity of feed substrate:  $\epsilon_{rf} = 6.15$ ;
- thickness of the patch:  $t = 0.0175$  mm;
- design frequency of the proposed antenna: 11.4 GHz.

*Part 2.* Consider the following:

- length of the patch:  $L_p = 7.962$  mm;
- width of the patch:  $W_p = 6.458$  mm;
- effective dielectric constant of patch substrate:  $\epsilon_{\text{reff}(P)} = 1.9028$ ;
- ground plane (length = width  $\sim 2\lambda_o$ ) [16, 17]: 53 mm × 53 mm;
- feedline length:  $L_f = 26.5$  mm;
- feed width to height ratio:  $W_f/h_f = 1.57$ ;

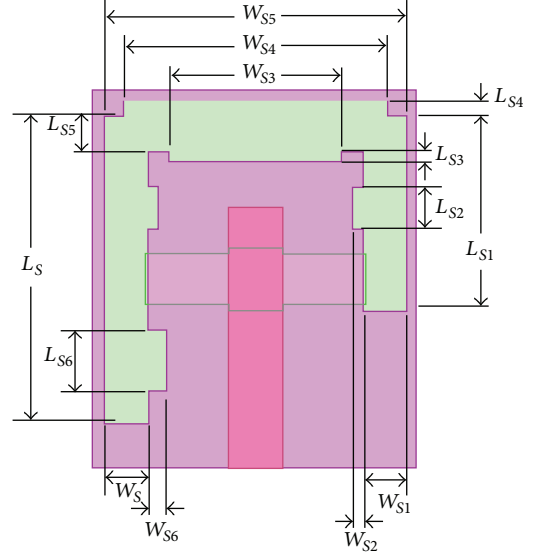


FIGURE 1: Geometry of the proposed aperture coupled patch antenna with inverted U-slot.

feedline width [18]:  $W_f = 1$  mm;

effective dielectric constant of feed substrate:  $\epsilon_{\text{reff}(f)} = 4.427$ ;

theoretical characteristic impedance [19, 20]:  $Z_o = 48.44 \Omega$ ;

aperture length:  $A_L = 4.1$  mm;

Aperture width:  $A_W = 1$  mm;

Stub length:  $L_s = 1.6$  mm.

## 3. Proposed Aperture Coupled Patch Antenna Configuration

The architecture of the aperture coupled microstrip patch antenna embedded with inverted U-slot and small tuning stubs is represented in Figure 1. The dimensions of the aperture slot and feedline are clearly represented in Figure 2. The dimensions of the radiating structures, aperture slot, and microstrip feedline are chosen according to [2]. The dimensions of inverted U-slot with small tuning stubs on it are adjusted to radiate apparently around the resonant frequency and their position is selected so that the radiating structure must be capable of producing wider bandwidth and proper impedance matching.

Moreover, the dimensions of the aperture slot and the size of the feedline stub are responsible for the proper impedance matching between the microstrip feedline and the radiating patch. It is important to discuss here that if the coupling between the feedline and radiating structure is not achieved, most of the fed signals will be reflected which results in the performance deterioration.

The length and width of the radiating patch are finite, and consequently the radiated fields at the radiating edges of the antenna experience fringing. Fringing affects the dimensions

TABLE 1: Geometrical parameters of analyzed antenna (all dimensions in mm).

Antenna parameters	Design 1	Design 2	Design 3	Design 4	Design 5	Design 6
$L$	7.96	7.96	7.96	7.40	7.40	7.40
$W$	6.45	6.45	6.45	6.03	6.03	6.03
$L_S$	NA	6.0	6.0	6.0	6.0	6.0
$W_S$	NA	0.8	0.8	0.8	0.8	0.8
$L_{S1}$	NA	NA	3.8	NA	3.8	3.8
$W_{S1}$	NA	NA	0.8	NA	0.8	0.8
$L_{S2}$	NA	NA	NA	NA	NA	0.8
$W_{S2}$	NA	NA	NA	NA	NA	0.2
$L_{S3}$	NA	NA	NA	NA	NA	0.2
$W_{S3}$	NA	NA	NA	NA	NA	3.2
$L_{S4}$	NA	NA	NA	0.3	0.3	0.3
$W_{S4}$	NA	NA	NA	4.9	4.9	4.9
$L_{S5}$	NA	NA	NA	0.7	0.7	0.7
$W_{S5}$	NA	NA	NA	5.6	5.6	5.6
$L_{S6}$	NA	NA	NA	NA	NA	1.2
$W_{S6}$	NA	NA	NA	NA	NA	0.35
$A_W$	1.0	1.0	1.0	1.0	1.0	1.0
$A_L$	4.1	4.1	4.1	4.1	4.1	4.1
$S_W$	1.2	1.2	1.2	1.2	1.2	1.2
$S_L$	1.0	1.0	1.0	1.0	1.0	1.0

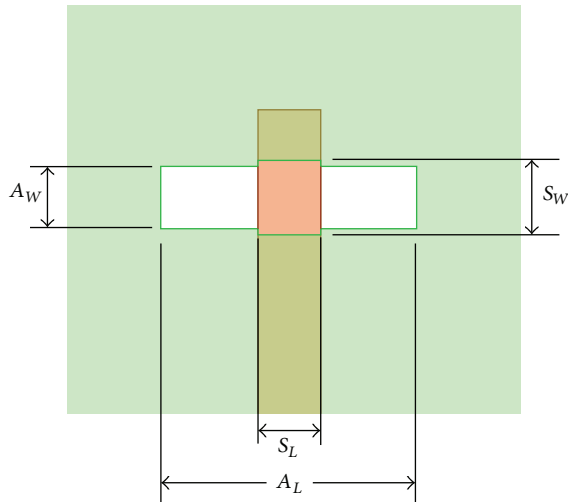


FIGURE 2: Dimensions of the aperture slot and feedline.

of patch height and dielectric constant of substrate and hence the resonant frequency. The constructional detail of the proposed antenna is shown in Figure 1; dimensions of the patch, slots, and small stubs are mentioned in Table 1. All the design parameters of the proposed antenna tabulated in Table 1 are calculated as per the transmission line model and iterative trials. As listed in Table 2, first of all, design 1 is analyzed and necessary modifications have been done in a progressive manner to achieve the final optimum designs that is design 6.

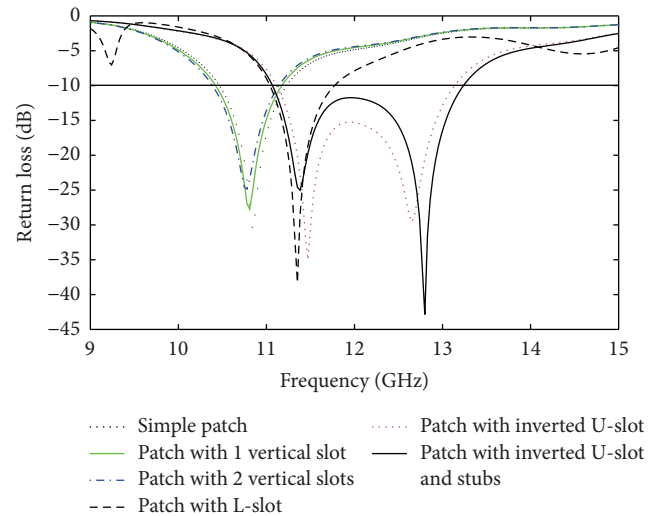


FIGURE 3: Return loss plot of all the designs in which solid black line plot represents the return loss of proposed antenna.

#### 4. Discussion of Results

Our attention is focused on the discussion and presentation of calculated and measured results for the return loss, VSWR, gain, and radiation pattern of the proposed antenna design in this section. The frequency range of 10 GHz to 14 GHz is utilized for the analysis purpose of the proposed design. Figure 3 is representing the return loss plots as per design 1 to design 6 mentioned in Table 1. We observed that simple

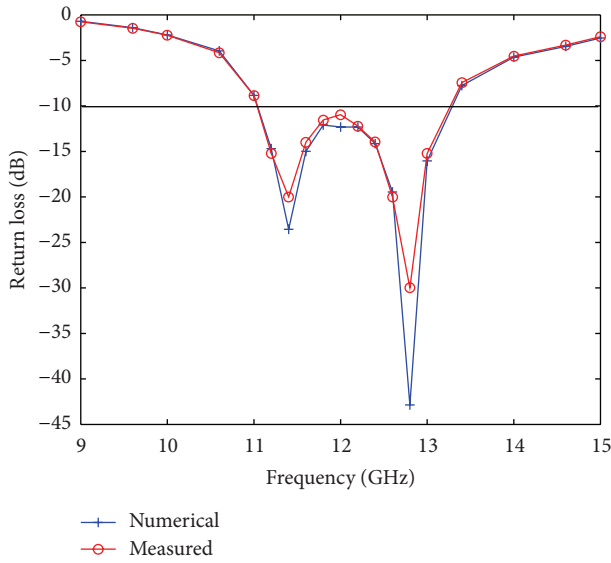


FIGURE 4: Return loss versus frequency plot of calculated and measured results of proposed antenna.

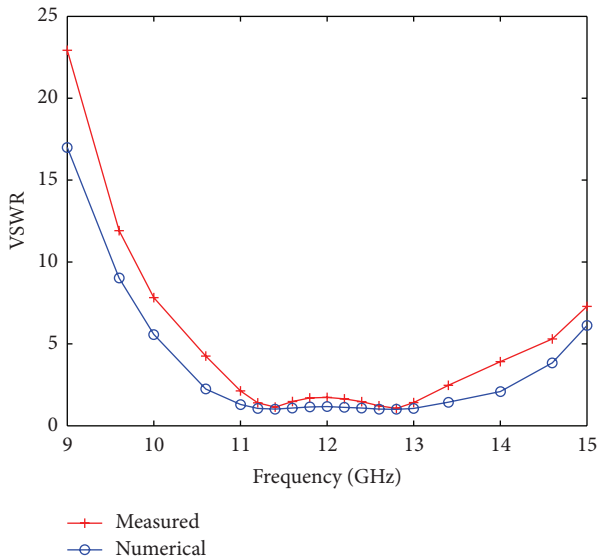


FIGURE 5: VSWR versus frequency plot of calculated and measured results of proposed antenna.

aperture coupled patch antenna (black dotted plot) exhibits  $-30$  dB return loss at  $10.84$  GHz resonant frequency and  $790$  MHz ( $10.43$  GHz to  $11.22$  GHz) absolute bandwidth.

Further improvements have been achieved in the design after applying different patterns and positions of slots as represented in Figure 1. At the very first step, design 1 of Table 1 is modified to design 2 by employing one vertical slot of length  $L_S = 6$  mm and  $W_S = 0.8$  mm on the radiating patch and we observed slight decrease in resonant frequency from  $10.84$  GHz to  $10.8$  GHz and bandwidth increases by  $10$  MHz and return loss is  $-28$  dB shown as green line

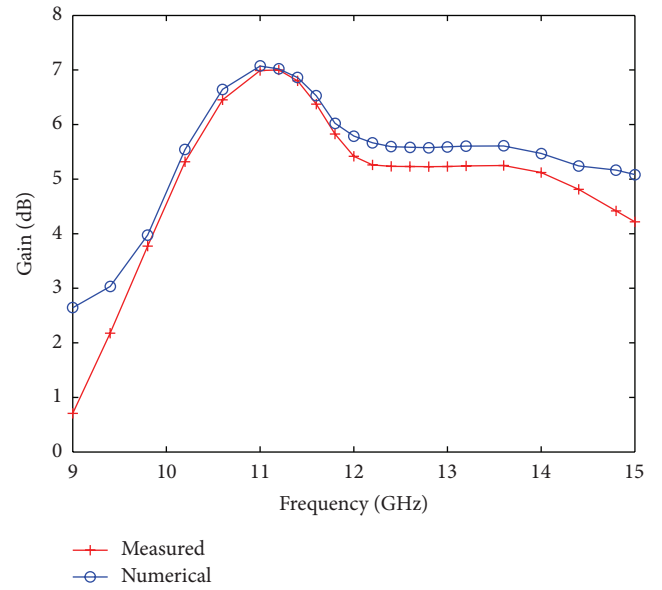


FIGURE 6: Gain versus frequency plot of calculated and measured results of proposed antenna.

TABLE 2: Description of antenna designs mentioned in Table 1.

Antenna designs	Description of designs
Design 1	Simple aperture coupled patch antenna
Design 2	Aperture coupled patch with one vertical slot
Design 3	Aperture coupled patch with two vertical slots
Design 4	Aperture coupled patch with L-slot
Design 5	Aperture coupled patch with inverted U-slot
Design 6	Aperture coupled inverted U-slot patch with 3 stubs

plot. Antenna design 2 is modified with antenna design 3 by implanting another slot on the radiating patch having dimensions  $L_{S1} = 3.8$  mm and  $W_{S1} = 0.8$  mm and observed that the resonant frequency decreases from  $10.8$  GHz to  $10.79$  GHz and bandwidth decreases to  $740$  MHz and return loss decreases to  $-25$  dB shown in Figure 5 and denoted as dash-dot line structure. The reason for this degradation is that the radiation from two vertical slots on either side of the patch is not coupled mutually because these slots are departed by the conducting patch; therefore, it decreases in bandwidth. By taking into consideration this degradation, the antenna is further improved as design 4 in which a squared truncated inverted L-slot is implanted on the patch having dimensions listed in Table 1. The result of design 4 is shown in Figure 3 and represented with the dashed line; it exhibits a drastic change in return loss which is  $-38$  dB at resonant frequency  $11.38$  GHz and the bandwidth remains unaltered that is  $800$  MHz. With these modifications in the design, we have achieved the appropriate return loss and VSWR, but the goal of bandwidth enhancement has not been achieved

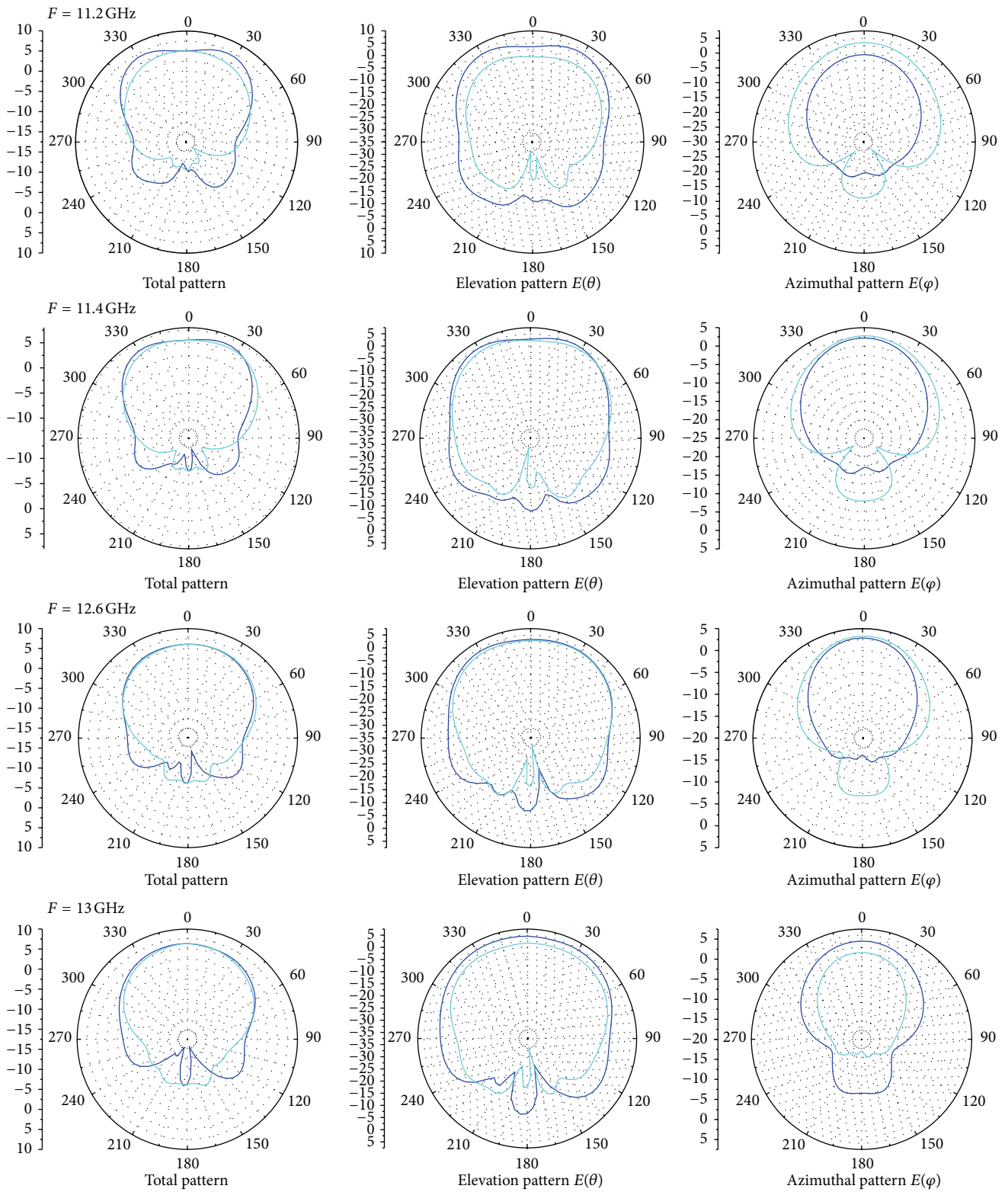


FIGURE 7: 2D radiation patterns of aperture coupled microstrip patch antenna by using inverted U-slot.

TABLE 3: Return loss, gain, and bandwidth of all the design analysed in this work.

Antenna performance	Operating frequency	Return loss	Gain	Bandwidth
Design 1	10.84 GHz	-30 dB	7 dB	790 MHz
Design 2	10.80 GHz	-28 dB	7 dB	800 MHz
Design 3	10.79 GHz	-25 dB	7.5 dB	740 MHz
Design 4	11.38 GHz	-38 dB	6.95 dB	800 MHz
Design 5	11.45 GHz	-35 dB	6.87 dB	2000 MHz
Design 6	11.45 GHz	-43 dB	6.97 dB	2170 MHz

so far. No doubt that the antennas having bandwidth more than 500 MHz can be categorized as wideband antenna, but still we will try to reach up to the considerable amount of bandwidth by improving our design. Design 5 with reference to Table 1 is another enhancement which we have reached by implanting an inverted U-slot having dimensions as per Table 1. It is found that the bandwidth has increased with this design as 2000 MHz and the return loss is below the threshold value in the frequency range of 11.11 GHz to 13.13 GHz. Utmost value of return loss is attained, -35 dB at 11.45 GHz frequency and -30 dB at 12.65 GHz frequency. Furthermore, some small stub slots are added in the inverted U-slot structure and dimensions of these slots are detailed under design 6 of Table 1. In this absolute design, we have attained 2170 MHz bandwidth (11.08 GHz–13.25 GHz) with the maximum return loss of -43 dB as undoubtedly represented in Figure 3 with solid black line plot which are the tremendous values of bandwidth and return loss so far. Further, the calculated and measured results of return loss and VSWR are presented in Figures 4 and 5, respectively. The incident power used for these measurements was 10 mW and it is observed from the measured return loss and VSWR that 92% to 99.2%.

Power is Accepted by the proposed antenna in the frequency range of 11 GHz–13.2 GHz. A radiation efficiency of 91% to 97% is achieved throughout the specified frequency range. Finally, it is observed from Figures 4 and 5 that a good agreement has been achieved between the calculated and measured return loss and VSWR values.

Figure 6 represents gain versus frequency plot through which it is undoubtedly observed that the proposed antenna design exhibits acceptable gain (5.5 dB to 6.97 dB) within the frequency range of 11 GHz–13.2 GHz.

A good agreement has also been achieved between the calculated and measured value of gain throughout the required frequency range. All the important parameters which we have discussed in the paper are tabulated in Table 3 so that they can easily be recognized and compared with each other. The VSWR values for all the designs have not been shown because all of these antenna designs exhibited a good value of VSWR which should range between 1 and 2.

It is observed from Table 3 that with antenna design 6, a good agreement amongst all the important parameters has been achieved.

The measured 2D radiation patterns at different resonant frequencies are presented in Figure 7. The radiation characteristics are also studied in azimuthal plane ( $x$ - $y$  planes) and elevation plane ( $y$ - $z$  planes) and it is observed that the

proposed antenna is radiating more in the theta ( $y$ - $z$  planes) direction and less in the phi ( $x$ - $y$  planes) direction. Normally, the radiation characteristics are determined in the far field region as a function of coordinates and it can also be classified in terms of power pattern or field pattern. Moreover, from the total patterns of all resonant frequencies, it is clear that major lobe is stronger than the back lobe and side lobes and it is analysed that this proposed antenna is radiating normally to the antenna surface.

## 5. Conclusions

The design of inverted U-slot aperture coupled wideband microstrip patch antenna is analyzed and discussed in this work. The performance parameters of the antenna as detailed in Table 3 are achieved in a good agreement after applying slight modifications to the base design to reach up to the final optimum wideband design. Moreover, the design resulted in a smaller size antenna with a wide bandwidth operation. A good agreement between calculated and measured return loss, VSWR, and gain is achieved. All the results of the proposed design are presented and discussed and it is concluded that this antenna will give the satisfactory performance in the band of operating frequencies (11 GHz–13.5 GHz).

## Conflict of Interests

The authors declare that there is no conflict of interests regarding the publication of this paper.

## References

- [1] I. J. Bahl and P. Bhartia, *Microstrip Antennas*, Artech House, Boston, Mass, USA, 1980.
- [2] C. A. Balanis, *Antenna Theory, Analysis and Design*, John Wiley & Sons, New York, NY, USA, 1997.
- [3] D. M. Pozar, "Microstrip antenna aperture coupled to a microstripline," *Electronics Letters*, vol. 21, no. 2, pp. 49–50, 1985.
- [4] S. K. Padhi, N. C. Karmakar, C. L. Law, and S. Aditya, "A dual polarized aperture coupled circular patch antenna using a c-shaped coupling slot," *IEEE Transactions on Antennas and Propagation*, vol. 51, no. 12, pp. 3295–3298, 2003.
- [5] C. H. Tsao, Y. M. Hwang, F. Kilburg, and F. Dietrich, "Aperture coupled patch antennas with widebandwidth and dual polarization capabilities," in *Proceedings of the IEEE Antennas and Propagation Symposium Digest*, pp. 936–939, 1988.

- [6] W. J. Tseng and S. J. Chung, "Analysis and application of a two-port aperture-coupled microstrip antenna," *IEEE Transactions on Microwave Theory and Techniques*, vol. 46, no. 5, pp. 530–535, 1998.
- [7] H. J. Song and M. E. Bialkowski, "Ku-Band  $16 \times 16$  planar array with aperture-coupled microstrip-patch elements," *IEEE Antennas and Propagation Magazine*, vol. 40, no. 5, pp. 25–29, 1998.
- [8] S. Gao, L. W. Li, M. S. Leong, and T. S. Yeo, "A broad-band dual-polarized microstrip patch antenna with aperture coupling," *IEEE Transactions on Antennas and Propagation*, vol. 51, no. 4, pp. 898–900, 2003.
- [9] K. L. Wong and H. C. Tung, "An inverted U-shaped patch antenna for compact operation," *IEEE Transactions on Antennas and Propagation*, vol. 51, no. 7, pp. 1647–1648, 2003.
- [10] Q. Rao and R. H. Johnston, "Modified aperture coupled microstrip antenna," *IEEE Transactions on Antennas and Propagation*, vol. 52, no. 12, pp. 3397–3401, 2004.
- [11] Q. Rao, T. A. Denidni, and R. H. Johnston, "A new aperture coupled microstrip slot antenna," *IEEE Transactions on Antennas and Propagation*, vol. 53, no. 9, pp. 2818–2826, 2005.
- [12] C. Y. Sim, C. C. Chang, and J. S. Row, "Dual-feed dual-polarized patch antenna with low cross polarization and high isolation," *IEEE Transactions on Antennas and Propagation*, vol. 57, no. 10, pp. 3321–3324, 2009.
- [13] K. Qin, M. Li, H. Xia, and J. Wang, "A new compact aperture-coupled microstrip antenna with corrugated ground plane," *IEEE Antennas and Wireless Propagation Letters*, vol. 11, pp. 807–810, 2012.
- [14] M. M. Honari, A. Abdipour, and G. Moradi, "Bandwidth and gain enhancement of an aperture antenna with modified ring patch," *IEEE Antennas and Wireless Propagation Letters*, vol. 10, pp. 1413–1416, 2011.
- [15] M. Ali, A. Kachouri, and M. Samet, "Novel method for planar microstrip antenna matching impedance," *Journal of Telecommunications*, vol. 2, pp. 131–138, 2010.
- [16] R. Garg, P. Bhartia, I. Bahl, and A. Ittipibon, *Microstrip Antenna Design Handbook*, Artech House, Boston, Mass, USA, 2001.
- [17] E. Lier and K. R. Jakobsen, "Rectangular microstrip patch antenna with infinite and finite ground plane dimensions," *IEEE Transactions on Antennas and Propagation*, vol. 31, no. 6, pp. 978–984, 1983.
- [18] H. A. Wheeler, "Transmission line properties of parallel strips separated by a dielectric sheet," *IEEE Transactions on Microwave Theory and Techniques*, vol. 13, pp. 172–185, 1965.
- [19] E. O. Hammerstadt, "Equations for microstrip circuit design," in *Proceedings of the 5th European Microwave Conference*, pp. 268–272, September 1975.
- [20] I. J. Bahl and R. Garg, "Simple and accurate formulas for microstrip with finite strip thickness," *Proceedings of the IEEE*, vol. 65, no. 11, pp. 1611–1612, 1977.

## Research Article

# Broadband Loop Antenna on Soft Contact Lens for Wireless Ocular Physiological Monitoring

Ssu-Han Ting,<sup>1</sup> Bo-Ming Jeng,<sup>1</sup> Wen-Shan Chen,<sup>2</sup>  
Jin-Chern Chiou,<sup>3</sup> and Ching-Hsing Luo<sup>1,4</sup>

<sup>1</sup> Department of Electrical Engineering, National Cheng Kung University, Tainan City 701, Taiwan

<sup>2</sup> Department of Electronic Engineering, Southern Taiwan University of Science and Technology, Tainan City 71005, Taiwan

<sup>3</sup> Department of Electronic and Computer Engineering, National Chiao Tung University, Hsinchu 30010, Taiwan

<sup>4</sup> Institute of Medical Science and Technology, National Sun Yat-sen University, Kaohsiung, 804, Taiwan

Correspondence should be addressed to Ching-Hsing Luo; robinluo@mail.ncku.edu.tw

Received 28 September 2013; Revised 9 March 2014; Accepted 9 March 2014; Published 13 April 2014

Academic Editor: Zhongxiang Shen

Copyright © 2014 Ssu-Han Ting et al. This is an open access article distributed under the Creative Commons Attribution License, which permits unrestricted use, distribution, and reproduction in any medium, provided the original work is properly cited.

This paper presents a novel loop antenna with broadband for wireless ocular physiological monitoring (WOPM). The antenna is fabricated on a thin-film poly-para-xylylene C (parylene C) substrate with a small thickness of 11  $\mu\text{m}$  and dimension of  $\pi \times 6.5 \times 6.5 \text{ mm}^2$ . With the advantage of small size, the proposed antenna is suitable to apply to the soft contact lens and transmit the signal in microelectromechanical Systems (MEMS). Because the pig's eye and human's eye have similar parameters of conductivity and permittivity, the experimental results are obtained by applying the proposed antenna on the pig's eye and cover from 1.54 to 6 GHz for ISM band (2.4 and 5.8 GHz) applications. The measured antenna radiation patterns, antenna gains, and radiation efficiency will be demonstrated in this paper, which are suitable for application of wireless ocular physiological monitoring.

## 1. Introduction

Recently, monitoring various physiological parameters with biological telemetry system has become an important research topic in wireless monitoring control. To accomplish the wireless monitoring control, the antennas implanted in human body are used to establish communication links between medical sensing devices and external instruments for short-distance biotelemetry. Eye ball monitoring system that is an application of biological telemetry system has also been studied recently, such as monitoring intraocular pressure monitoring systems [1, 2], wireless powered micro-LED display systems [3], and glucose-monitoring systems [4]. This biotelemetry system can transfer the physiological data into signal and transmit the signal to the external receiving instrument through the antenna on the contact lens. These instruments can share valuable data through the telephone system or the Internet. Through the wireless instruments, the detected physiological data can be sent regularly to the medical institution. An antenna is a key component in

the biotelemetry medical systems to transfer available data. However, the antennas used in human body are difficult to accomplish for interference and size limits. This paper presents a novel loop antenna design for WOPM applications.

## 2. Antenna Design

**2.1. Antenna Geometry.** Using the Ansoft simulation software high-frequency structure simulator (HFSSSTM), a novel broadband antenna was designed for the biotelemetry applications (ISM band 2.4 and 5.8 GHz). The geometry of the proposed antenna shown in Figure 1(a) is fabricated on the parylene C substrate with thickness of 11  $\mu\text{m}$  and permittivity of 4. Figure 1(b) shows the photograph of proposed antenna with minicable. The proposed antenna is connected on a soft contact lens with conductive epoxy glue. The overall dimension of loop antenna is  $\pi \times 6.5 \times 6.5 \text{ mm}^2$  with width of the 1 mm (W1). The parameters of the antenna are listed in Table 1.

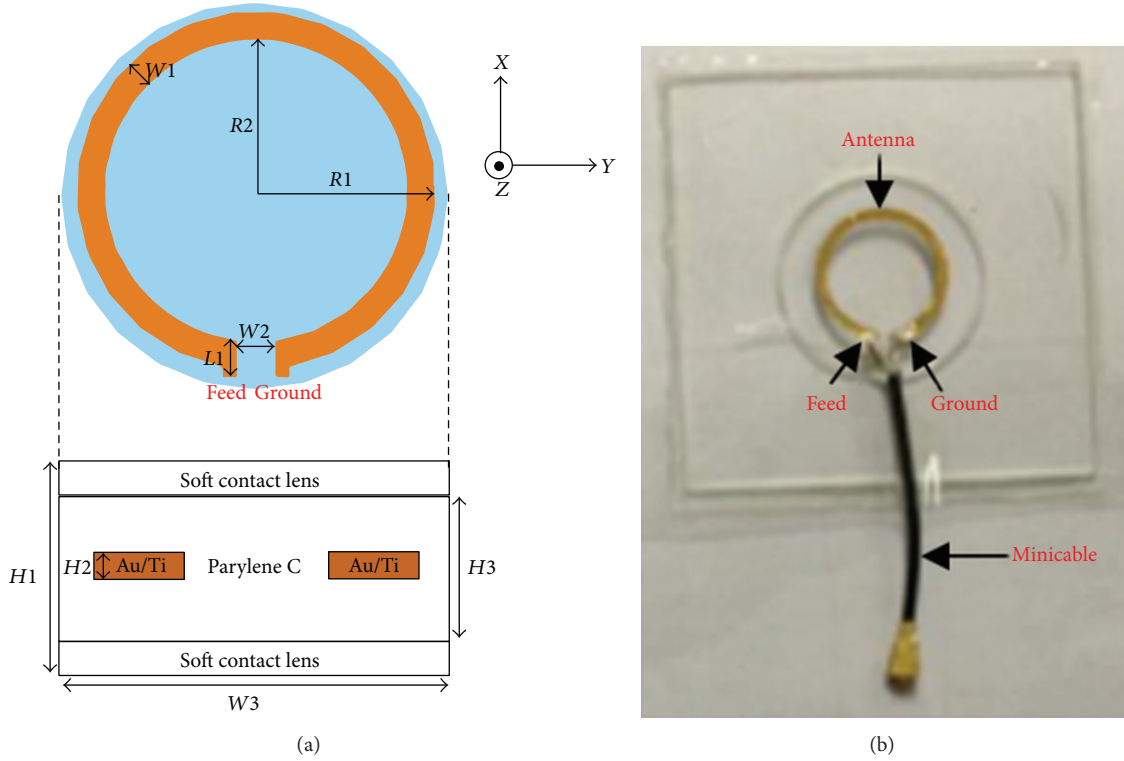


FIGURE 1: Geometry of the proposed antenna. (a) Substrate model. (b) Photograph of a fabricated antenna with minicable.

TABLE 1: Parameters of the proposed antenna.

Parameter	Unit (mm)	Parameter	Unit ( $\mu\text{m}$ )
$W1$	1	$H1$	100
$W2$	1.4	$H2$	0.38
$W3$	7	$H3$	11
$R1$	6.5		
$R2$	5.5		
$L1$	1.3		

**2.2. Comparison of Permittivity and Conductivity between Human's and Pig's Eye.** In experimental operation, pig's eye must be used to replace human's eye. Therefore, the parameters of their tissue must be verified and studied. Figure 2 presents the measurement environment of the minced pig's eye tissue on an Agilent 85070E dielectric probe kit and an 8753E network analyzer. Figure 3 shows the comparison results of permittivity and conductivity against frequency between the test tissue (pig's eye) and the reference tissue (human's eye) [5]. The results indicate that the characteristics of pig's eye are similar to human's eye and can be used to replace human's eye.

### 3. Results and Discussion

The simulated results of the proposed antenna are obtained by high frequency structure simulator (HFSS) [6] and



FIGURE 2: Minced pig's eye tissue measurement environment.

the measured results are achieved from Agilent E5071C network analyzer. In Figure 4, the measured and simulated antenna reflection coefficient ( $S_{11}$ ) of the proposed antenna demonstrates good agreement. Two resonant modes create wide operation bandwidth that can also be observed. The measured  $S_{11}$  based on  $-10$  dB standard achieves an impedance bandwidth of 4.46 GHz (from 1.54 to 6 GHz) for ISM application band. Figure 5 shows the simulated input impedance (imaginary and real parts) for the proposed antenna. From 1.75 to 6 GHz, the input impedance presents

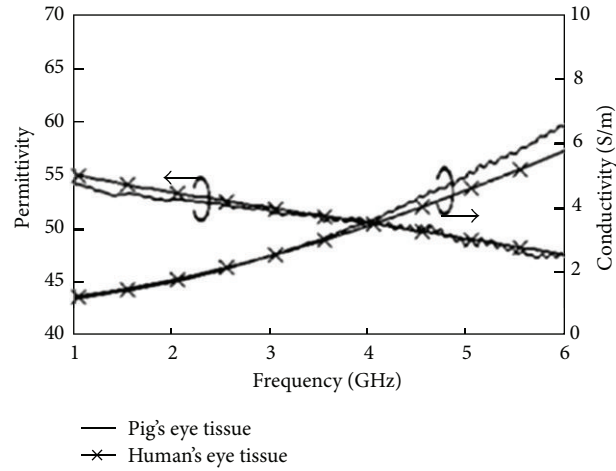


FIGURE 3: Comparing the permittivity and conductivity against frequency of the test tissue (pig's eye) and the reference tissue (human's eye).

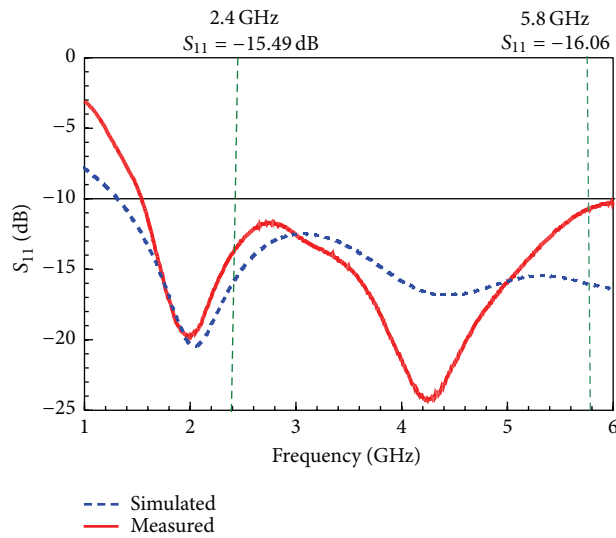


FIGURE 4: Simulated and measured return loss of the proposed antenna.

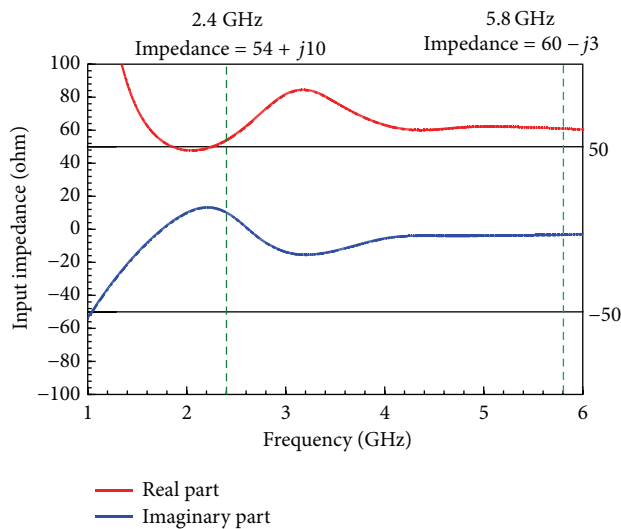


FIGURE 5: Simulated impedance of the proposed antenna.

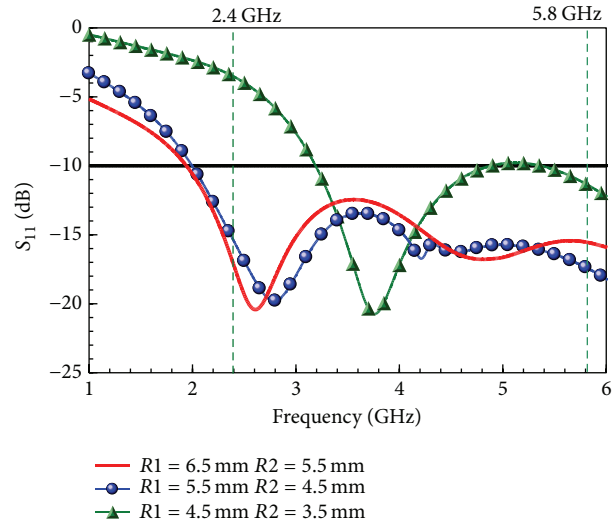


FIGURE 6: Simulated  $S_{11}$  for different loop sizes of the proposed antenna.

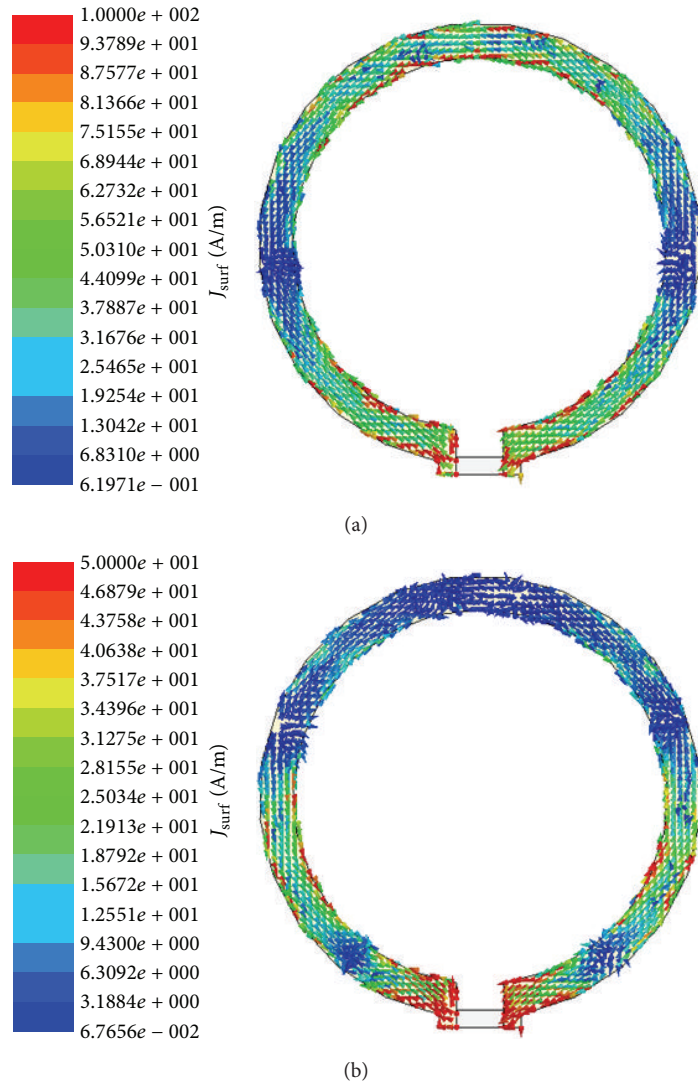


FIGURE 7: Simulated current distributions of the proposed antenna: (a) 2.4 GHz; (b) 5.8 GHz.

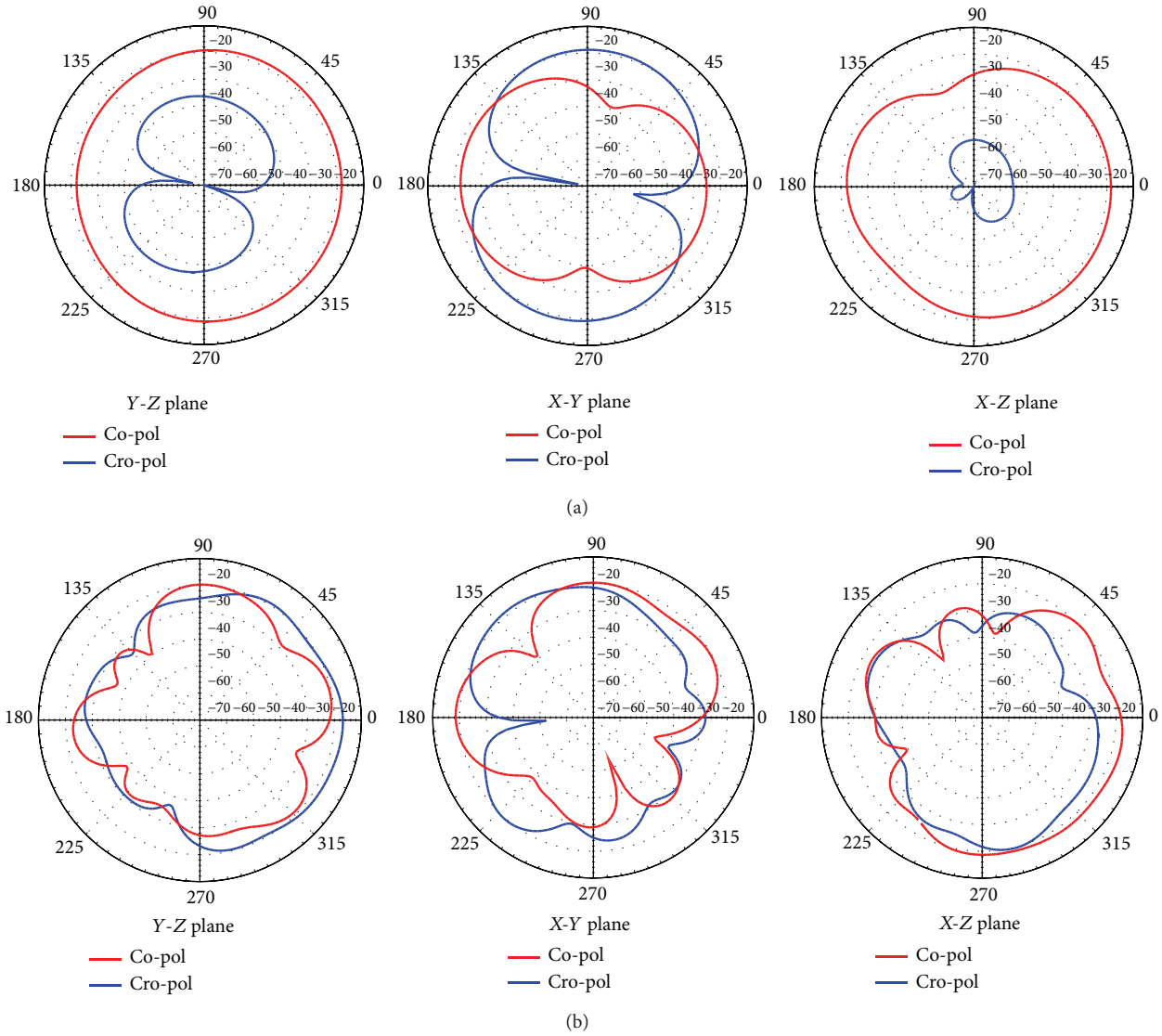


FIGURE 8: Measured 2D radiation pattern of the proposed antenna: (a) 2.4 GHz; (b) 5.8 GHz.

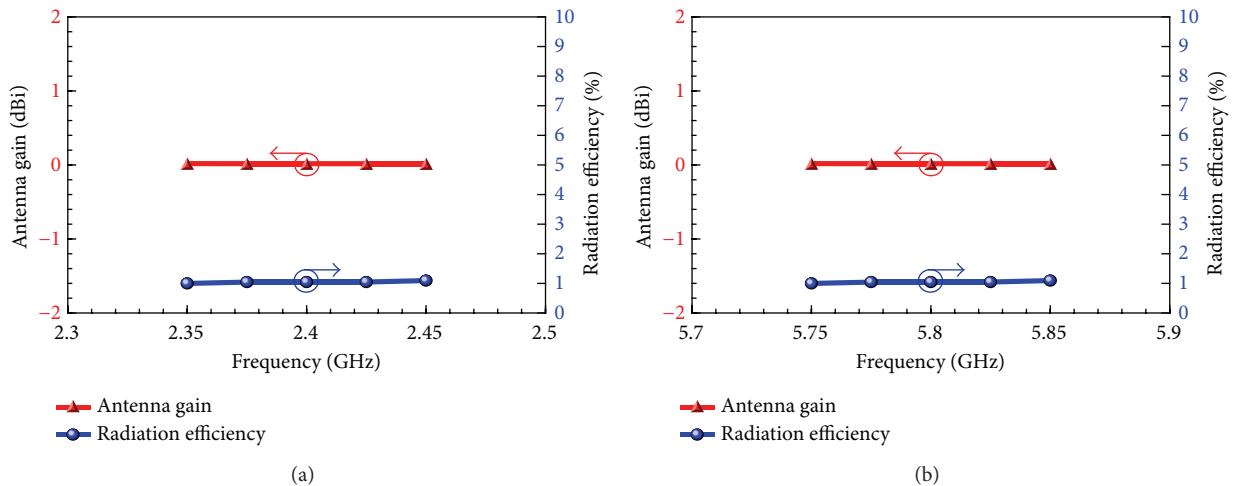


FIGURE 9: Measured radiation efficiency of the proposed antenna: (a) 2.3–2.5 GHz; (b) 5.7–5.9 GHz.

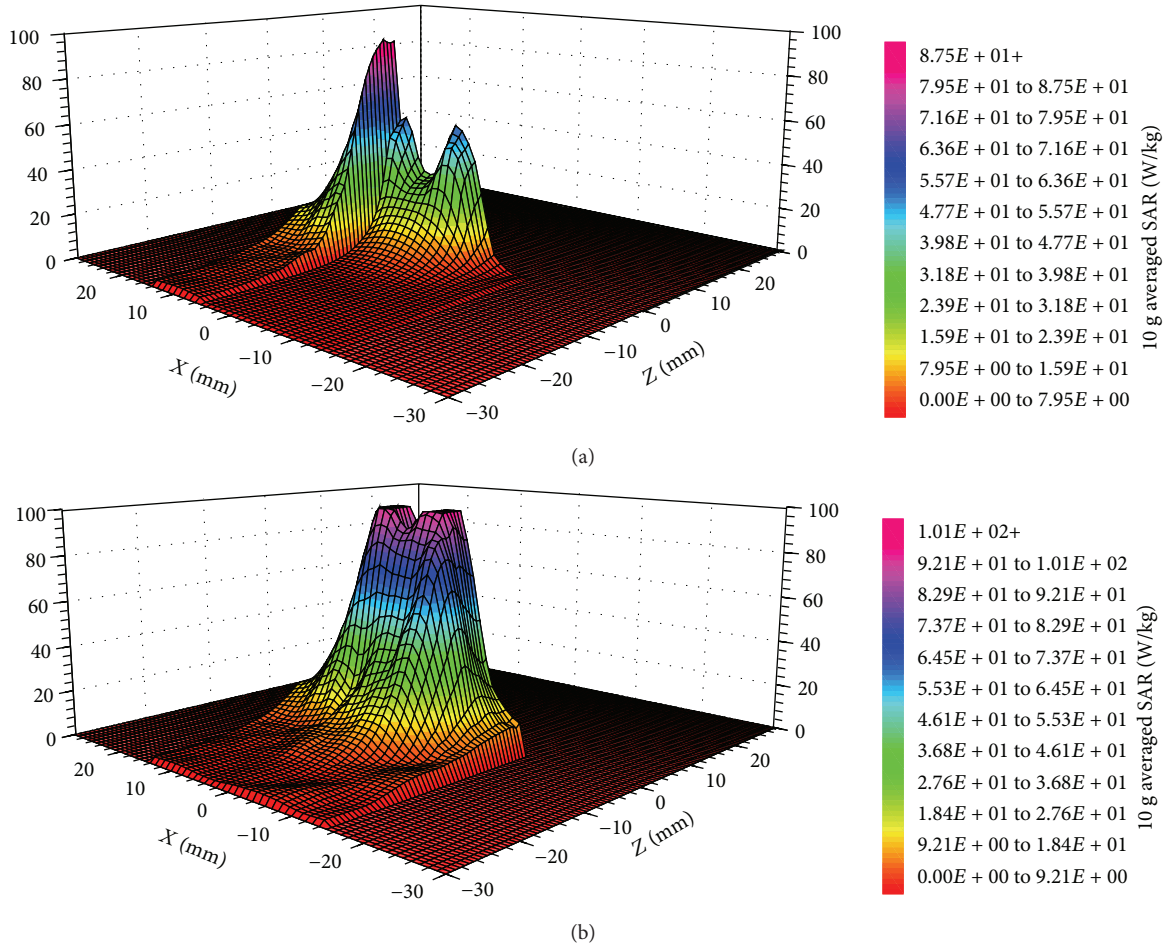


FIGURE 10: Simulated 10 g averaged SAR of the proposed antenna: (a) 2.4 GHz; (b) 5.8 GHz.

small variations and close to  $50\ \Omega$  impedance matching. The property of small impedance variations also creates broadband characteristic and covers 2.4 and 5.8 GHz for ISM band. Figure 6 shows the simulated  $S_{11}$  for different loop sizes of the proposed antenna. From the simulated results, smaller loop excites higher resonant modes, which meet the theory of resonance. Another feature of the proposed design is that the resonant modes are tunable. Figure 7 shows the surface current distributions of the proposed antenna at 2.4 and 5.8 GHz. In Figure 7(a), two zeroes and three poles on the loop form a  $1\ \lambda$  resonance. At the higher mode (Figure 7(b)), five zeroes and four poles create a  $1.5\ \lambda$  resonance. To sum up, the proposed design excites two resonant modes to obtain broad operation for ISM band that are verified. Figures 8(a) and 8(b) present the measured antenna 2D radiation pattern. In Y-Z plane, the pattern shows near omnidirectional pattern at 2.4 GHz. At higher band at 5.8 GHz, the patterns are twist and have more zeros. Figure 9 shows the measured antenna radiation gain and efficiency. At 2.4 and 5.8 GHz, the antenna gains are stable and close to 0 dBi. Besides, the radiation efficiency is also stable and close to 1% at that band. Because the human body is a lossy dielectric material, the efficiency of the antenna is always small [7]. In Figures 10(a) and 10(b),

the simulated 10 g averaged SAR distributions at ISM band (2.4 and 5.8 GHz) are obtained from the proposed antenna attached on eye tissue.

#### 4. Conclusions

This work presents a novel broadband loop antenna design (optimized bandwidth of 4.46 GHz) for wireless ocular physiological monitoring applications at ISM band (2.4 and 5.8 GHz). The proposed antenna has advantages of simple geometry and easy fabrication. Another feature of this design is that the resonant modes can be changed by varying the loop size. The simulated and measured results are also suitable for wireless ocular physiological monitoring applications.

#### Conflict of Interests

The authors declare that there is no conflict of interests regarding the publication of this paper.

## Acknowledgment

The authors would like to thank the National Science Council in Taiwan for financial supports (NSC-101-2220-E-006-003).

## References

- [1] M. Leonardi, E. M. Pitchon, A. Bertsch, P. Renaud, and A. Mermoud, "Wireless contact lens sensor for intraocular pressure monitoring: assessment on enucleated pig eyes," *Acta Ophthalmologica*, vol. 87, no. 4, pp. 433–437, 2009.
- [2] K. Stangel, S. Kolnsberg, D. Hammerschmidt, B. J. Hosticka, H. K. Trieu, and W. Mokwa, "A programmable intraocular CMOS pressure sensor system implant," *IEEE Journal of Solid-State Circuits*, vol. 36, no. 7, pp. 1094–1100, 2001.
- [3] J. Pandey, Y.-T. Liao, A. Lingley, R. Mirjalili, B. Parviz, and B. P. Otis, "A fully integrated RF-powered contact lens with a single element display," *IEEE Transactions on Biomedical Circuits and Systems*, vol. 4, no. 6, pp. 454–461, 2010.
- [4] Y.-T. Liao, H. Yao, B. Parviz, and B. Otis, "A  $3\mu\text{W}$  wirelessly powered CMOS glucose sensor for an active contact lens," in *Proceedings of the IEEE International Solid-State Circuits Conference (ISSCC '11)*, pp. 38–39, February 2011.
- [5] Institute of Applied Physics (IFAC), Nello Carrara, <http://niremf.ifac.cnr.it/tissprop/htmlclie/htmlclie.htm>.
- [6] Ansoft Corporation HFSS, <http://www.ansoft.com/products/hf/hfss/>.
- [7] J. Kim and Y. Rahmat-Samii, "Implanted antennas inside a human body: simulations, designs, and characterizations," *IEEE Transactions on Microwave Theory and Techniques*, vol. 52, no. 8, pp. 1934–1943, 2004.

## Research Article

# A Low-Profile WLAN Antenna with Inductor and Tuning Stub for Broadband Impedance Matching

Woo-Su Kim,<sup>1</sup> Sunho Choi,<sup>2</sup> and Gye-Taek Jeong<sup>3</sup>

<sup>1</sup> *Planning and Budget Team, KEIT, 10F KOTECHE Building, 305 Teheran-Ro, Gangnam-Gu, Seoul 135-080, Republic of Korea*

<sup>2</sup> *R&D Center, GoerTek Korea Co. Ltd, 607 A-dong Digital Empire B/D, 1556 Deogyong-daero, Yeongtong-gu, Suwon, Gyeonggi-do 443-812, Republic of Korea*

<sup>3</sup> *R&D Center, WAVE TECH B/D, 15 iljik-ro 94-gil, Seoksu-dong, Anyang, Gyeonggi-do 430-040, Republic of Korea*

Correspondence should be addressed to Gye-Taek Jeong; [gtjeong07@gmail.com](mailto:gtjeong07@gmail.com)

Received 9 January 2014; Accepted 11 March 2014; Published 8 April 2014

Academic Editor: Wenbin Dou

Copyright © 2014 Woo-Su Kim et al. This is an open access article distributed under the Creative Commons Attribution License, which permits unrestricted use, distribution, and reproduction in any medium, provided the original work is properly cited.

This paper presents a low-profile multiband antenna suitable for wireless local area networks (WLANs), using a chip inductor and tuning stub for broadband impedance matching. The proposed antenna is compact ( $12 \times 10 \times 1 \text{ mm}^3$ ) and covers three bands: 2.4-GHz (2.400–2.484 GHz), 5.2-GHz (5.150–5.350 GHz), and 5.8-GHz (5.725–5.825 GHz). The measured 10-dB bandwidths are 12.0% (2.28–2.57 GHz) in the lower band for 2.4-GHz WLANs and 39.1% (4.81–7.15 GHz) in the upper band for 5 GHz-WLANs. The measured peak gain of the antenna is between 2.7 and 4.39 dBi and the radiation patterns are omnidirectional.

## 1. Introduction

IEEE 802.11 a/b/g standards for wireless local area networks (WLANs) cover the following frequency bands: 2.4 GHz (2.400–2.484 GHz), 5.2 GHz (5.150–5.350 GHz), and 5.8 GHz (5.725–5.825 GHz). The use of mobile communication devices for WLAN applications is steadily increasing because multiband WLANs provide easy Internet access and compatibility with other devices and applications. Furthermore, because the rapid spread of smartphones has generated increasing demand for seamless Internet service, WLANs have become a common feature of mobile handsets [1]. While this has led to research into WLAN antennas [2–6], most of the resulting antennas are large or have complicated structural geometries that make them impractical for use in mobile phones.

Mobile phones are still evolving to become lighter and thinner with more diverse functions as technology advances. The space available for the antenna in a mobile phone decreases as the number of internal components increases. This poses a challenge for antenna designers because the antenna efficiency requirements remain unchanged. Early mobile phones had external antennas, which were often

helical [7]. However, external antennas have been replaced by internal designs for the sake of aesthetics and durability, based on studies that began in early 2000 [8–10]. Internal antennas for mobile phones are characterized by a low profile and a single substrate; they provide multiband coverage and omnidirectional radiation [4]. Impedance matching is essential in low-profile internal antennas to enhance antenna characteristics [1].

Antenna impedance-matching techniques can be classified into two categories: current impedance matching and lumped element matching. Current impedance matching sometimes results in complexity of design and manufacturing due to the modification of antenna geometry, and losses might be induced by the use of dielectric materials. In lumped element matching, the matching network of inductors and capacitors equalizes the impedance mismatch between the source and antenna load. This approach also results in some degree of loss and complexity [11–13].

This paper proposes a triple-band internal antenna for WLAN applications. The proposed antenna is a modified two-strip monopole antenna with a shunt inductor and tuning stub. To reduce the antenna volume and meet performance requirements, the height was fixed at 1 mm and the

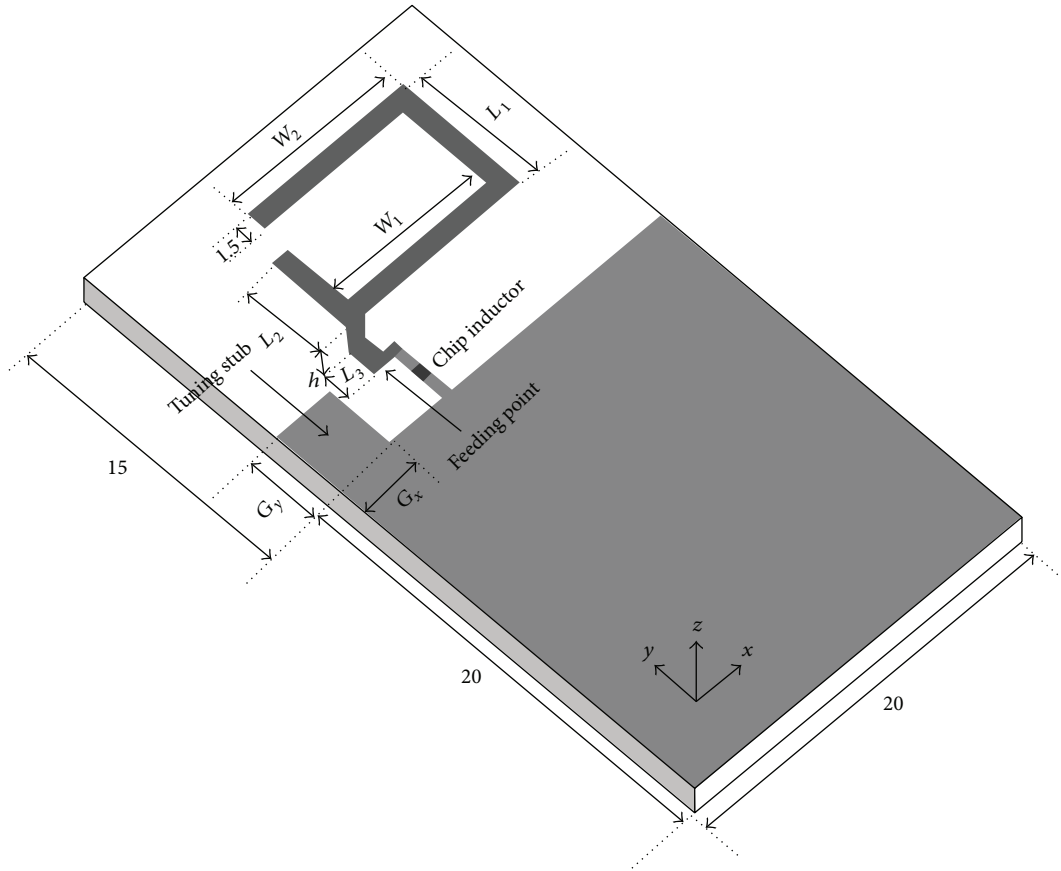


FIGURE 1: Geometry of the proposed WLAN antenna.

strip was folded. A shunt inductor ( $L = 6.8$  nH) was added for impedance matching at approximately 2.4 GHz and a tuning stub was included on the ground plane for broadband impedance matching. The capacitive coupling between the tuning stub and antenna tunes the resonance and broadens the impedance bandwidth in the 5-GHz bands. This antenna was designed and analyzed using the CST Microwave Studio software package [14]. Its performance was evaluated by measuring the actual characteristics of a physical prototype. This antenna could be used for triple-band WLAN operations and is much smaller than previous antennas [2–6]. The proposed impedance-matching technique is easily integrated into a PCB without increasing the antenna volume.

## 2. Antenna Design

The structure of the proposed antenna is shown in Figure 1. The antenna is built in an FR4 printed circuit board that is 0.8 mm thick and has a permittivity of 4.4; this material is frequently used in mobile phones due to its low cost. The substrate is  $20 \times 35$  mm and the system ground is  $20 \times 20$  mm. The antenna is a two-strip monopole with a shunt inductor and tuning stub. As shown in the figure, the folded monopole antenna geometry widely used in mobile handsets is used here to obtain dual resonance, omnidirectional radiation, and compact size.

Figure 2 shows the simulated reflection coefficient of a two-strip monopole antenna as a function of height  $h$ . In this simulation, the parameters were set as follows:  $L_1 = 8.0$  mm,  $L_2 = 4.7$  mm,  $L_3 = 2$  mm,  $W_1 = 9.0$  mm, and  $W_2 = 11.7$  mm. Figure 2 shows that the higher resonance frequency increased with the height, although the height had little effect on the lower resonance frequency. Conversely, an increase in height improved the impedance matching at the lower resonance but degraded that of the higher band. Therefore, we fixed the height at 1 mm to include resonances near 2.5 and 5 GHz while maintaining a low physical profile consistent with the latest trend in slim phones. With the height set at 1 mm, the current path length of strip 1 was 31.7 mm, which corresponded approximately to a quarter wavelength of 2.5 GHz. The overall length of strip 2 was 7.7 mm, corresponding approximately to a one-eighth wavelength of 5 GHz, but this is one-quarter wavelength in relation to  $\lambda = c/f\sqrt{\mu\epsilon}$ , where  $\mu = 1$  and  $\epsilon = 4.4$  for the high frequency. However, the antenna must enhance impedance matching and bandwidth for WLAN applications.

Figure 3 shows the simulated reflection coefficients of the antenna for different values of the chip inductor for the same parameters and a height of 1 mm. An inductor parallel to the antenna enhances the impedance matching in the 2.4-GHz band. When the inductance increased, the impedance matching improved, although there was little change in impedance

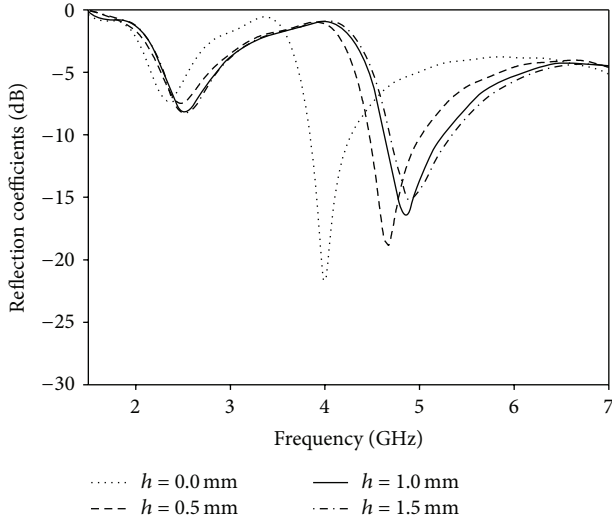


FIGURE 2: Simulated reflection coefficients of a two-strip monopole antenna as a function of height  $h$ .

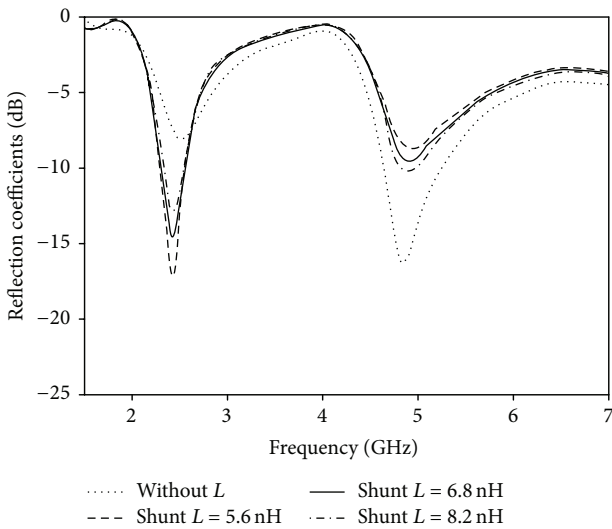


FIGURE 3: Simulated reflection coefficients of the proposed antenna as a function of the chip inductor ( $L$ ).

matching for the 2.4-GHz band when the value of the inductance was  $\leq 6.8$  nH. When the inductance increased, the impedance matching improved, but the measured antenna gain decreased. Hence, an inductance of 6.8 nH was found to be most appropriate. However, the bandwidth and impedance matching had to be enhanced for the 5.2- and 5.8-GHz bands while maintaining the characteristics of the 2.4-GHz band.

Figure 4 shows the enhancement of the bandwidth and impedance when a tuning stub ( $G_x = 3.2$  mm,  $G_y = 3.4$  mm) is inserted. Without the tuning stub, the input impedance of the 2.4-GHz band is inside the 2:1 voltage standing wave ratio (VSWR) circle, but the input impedance of the 5.2 and 5.8-GHz bands is outside. With the tuning stub, however, all frequency bands required for 5.2- and 5.8-GHz WLAN applications are satisfactory because the impedance locus on

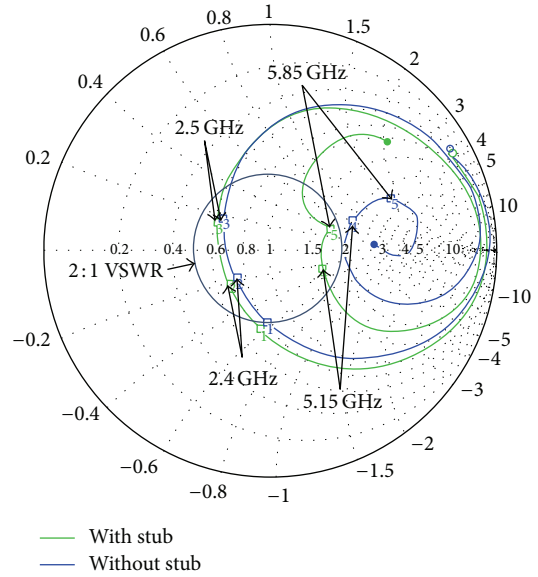


FIGURE 4: Simulated input impedance for the proposed antenna shown on Smith chart with (green) and without (blue) a tuning stub for frequencies 1.50–8.00 GHz.

the Smith chart moves inside the circle. Furthermore, the capacitive coupling between the tuning stub and antenna tunes the higher resonance and enhances bandwidth with little change to the lower band. This means that the proposed antenna covers all frequency bands required for 2.4/5.2/5.8-GHz WLAN applications when we choose a tuning stub with appropriate width  $G_x$  and length  $G_y$ .

Table 1 lists the results of a parameter analysis performed to optimize the tuning stub with the same antenna parameters shown in Figure 3 and an inductance value of 6.8 nH. Resonance and the 10-dB bandwidth of both bands were investigated when the width of tuning stub increased from 2.8 to 3.6 mm and the height increased from 3.0 to 3.8 mm in 0.4-mm increments. Table 1 shows that, without the tuning stub, the 2.4-GHz WLAN band was included, but the 5.2/5.8-GHz band was not. The lower resonance and 10-dB bandwidth were not affected by the size of the tuning stub, but the higher resonance increased with the tuning stub width and length. For a width of 3.0 mm, the 5.8-GHz band was not included. A width of 3.4 mm resulted in a broad 10-dB bandwidth that included the 5.2/5.8-GHz WLAN band for different tuning stub heights, unlike widths of 3.0 and 3.8 mm. Therefore, the width of the tuning stub was fixed at 3.4 mm. Since a width of 3.4 mm and length of 3.2 mm resulted in the maximum 10-dB bandwidth, 3.2 mm was selected as the most appropriate length.

According to the simulation results, the geometry proposed in this paper can be modeled by the equivalent circuit illustrated in Figure 5. The radiating strip 1, configured with  $L_3$ ,  $h$ ,  $W_1$ ,  $L_1$ , and  $W_2$ , as indicated in Figure 1, is represented by  $L_{\text{strip}1}$ ,  $C_{\text{strip}1}$ , and  $R_{\text{strip}1}$ . As Figure 3 shows, the shunt chip inductor  $L_{\text{chip}}$  is directly related to the resonant frequency of 2.4 GHz. Therefore, the radiating strip and the shunt chip inductor can be grouped together, resulting in the admittance

TABLE 1: Resonant frequency and 10-dB bandwidth for different tuning stubs.

Tuning stub		Lower band		Upper band	
$G_x$ (mm)	$G_y$ (mm)	$f_{low}$ (GHz)	$BW_{low}$ (%)	$f_{high}$ (GHz)	$BW_{high}$ (%)
0	0	2.42	8.2	4.90	0
	3.0	2.42	8.2	5.15	11.8
2.8	3.4	2.42	8.2	5.31	32.7
	3.8	2.42	8.2	5.41	29.5
3.2	3.0	2.42	8.2	5.20	7.7
	3.4	2.42	8.2	5.36	33.8
	3.8	2.42	8.2	5.46	29.0
3.6	3.0	2.42	8.2	5.23	7.6
	3.4	2.42	8.2	5.41	33.5
	3.8	2.42	8.2	5.52	29.1

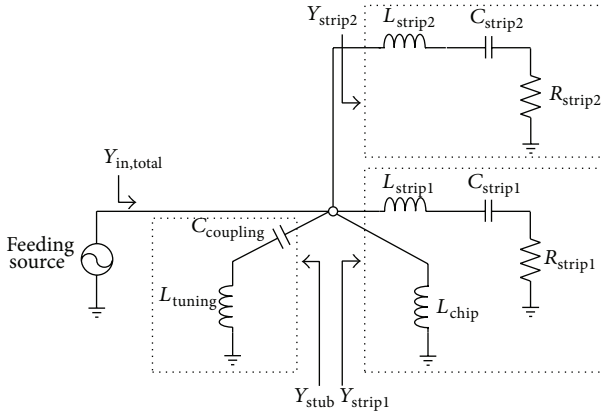
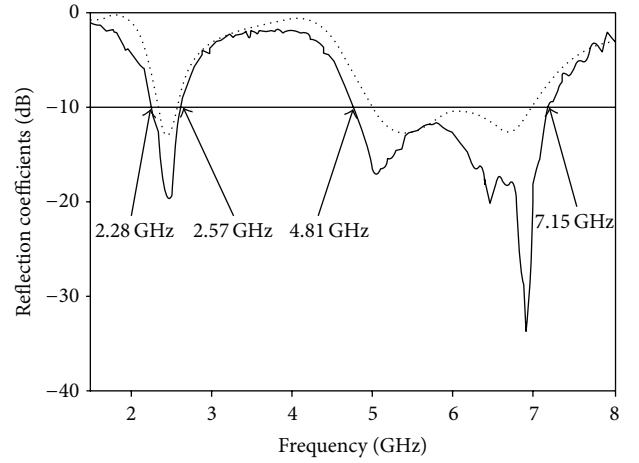


FIGURE 5: The equivalent circuit for the proposed WLAN antenna.

$Y_{strip1}$ , as shown in Figure 5. Similarly, the radiating strip 2, configured with  $L_3$ ,  $h$ , and  $L_2$ , is represented by  $L_{strip2}$ ,  $C_{strip2}$ , and  $R_{strip2}$ . The corresponding input admittance is  $Y_{strip2}$ . The tuning stub, represented by  $L_{tuning}$ , is connected to the feeding source via the coupling capacitor  $C_{coupling}$ . The corresponding input admittance is  $Y_{stub}$ . The approximate value of the admittance for each separate structure can be calculated using the full-wave simulation tool CST Microwave Studio. The resulting values of  $Y_{strip1}$ ,  $Y_{strip2}$ , and  $Y_{stub}$  are  $0.0292 + j0.0068$ ,  $0.0057 + j0.0034$ , and  $0.0078 - j0.0019$  mho, respectively, for 2.4 GHz;  $0.0004 + j0.0056$ ,  $0.0148 + j0.0064$ , and  $0.0176 + j0.0005$  mho, respectively, for 5.2 GHz; and  $0.0001 + j0.0038$ ,  $0.0022 + j0.0121$ , and  $0.0033 + j0.0164$  mho, respectively, for 5.8 GHz. The total input impedance  $Y_{in,total}$  can be approximately calculated as  $Y_{in,total} \approx Y_{strip1} + Y_{strip2} + Y_{stub}$  by ignoring the redundancy and coupling between equivalent blocks.

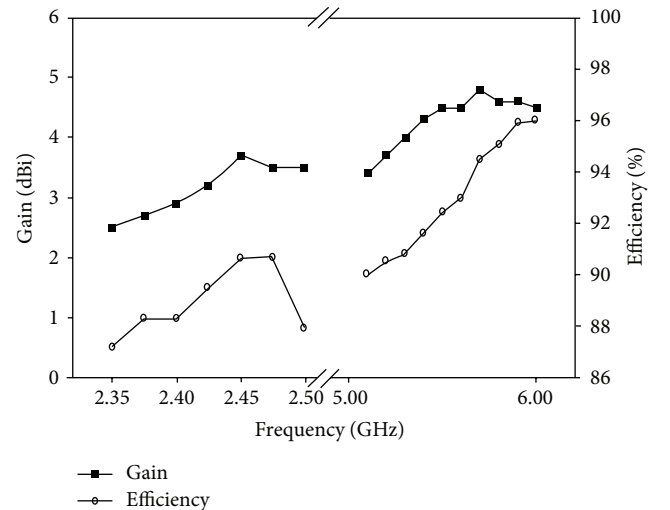
### 3. Measurement Results

A prototype antenna was fabricated using the optimized parameters obtained as described in the previous section. The performance of this prototype was characterized in terms of the reflection coefficient, gain, and radiation pattern, which were measured in an anechoic chamber.



..... Simulated  
 — Measured

FIGURE 6: Simulated and measured reflection coefficients of the proposed antenna.



■ Gain  
 ○ Efficiency

FIGURE 7: Measured radiation efficiency and peak gain of the proposed antenna.

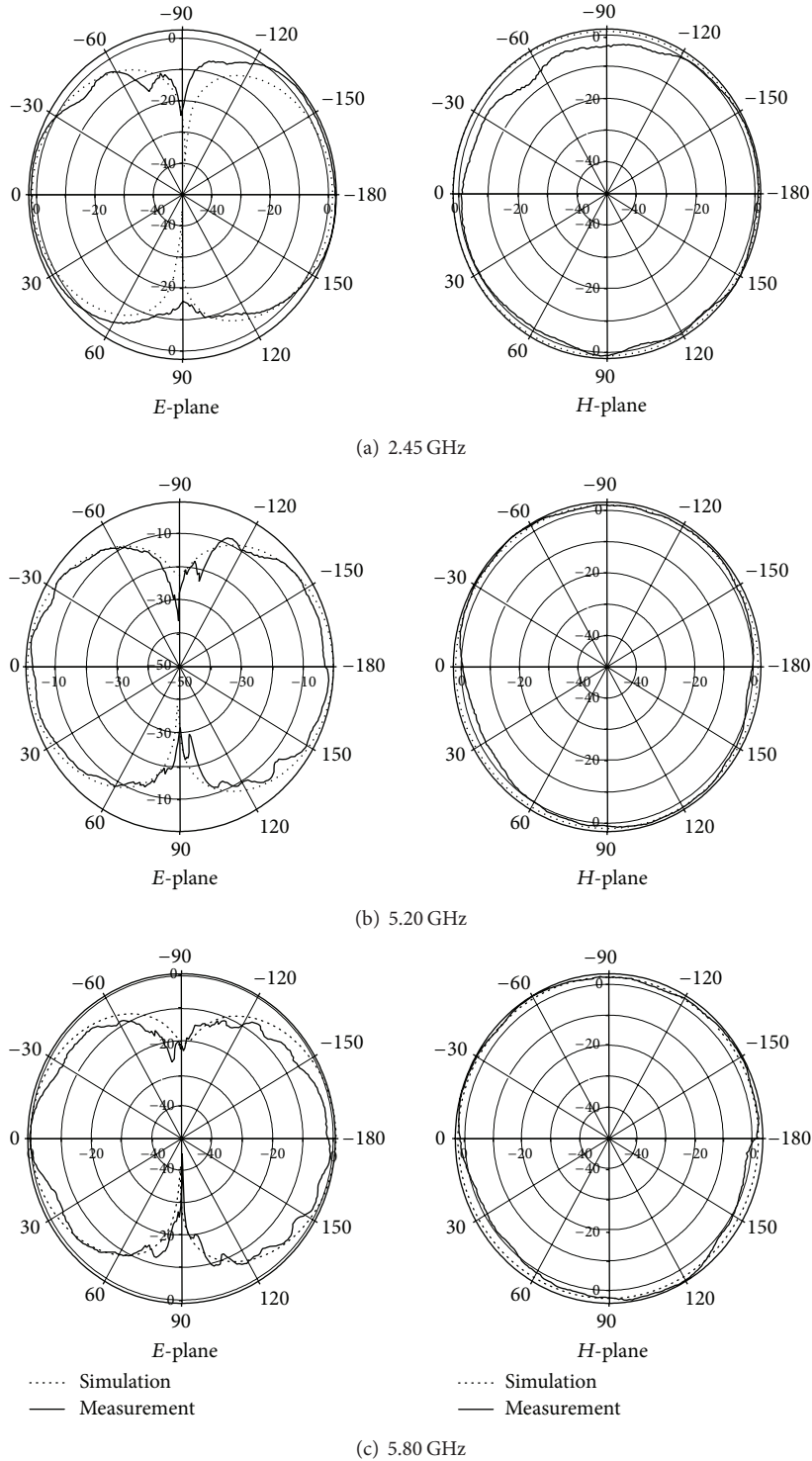


FIGURE 8: Simulated and measured radiation patterns of the proposed antenna.

The compact antennae [2–6] of multiband WLAN services occupy a lot of space and are not easy to integrate with other circuitry. The proposed antenna is smaller than Chiu’s antenna [2] and Kim’s antenna [3] by 56% and 12%, respectively. In addition, its bandwidths are wider than those

in [2, 3] by 6.7% and 7.0%, respectively, at 2.4 GHz and by 15.0% and 13.9%, respectively, at 5 GHz.

Figure 6 shows that the simulated and measured reflection coefficients of the antenna agreed closely. The 10-dB bandwidth of the prototype was 12.0% in the lower

band (2.28–2.57 GHz) and 39.1% in the higher band (4.81–7.15 GHz). These results show that broadband impedance matching was achieved and the proposed antenna satisfies the impedance conditions in all frequency bands required for 2.4/5.2/5.8-GHz WLAN applications.

Figure 7 shows the measured peak gain of the prototype antenna. The measured peak gain in the 2.4-GHz band ranges from 2.7 to 3.2 dBi. In the 5.2/5.8-GHz band, the measured peak gain varies between 2.95 and 4.39 dBi. These results are suitable for mobile terminals.

Figure 8 shows the simulated and measured radiation patterns of the prototype antenna at 2.45, 5.20, and 5.80 GHz measured from 0° to 360° at 5°-intervals. Good agreement was obtained between the simulated and measured results. These radiation patterns are omnidirectional over all the WLAN operating bands.

#### 4. Conclusion

This paper presents a low-profile two-strip monopole antenna with an inductor and tuning stub that can cover the 2.4/5.2/5.8-GHz WLAN frequencies. The narrow bandwidth and poor impedance matching due to the low-profile geometry were enhanced with a tuning stub and shunt inductor. A prototype constructed using optimized parameters had a fractional bandwidth of 12.0% in the lower band (2.28–2.57 GHz) and 39.1% in the higher band (4.81–7.15 GHz). The radiation pattern of the antenna was omnidirectional with a high peak gain of 2.7–4.39 dBi. Furthermore, at  $12 \times 10 \times 1$  mm, the overall size of the antenna makes it very promising for compact mobile terminals.

#### Conflict of Interests

The authors declare that there is no conflict of interests regarding the publication of this paper.

#### References

- [1] D. A. Sanchez-Hernandez, *Multiband Integrated Antennas for 4G Terminals*, Artech House, Boston, Mass, USA, 2008.
- [2] C. Y. Chiu, C. H. Chan, and K. M. Luk, "Small dual-band antenna with folded-patch technique," *IEEE Antennas and Wireless Propagation Letters*, vol. 3, no. 1, pp. 108–110, 2004.
- [3] T.-H. Kim and D.-C. Park, "Compact dual-band antenna with double L-slits for WLAN operations," *IEEE Antennas and Wireless Propagation Letters*, vol. 4, no. 1, pp. 249–252, 2005.
- [4] K.-L. Wong and C.-H. Chang, "WLAN chip antenna mountable above the system ground plane of a mobile device," *IEEE Transactions on Antennas and Propagation*, vol. 53, no. 11, pp. 3496–3499, 2005.
- [5] H. Wang and M. Zheng, "An internal triple-band WLAN antenna," *IEEE Antennas and Wireless Propagation Letters*, vol. 10, pp. 569–572, 2011.
- [6] A. G. Alhaddad, R. A. Abd-Alhameed, D. Zhou, C. H. See, P. S. Excell, and S. M. R. Jones, "Folded loop balanced coplanar antenna for WLAN applications," *IEEE Transactions on Antennas and Propagation*, vol. 60, no. 10, pp. 4916–4920, 2012.
- [7] Y. Letestu and A. Sharaiha, "Broadband folded printed quadrifilar helical antenna," *IEEE Transactions on Antennas and Propagation*, vol. 54, no. 5, pp. 1600–1604, 2006.
- [8] M. Ali, R. A. Sadler, and G. J. Hayes, "A uniquely packaged internal inverted-F antenna for bluetooth or wireless LAN application," *IEEE Antennas and Wireless Propagation Letters*, vol. 1, pp. 5–7, 2002.
- [9] K. L. Wong and C. I. Lin, "Internal GSM/DCS antenna backed by a step-shaped ground plane for a PDA phone," *IEEE Transactions on Antennas and Propagation*, vol. 54, no. 8, pp. 2408–2410, 2006.
- [10] V. A. Nguyen, M. T. Dao, Y. T. Lim, and S.-O. Park, "A compact tunable internal antenna for personal communication handsets," *IEEE Antennas and Wireless Propagation Letters*, vol. 7, pp. 569–572, 2008.
- [11] V. Iyer, S. N. Makarov, D. D. Harty, F. Nekoogar, and R. Ludwig, "A lumped circuit for wideband impedance matching of a non-resonant, short dipole or monopole antenna," *IEEE Transactions on Antennas and Propagation*, vol. 58, no. 1, pp. 18–26, 2010.
- [12] D. F. Bowman and E. F. Kuester, "Impedance matching, broadbanding, and baluns," in *Antenna Engineering Handbook*, J. L. Volakis, Ed., pp. 52–31, McGraw Hill, New York, NY, USA, 4th edition, 2007.
- [13] D. M. Pozar, *Microwave Engineering*, chapter 5, John Wiley & Sons, New York, NY, USA, 3rd edition, 2005.
- [14] CST Microwave Studio (MWS), *Version SP2*, CST Corporation, Framingham, Mass, USA, 2011.

## Research Article

# Radiation Efficiency Improvement Method for Multifeed Circular Polarization Antenna Array with Mutual Coupling Effect

Zijian Xing, Ling Wang, Jianying Li, and Kun Wei

*School of Electronics and Information, Northwestern Polytechnical University, Xi'an 710072, China*

Correspondence should be addressed to Ling Wang; [lingwang@nwpu.edu.cn](mailto:lingwang@nwpu.edu.cn)

Received 20 January 2014; Revised 6 March 2014; Accepted 10 March 2014; Published 3 April 2014

Academic Editor: Shaoqiu Xiao

Copyright © 2014 Zijian Xing et al. This is an open access article distributed under the Creative Commons Attribution License, which permits unrestricted use, distribution, and reproduction in any medium, provided the original work is properly cited.

In the circular polarization antenna array, the input impedance, axial ratio, and radiation pattern of antenna patch will be changed. Compared with the performances of single antenna, the mutual coupling also led to the low efficiency of all antennas. A novel radiation efficiency elevation method of multifeed circular polarization (CP) antenna array is demonstrated in this paper, in order to solve the problem. To prove the concept of novel method, dual-feed antenna with stubs is developed and fabricated. According to the measured results, each antenna would increase in efficiency by approximate 1dB by applying this novel design method. Therefore, this paper provides dramatically useful results of lessening the negative effect resulting in mutual coupling.

## 1. Introduction

Nowadays, circularly polarized microstrip patch antennas (MPAs) are one of the conventional antennas in the communication and radar systems [1–5]. The most important characteristics of these antennas are competing to Faraday rotation, reducing raindrops reflection effects, needing no estimation of the necessary orientation of the antenna according to the polarization of the received signals, duplicating the channel capacity, applying the positive and negative circular polarization, and reducing the fading effects.

According to feed methods, the MPAs can be divided into two kinds as the single feed and the multifeed [6, 7]. The structure of single feed circularity polarization antenna is greatly simple, because it does not need feed network. However, axial ratio (AR) and impedance bandwidth of single feed antenna are extremely narrow and sensitive. Although multifeed MAPs are complex in structure, they are widely applied in antenna array, because the axial ratio of which is more robust [8–10]. In small antenna array, the input impedance of each component is different because of mutual coupling. The efficiency of each component plays an important role in the amplitude consistence of the whole array. The radiation pattern of each component is also different

because it is the summation field of every component when one antenna is excited.

The impedance of radiation patch and feed network should be conjugate matched perfectly to obtain good efficiency of antenna. The I/O impedance of feed network shall be measured precisely and conjugate matched with the radiation patch. In this paper, double-feed CP antenna array is chosen to introduce the novel method of obtaining higher radiation efficiency.

This paper is organized as follows. In the second section, the radiation patch and feed network are introduced in detail. In the third section, theory analysis of axial ratio with mutual coupling effect is deduced. The novel method is applied in antenna array, thanks to which the performances of the antenna array will be improved. The last section will give the conclusion.

## 2. Structure of the Dual-Feed Patch

In accordance with the theory of the strip line, the character impedance of ideal strip line can be precisely calculated by the conformal mapping method. There is also some approximate arithmetic that can be adopted to shorten the calculation

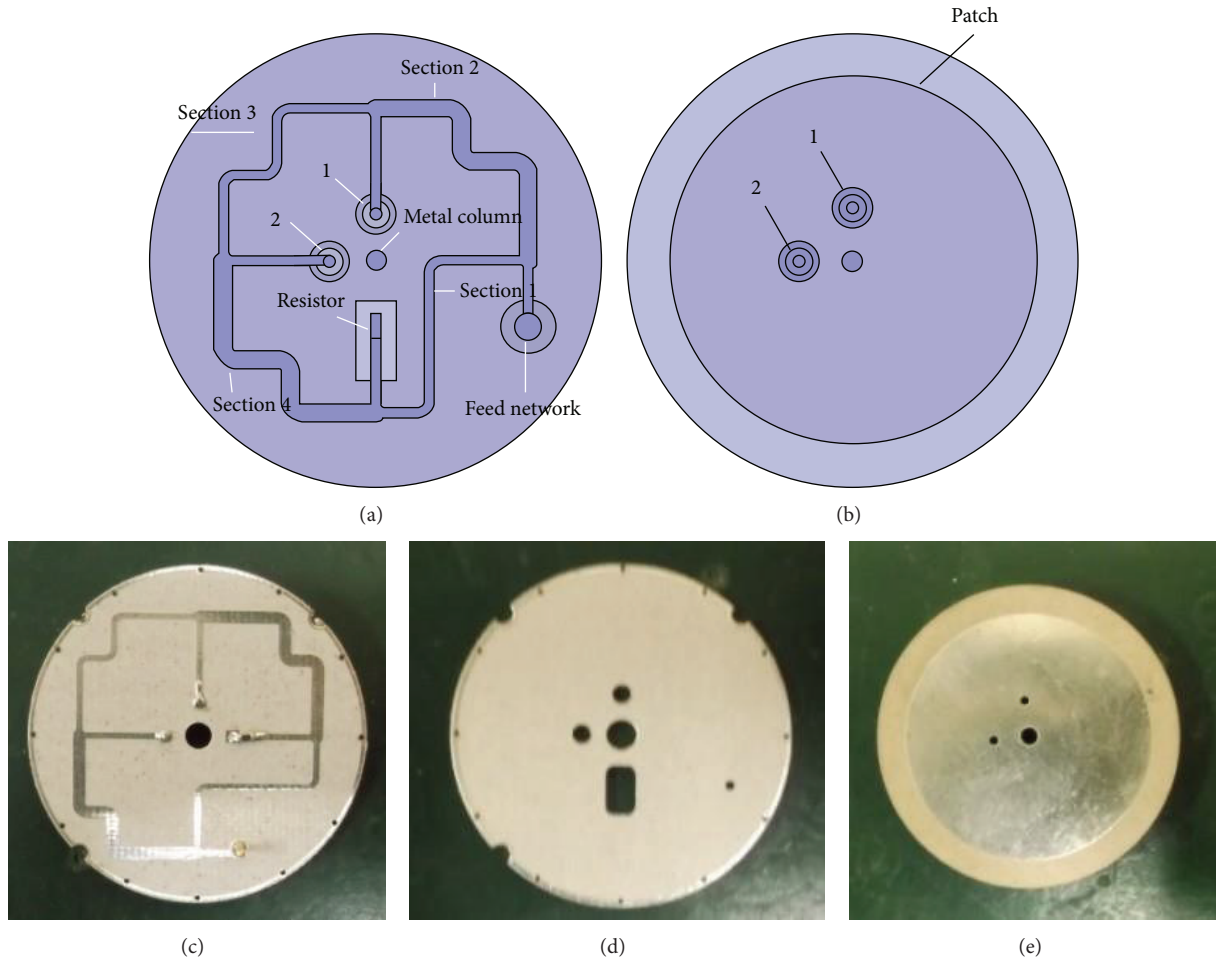


FIGURE 1: (a) shows the top view of the feed network which is a four-port strip line bridge, (b) is radiation patch on a thick PCB board of 4 mm, (c) is bottom view of the feed network photo, (d) is the other half of the feed network, and (e) is the photo of radiation patch.

process. Actual processed strip line is always composed of two PCB layers which are tightly combined. As shown in Figures 1(a) and 1(b), there are models of the RHCP GPS dual-feed network and a patch which is operated at 1.575 GHz. The radius of the antenna is 17 mm. The substrate permittivity of feed network is 4.6. The substrate permittivity of the radiation patch is 16. The radius of the metal patch is 13.5 mm. The feed network is a four-port electric bridge which contains one feed port, two output ports, and one isolation port. In Figure 1(a), 1 and 2 are the output ports which could supply equal amplitude and orthogonal signals for the patch in order to obtain the circular polarization. The isolation port is marked by *resistor* which can absorb leaking power and keep good performance of the power splitter. The feed network contains four sections of lines which have the same length equal to 23.4 mm or  $1/4$  wavelength. The width of Sections 1 and 3 is the same (1.304 mm), so is the width of Sections 1 and 2 (0.72 mm). The thickness of the feed network and radiation patch is 1.62 mm and 4 mm, respectively.

Figure 1(a) shows a model of four-port strip line bridge. Port 1 and 2 supply equal amplitude and orthogonal phase signals to the patch. In theory, the input and output impedance of a good bridge are 50 ohm, but the impedance of a patch is

greatly affected by the mutual coupling when the antenna is located in array. The problem will be studied and solved in the next section. Strip line feed networks are the combination of two pieces of PCB board which are shown in Figures 1(c) and 1(d). Figure 1(e) shows the top view of radiation patch.

The alone antenna could obtain good performances for GPS application. But in the antenna array, the efficiency of the antenna will decrease because of mutual coupling. The paper proposes an effective method for solving this problem in the next section.

### 3. Radiation Efficiency Improvement Method and Analysis

The performances of the antenna radiation pattern and axial ratio can be deteriorated due to mutual coupling. The pattern of antenna array is analyzed in many papers whereas the axial ratio of that is rarely analyzed. In Section 3.1, the axial ratio theory analysis of circular polarization antenna array is deduced. In order to solve the problem, the radiation efficiency improvement method is proposed and analyzed in

other sections. Seven-component antenna array is applied to show the effect of this novel method by experiments.

**3.1. The Axial Ratio Analysis of Circular Polarization Antenna Array.** The inner electronic field distribution of patch antenna is clearly known, so it is appropriate to be used to calculate the coupling efficiency which has been analyzed in many papers including radiation pattern and mutual impedance [10–13]. But the coupling effect study of axial ratio is rarely reported. In this section, the mutual coupling effects of axial ratio are deduced in theory. In circular polarization antenna, two resonant models have the same amplitude with 90-degree phase difference. The coupling effect of axial ratio is analyzed in theory by using two similar circular polarization microstrip antennas as shown in Figure 2. In Figure 2, axial ratio of antenna A is 1 when antenna B is not located beside it. Axial ratio is deduced when only antenna A is excited and antenna B is not excited. The analyzed conclusions of this model could be widely spread to various microstrip circular polarization antennas with different numbers and locations. The radius of these two antennas is marked by  $a$ .

Before obtaining the final axial ratio, the mutual reaction between antennas should be calculated. Similar to the mutual reaction in the calculation of dipole mutual impedance, the mutual reaction is defined as

$$\langle a, b \rangle = - \iint_{s_b} \vec{H}_{ab} \cdot \vec{M}_b ds, \quad (1)$$

where  $s_b$  is the area occupied by the source  $\vec{M}_b$  and  $\vec{H}_{ab}$  is the magnetic field produced by the current  $\vec{M}_a$  on the aperture of patch B. The  $\vec{H}_{ab}$  is obtained from the electric vector potential  $\vec{F}_a$  using

$$\vec{H}_{ab} = \frac{1}{j\omega\mu} \left[ k_0^2 \vec{F}_a + \nabla (\nabla \cdot \vec{F}_a) \right], \quad (2)$$

where  $\vec{F}_a$  is given by

$$\vec{F}_a = \iint_{s_a} \vec{G}(r, r') \cdot \vec{M}_a ds \quad (3)$$

$$\vec{G}(r, r') = \left[ \vec{I} + \frac{1}{k_0^2} \nabla \nabla \right] G_0(r, r'). \quad (4)$$

Here,  $S_a$  is the area of the magnetic current of antenna A.  $\vec{G}(r, r')$  is the free space dyadic Green function. However, for low values of permittivity and small substrate thickness, conditions which are usually true for microstrip antennas, one can use the free space Green function with negligible error. The electric field distribution for the  $TM_{mn}$  mode inside the patch metallization is given by

$$E(\rho, \phi) = A J_n(k_{mn}\rho) \cos n\phi \vec{z}. \quad (5)$$

The equivalent magnetic surface current at the border of antenna A is shown as in (6) and the magnetic current of other borders could be calculated by this equation:

$$\vec{M}_a = 2\vec{E} \times \vec{n} = 2E_z(a, \phi) \vec{\phi}. \quad (6)$$

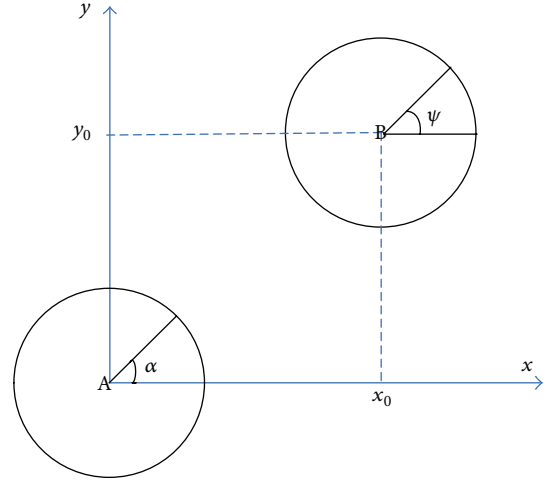


FIGURE 2: Diagram of the circular polarization antenna array which contains two microstrip antennas.

After obtaining the exact value of magnetic current around the periphery of antenna A, the magnetic field at  $xoy$  plane could be calculated by (2) and (3). The expressions for the components of  $H_{ab}$  are obtained as

$$\begin{aligned} H_{ab}^x &= \frac{1}{j\omega\mu} \int_0^{2\pi} \frac{aM_a \cos \alpha \cdot e^{-jkr}}{4\pi r^3} \\ &\cdot \left\{ 2 \sin \alpha (1 + jkr) + \frac{(y \sin \alpha + x \cos \alpha - a)}{r^2} \right. \\ &\quad \left. \times (k^2 r^2 - 3jkr - 3) \right\} d\alpha, \\ H_{ab}^y &= \frac{1}{j\omega\mu} \int_0^{2\pi} \frac{aM_a \cos \alpha \cdot e^{-jkr}}{4\pi r^3} \\ &\cdot \left\{ 2 \cos \alpha (1 + jkr) + \frac{(y \sin \alpha + x \cos \alpha)}{r^2} \right. \\ &\quad \left. \times (k^2 r^2 - 3jkr - 3) \right\} d\alpha, \end{aligned} \quad (7)$$

where  $r^2 = (x - a \cos \alpha)^2 + (y - a \sin \alpha)^2$ . The mutual react formulation could be derived below. Here, the value of  $\vec{M}_a$  equals  $\vec{M}_b$ , whereas the locations of the two are different:

$$\begin{aligned} \langle a, b \rangle_y &= \int_0^{2\pi} 2E_b(a, \psi) H_{ab}^y \cos \psi d\psi. \\ \langle a, b \rangle_x &= \int_0^{2\pi} 2E_b(a, \psi) H_{ab}^x \sin \psi d\psi. \\ \langle a, a \rangle_y &= \int_0^{2\pi} 2E_a(a, \alpha) H_{ab}^y \cos \alpha d\alpha. \\ \langle a, a \rangle_x &= \int_0^{2\pi} 2E_a(a, \alpha) H_{ab}^x \sin \alpha d\alpha. \end{aligned} \quad (8)$$

This completes the derivation of mutual reaction between two identical circular microstrip patch antennas. The general field is the summation of the two patch antennas radiation. Using this expression, the axial ratio at the normal orientation could be deduced in

$$\text{AR} = \frac{\max}{\min} \left[ \left( \int_0^{2\pi} e^{j(\pi/2)} E_a(a, \alpha) H_{ab}^y \cos \alpha d\alpha + \int_0^{2\pi} e^{j(\pi/2)} E_b(a, \psi) H_{ab}^y \cos \psi d\psi \right)^2 + \left( \int_0^{2\pi} E_a(a, \alpha) H_{ab}^x \sin \alpha d\alpha + \int_0^{2\pi} E_b(a, \psi) H_{ab}^x \sin \psi d\psi \right)^2 \right]^{(1/2)}. \quad (9)$$

The axial ratio is deduced when another antenna is located beside excited antenna A. It is clear that the axial ratio could also be obtained when any other antennas are located beside one excited circular polarization antenna. Therefore, the input impedance, radiation pattern, and axis ratio are simulated and measured in detail in this section and the next couple of sections.

**3.2. Impedance Analysis of Antenna Feed Point.** In order to lessen the negative effect of mutual coupling, the detailed impedance analysis of the patch is of great importance. The input impedance of the patch is closely related to the location of the feed point [10]. The input resistance of the circular microstrip patch could be calculated by the following equations when the antenna is operated at the main resonant mode:

$$R = \frac{V^2 J_1^2(k\rho_0)}{P_T}, \quad (10)$$

where  $V$  is the voltage which is the integral of electric field  $E$  through height  $h$ .  $J_1(k\rho_0)$  is the one-order Bessel function.  $\rho_0$  is the distance at radius,  $k$  is the propagation constant, and  $P_T$  is the consumption power which include the radiation power, consumption on the metal, and the substrate. If  $\rho_0$  becomes smaller,  $J_1(k\rho_0)$  and  $V$  will also be smaller, and visa verse. In (10),  $\rho_0$  is the variable. Simulation results of the antenna of Figure 1(b) are shown in Figure 3 which is the relationship between the input impedance and  $\rho_0$ .

In Figure 3, the resistance is so high when the antenna operates at the resonant frequency. But if the antenna does not operate at the resonant frequency, the reactance value shall not be 0. In this situation, the patch should be conjugate matched with the feed network in order to obtain enough efficiency. The reflection between the two is very large when their reactance properties are the same. In this paper, the theory is applied to obtain good effect on the improvement of the antenna gain. Just like Section 3.1, in circularity polarization antenna array, the resonant resistances of two polarizations in one antenna are affected by coupling differently, so the matching and axial ratio will be worse.

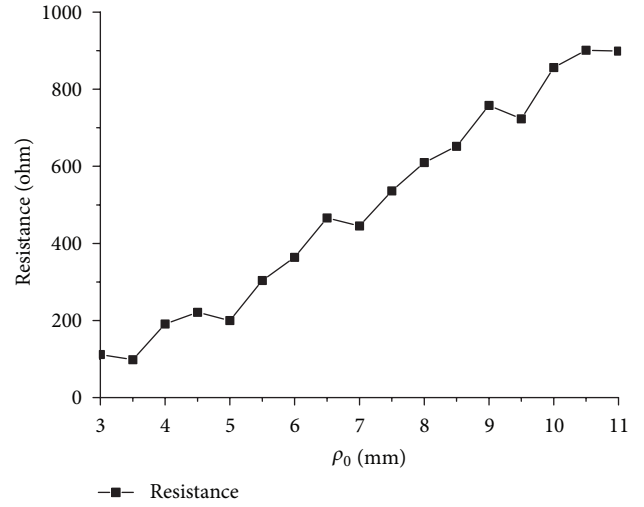


FIGURE 3: Resonant resistance versus different feed point.

**3.3. Radiation Efficiency Improvement Method.** After analyzing the relationship between feed point and impedance, seven-component circularity polarization antenna array is applied as the example in order to establish experiments of improvement method in this section. Figure 4 is the overview of seven-component antenna arrays which are of hexagonal shape and widely applied in the antijam navigation system. In order to investigate the performances of mutual coupling well, the antenna model in Figure 4(a) contains seven patches as in Figure 1(b). Figure 4(b) shows the seven integrated antennas which contain feed network and patch. Figure 4(a) has 14 ports, whereas Figure 4(b) has 7 ports. The impedance of each patch in Figure 4(a) also can be measured as follows: the target antenna is connected to vector network analyzer, while other antennas and ports are connected with matched load.

In Figure 4(a), feed points of each component are arranged in parallel. The distance among the adjacent component is 68 mm which is of 0.35 wave length. The array contains only seven components, so that each component in this array operates at different situations. It is easy to understand that each port is barely affected by other ports which operate at the orthogonal mode. Therefore, the working status of each port is mainly affected by the other six ports which radiate the same polarization wave. The ports impedance of antenna 1 could be calculated by the self-impedance and the mutual impedance:

$$\begin{aligned} Z_{a1} &= Z_{a11} + Z_{a21} + Z_{a31} + Z_{a41} + Z_{a51} + Z_{a61} + Z_{a71}, \\ Z_{b1} &= Z_{b11} + Z_{b21} + Z_{b31} + Z_{b41} + Z_{b51} + Z_{b61} + Z_{b71}, \end{aligned} \quad (11)$$

where subscripts  $a$  and  $b$  are ports 1 and 2 of each antenna, respectively.  $Z_{b1}$  is the input impedance of antenna 1's port 2,  $Z_{b11}$  is the self-impedance of antenna 1's port 2, and  $Z_{bi1}$  is the mutual impedance between port 2 of antenna  $i$  and that of antenna 1. From Figure 4(a), it could be easily deduced that  $Z_{a11} = Z_{b11}$  and  $Z_{a21} \neq Z_{b21}$ . Therefore, the two resonant modes are affected by coupling differently and  $Z_{a1} \neq Z_{b1}$ . The

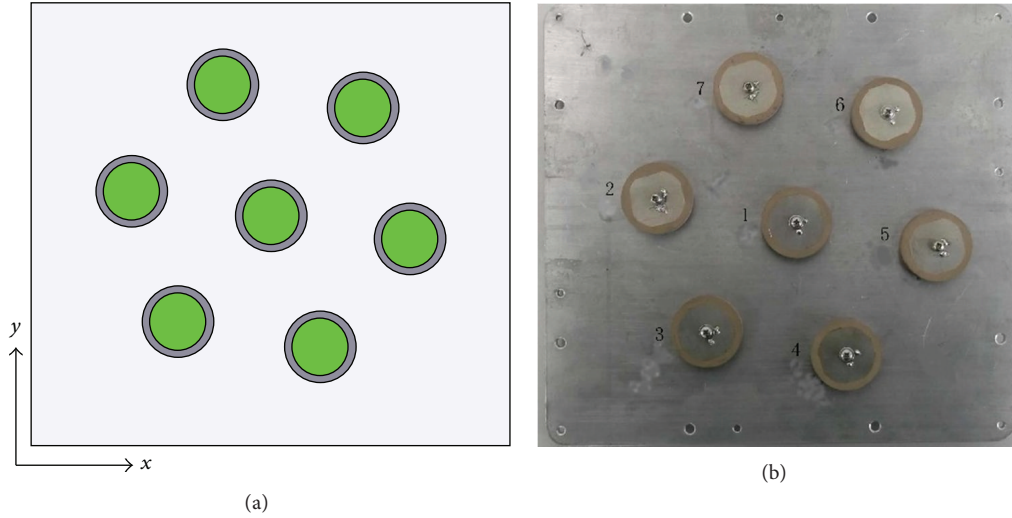


FIGURE 4: Seven-component antenna array: (a) a model without feed network and (b) final product of array.

TABLE 1: Measured input impedance of each port.

Port	$a1$	$a2$	$a3$	$a4$	$a5$	$a6$	$a7$
Impedance	$132 + 17 * j$	$75 - 33 * j$	$78 - 7 * j$	$77 - 29 * j$	$66 - 16 * j$	$75 - 11 * j$	$78 - 12 * j$
Port	$b1$	$b2$	$b3$	$b4$	$b5$	$b6$	$b7$
Impedance	$105 - 12 * j$	$67 + 6 * j$	$84 - 26 * j$	$74 - 29 * j$	$46 + 7 * j$	$68 - 37 * j$	$76 - 32 * j$

radiation perturbation is caused by the other antennas which can be excited by coupling. The measured impedance of each port in the antenna array of Figure 4 at 1.575 GHz is presented in Table 1.

In Table 1, the input impedance of each port in the antenna array is presented. Measured input impedance of each port is  $69 - 9 * j$  when the antenna stays alone. Mismatch leads to unequal power and distorted phase delay between the two ports of antenna. The paper proposes a novel experimental method to solve the problem of mismatch. Through applying this method, the efficiency of each component could be improved significantly.

The antenna could be designed as in Figure 5(a). The stubs of the antenna are applied for adjusting of the input impedance. By adjusting the length of two opposing stubs, the experiment could change the input impedance of each port, because the input impedance of microstrip antenna is mainly decided by the location of feed point. The measured port 1 and port 2 of the feed network are  $51 + 15 * j$  and  $48 + 23 * j$ , respectively. The best patch impedance of ports 1 and 2 should approach  $51 - 15 * j$  and  $48 - 23 * j$ , respectively. Figure 5(b) shows the Smith chart of number 2 antenna which is fed at port 1. If the stubs become shorter, the marker of any frequency will rotate around the curve along the anticlockwise orientation. But there is huge difference between stubs 1 and 2. The feed point effectively moves to edge if stub 1 becomes shorter; thus, the input impedance will become larger and the curve in Smith chart will move to the right, and vice versa. If stub 2 becomes shorter, the curve

will entirely move to the left. So, this is a very important rule for changing the impedance experimentally. By adjusting the stubs' length, the changed impedances of all ports are shown in Table 2. The dimensions of improved antenna stubs are shown in Table 3. For example, "11" means the length of stub 1 of number 1 antenna. The width of all stubs is 1 centimeter.

**3.4. Measurement Results Analysis of the Novel Method.** After improving the impedance of each antenna, the efficiency of each antenna is improved in various degrees. The pattern of original and improved antenna should be measured at the same place and same time, in order to obtain believable results. In Figure 6, the measurement scenario is shown; every component of the antenna array operates independently. Figure 6(a) shows the photo of transmitter antenna which is fixed on the vertical rotatable platform. Figure 6(b) shows that the receiver antenna array is fixed on the platform which can rotate at both vertical and horizontal orientation. The radiation pattern and axial ratio could be easily measured. Figure 7(a) shows the S11 performance of single antenna which is the combination of patch and feed network. The  $-10$  dB bandwidth is much larger than 100 MHz because one resistor locates at the isolation port in feed network to keep balance. In this paper, the S11 performance of the integrated antenna is not discussed in detail because it is always good during the experiment. Figure 7(b) shows the gain performance when the antenna stays alone. The gain is the largest when the antenna operates at 1.575 GHz. The

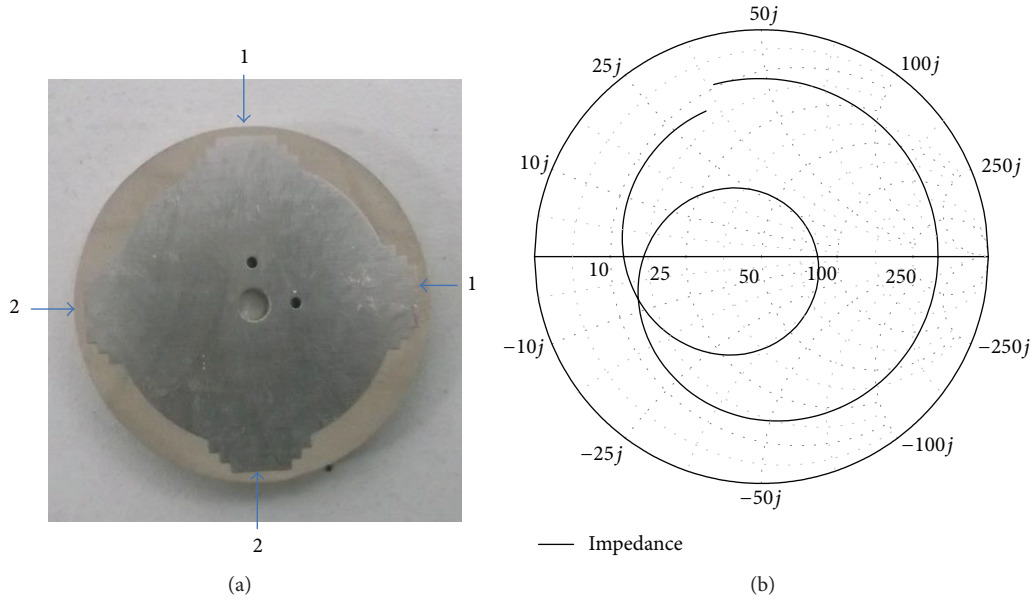


FIGURE 5: (a) The photo of improved antenna which contains two couples of stubs. (b) Measured number 2 component Smith chart versus frequency.

TABLE 2: Measured improved input impedance of each port.

Port	$a1$	$a2$	$a3$	$a4$	$a5$	$a6$	$a7$
Impedance	$52 - 17 * j$	$48 - 23 * j$	$53 - 21 * j$	$61 - 19 * j$	$56 - 16 * j$	$51 - 21 * j$	$56 - 28 * j$
Port	$b1$	$b2$	$b3$	$b4$	$b5$	$b6$	$b7$
Impedance	$55 - 6 * j$	$53 - 16 * j$	$54 - 27 * j$	$51 - 22 * j$	$55 - 17 * j$	$56 - 29 * j$	$59 - 22 * j$

TABLE 3: Dimensions of the improved antennas.

Stub	11	21	31	41	51	61	71
Length (mm)	0.3	0.3	0.1	0.1	0.1	0	0.1
Stub	12	22	32	42	52	62	72
Length (mm)	0.2	0	-0.1	-0.2	0	0.2	0.3

gain will decrease when the operating frequency of antenna is deviated. The novel method is mainly applied in the single frequency point, so that the gain performances of the resonant frequency are discussed in detail. Figure 7(c) shows the efficiency performance with different frequency.

In Figures 8(a), 8(b), and 8(c), the comparison between the original and the improved pattern of three antennas is demonstrated. Number 2, number 4, and number 6 in antenna array of Figure 4(b) are selected as an example. The picture shows the normalized power radiation pattern which is the power composition of the vertical and horizontal electrical field part. All the patterns are measured at  $xoz$  plane and normalized by the original gain. In Figure 8(d), the gain difference between original antenna array and improved antenna array is shown. It is clear that the gain of the improved antenna array is increased. Because the shapes of patterns are similar between original antenna and improved

antenna, the gain difference approximately equals efficiency difference.

In Figure 8, it could be easily observed that, after adopting novel technology, the efficiency of all antennas is improved. It is proved that the novel technology is of enormous use in lessening the negative effect which results in mutual coupling. Mutual coupling leads to the differences among the pattern shapes of antennas. The pattern shape of each antenna is not changed significantly after improvement because the pattern is relatively robust. The radiation pattern is determined by not only the location of the component but also the mutual coupling between components. In induction theorem, electromagnetic wave will be received by other components and radiated again when only one component is excited. The final radiation pattern is the superposition of the radiation of every component. The axial ratio is not robust and improved subtly when the novel technology is applied. In order to study the axial ratio performance further, the axial ratio performances of the same antennas are also shown in Figure 9.

Figure 9 selects three antennas and shows comparison of axial ratio between the original antennas and the improved ones. It is observed that the axial ratio is improved when the novel method is applied; axial ratios of these antennas are all lower than 3 dB at the axial orientation. The axial ratio is easily changed by coupling of other components, especially

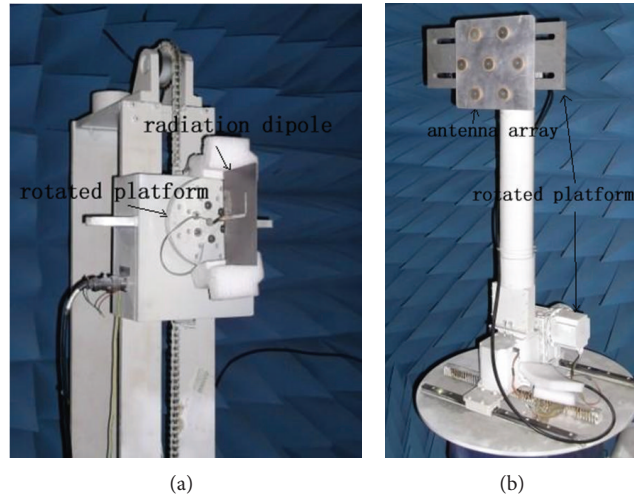


FIGURE 6: Measurement scenarios: (a) radiation antenna is fixed on the rotatable platform. (b) Received antenna is fixed on rotatable platform.

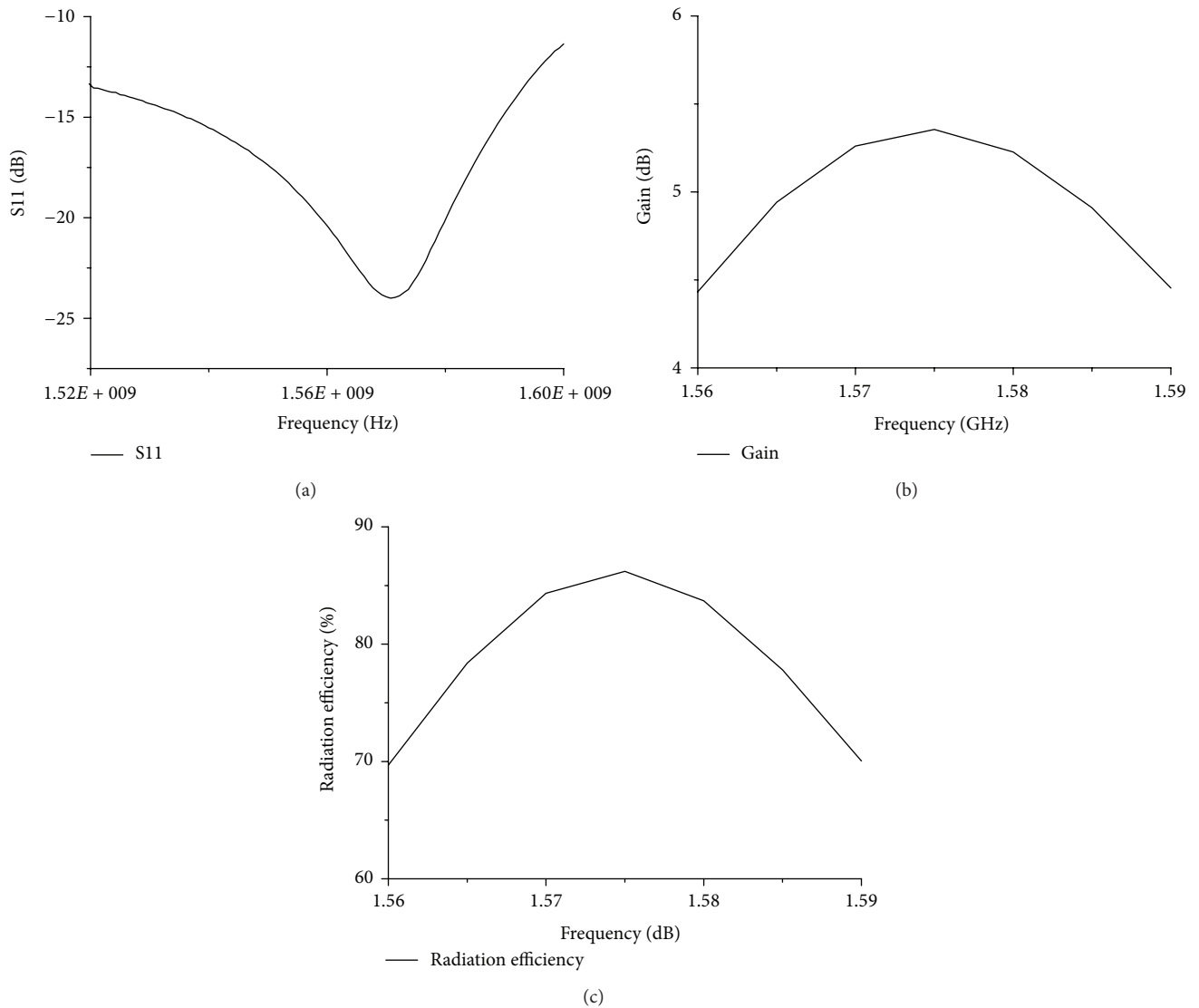


FIGURE 7: Performances of integrated single antenna. (a) S11, (b) gain, and (c) efficiency.

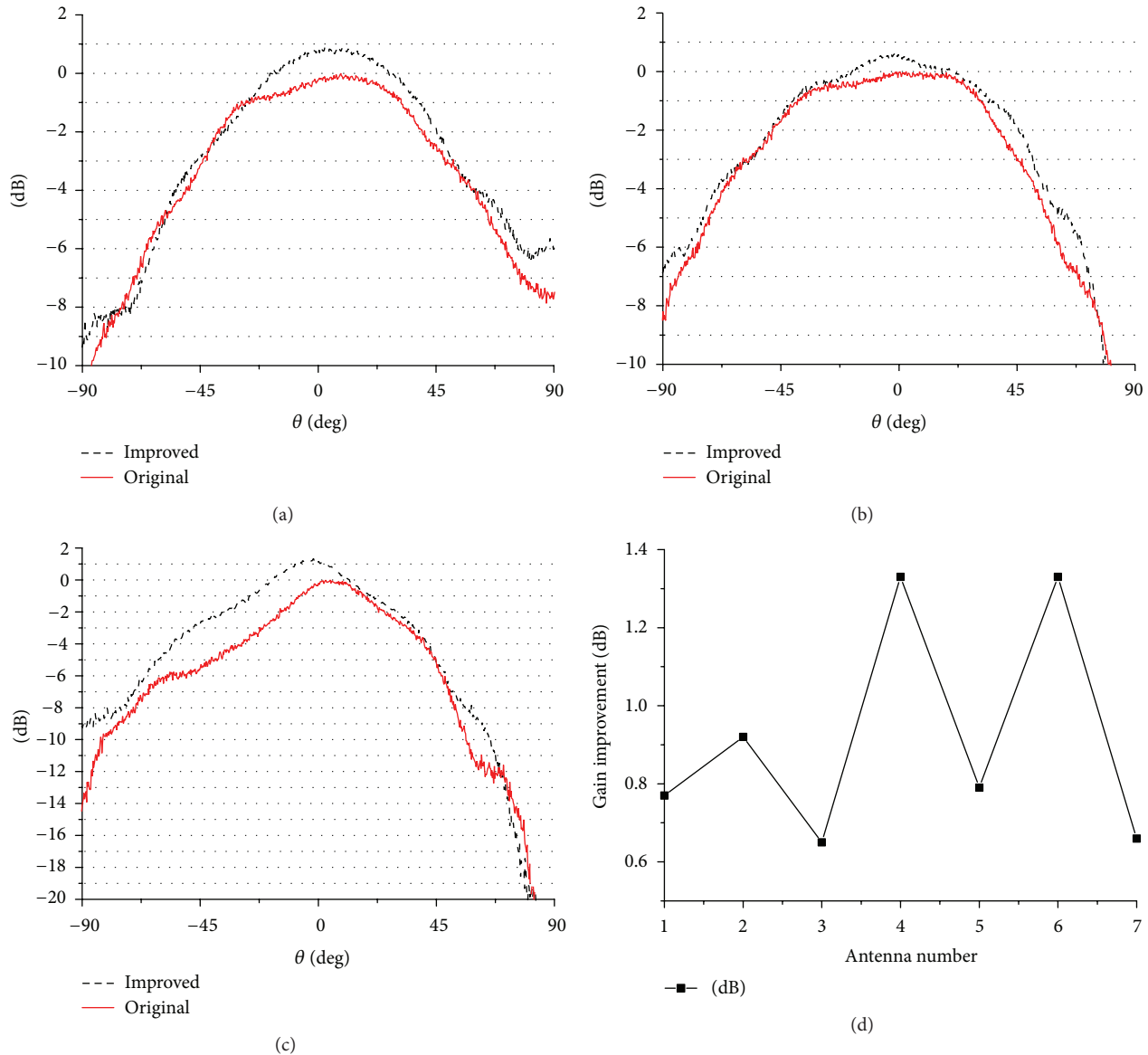


FIGURE 8: Comparing between improved pattern and original pattern: (a) number 2 component, (b) number 4 component, (c) number 6 component, and (d) efficiency/gain improvement curve.

in the low elevation. The distortion of radiation pattern also influences the axial ratio because the beam fails to point to the normal orientation. Therefore, the axial ratio is worse than before at some directions, which is very hard to be avoided. The novel method is applied to improve the match and raise the radiation efficiency of circular polarization antenna. Actually, the AR of axial orientation is improved under most of the conditions. Especially, the axial ratio performance at normal direction is the most important one for the circular polarization antenna.

#### 4. Conclusion

In this paper, one novel debugging method aiming at improving the efficiency of circular polarization antenna in array was proposed. By introducing the stubs and using the Smith chart,

the impedance of each patch could be well conjugate matched with the feed network. Owing to the well matched antenna patch constructed, the radiation efficiency could be increased by about 1 dB. Due to their good characteristic of increasing efficiency, the circularity polarization multifeed antennas in small antenna array could obtain weaker signal from planet and earn better navigation effect.

Moreover, the axial ratio in antenna array is also numerically analyzed and easily distorted by various electromagnetic circumstances. In antenna array, the main causation is that other antennas will be excited by mutual coupling.

#### Conflict of Interests

The authors declare that there is no conflict of interests regarding the publication of this paper.

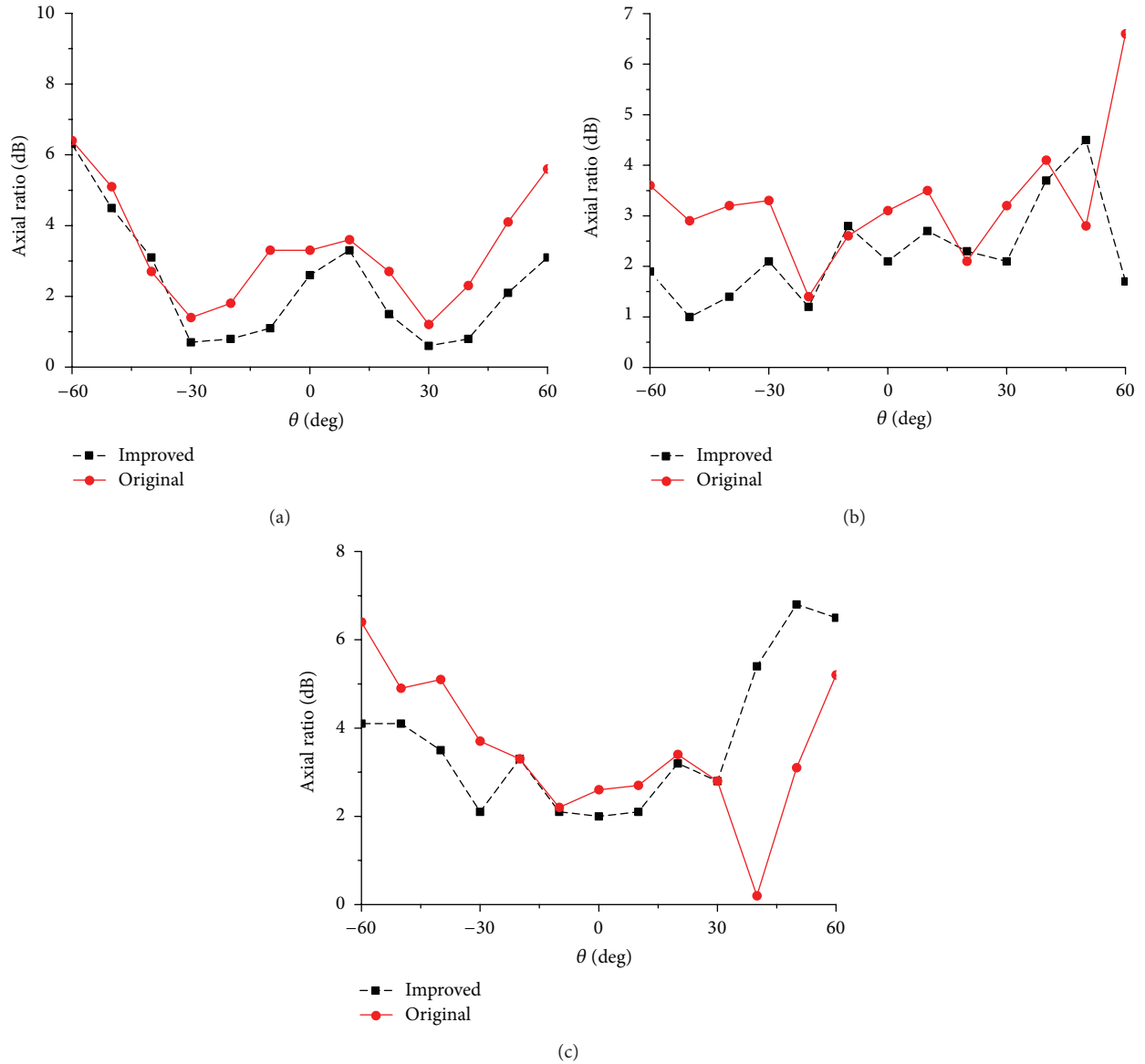


FIGURE 9: Axial ratio performances of the three components: (a) number 2 component, (b) number 4 component, and (c) number 6 component.

## Acknowledgments

This work was supported in part by the National Natural Science Foundation of China (nos. 61301093 and 61271416) and the National Defense Pre-Research Foundation of China (no. 11055132535).

## References

- [1] A. H. Sharif and M. Soleimani, "Accurate analysis and design of dual-feed circularly polarized microstrip patch antenna based on multiport network model," in *Proceedings of the Asia-Pacific Microwave Conference (APMC '05)*, vol. 4, December 2005.
- [2] R. D. Murch and K. Ben Letaief, "Antenna systems for broadband wireless access," *IEEE Communications Magazine*, vol. 40, no. 4, pp. 76–83, 2002.
- [3] Y. Ushijima, E. Nishiyama, and M. Aikawa, "Single-layer integrated microstrip array antenna for dual circular polarisation microwaves," *IET Microwaves, Antennas & Propagation*, vol. 6, no. 8, pp. 962–968, 2012.
- [4] J. Ouyang, "A circularly polarized switched-beam antenna array," *IEEE Antennas and Wireless Propagation Letters*, vol. 10, pp. 1325–1328, 2011.
- [5] W.-T. Hsieh, T.-H. Chang, and J.-F. Kiang, "Dual-band circularly polarized cavity-backed annular slot antenna for GPS receiver," *IEEE Transactions on Antennas and Propagation*, vol. 60, no. 4, pp. 2076–2080, 2012.
- [6] Y.-J. Hu, W.-P. Ding, and W.-Q. Cao, "Broadband circularly polarized microstrip antenna array using sequentially rotated technique," *IEEE Antennas and Wireless Propagation Letters*, vol. 10, pp. 1358–1361, 2011.

- [7] A. D. Nestic and D. A. Nestic, "Printed planar  $8 \times 8$  array antenna with circular polarization for millimeter-wave application," *IEEE Antennas and Wireless Propagation Letters*, vol. 11, pp. 744–747, 2012.
- [8] C. Vázquez, G. R. Hotopan, S. ver Hoeye, M. Fernández, L. F. Herrán, and F. las Heras, "Microstrip antenna design based on stacked patches for reconfigurable two dimensional planar array topologies," *Progress in Electromagnetics Research*, vol. 97, pp. 95–104, 2009.
- [9] P. Rocca, L. Manica, and A. Massa, "An effective excitation matching method for the synthesis of optimal compromises between sum and difference patterns in planar arrays," *Progress in Electromagnetic Research B*, vol. 3, pp. 115–130, 2008.
- [10] I. J. Bahl and P. Bhatia, *Microstrip Antenna*, Publishing House of Electronics Industry, 1984.
- [11] D. M. Pozar, "Input impedance and mutual coupling of rectangular microstrip antennas," *IEEE Transactions on Antennas and Propagation*, vol. 30, no. 6, pp. 1191–1200, 1982.
- [12] C. H. Niow, Y. T. Yu, and H. T. Hui, "Compensate for the coupled radiation patterns of compact transmitting antenna arrays," *IET Microwaves, Antennas and Propagation*, vol. 5, no. 6, pp. 699–704, 2011.
- [13] S. R. Best, "Mutual coupling between orthogonal electrically small dipole antennas," in *Proceedings of the 6th European Conference on Antennas and Propagation (EUCAP '12)*, pp. 1663–1666, 2012.

## Research Article

# Suppression of Cross-Polarization of the Microstrip Integrated Balun-Fed Printed Dipole Antenna

Huang Jingjian, Zhang Xiaofa, Xie Shaoyi, Wu Weiwei, and Yuan Naichang

*College of Electronic Science and Engineering, National University of Defense Technology, Changsha 410073, China*

Correspondence should be addressed to Huang Jingjian; [hjjfh2003@aliyun.com](mailto:hjjfh2003@aliyun.com)

Received 25 December 2013; Accepted 24 February 2014; Published 1 April 2014

Academic Editor: Xiuping Li

Copyright © 2014 Huang Jingjian et al. This is an open access article distributed under the Creative Commons Attribution License, which permits unrestricted use, distribution, and reproduction in any medium, provided the original work is properly cited.

The high cross-polarization of the microstrip integrated balun-fed printed dipole antenna cannot meet the demands of many engineering applications. This kind of antennas has high cross-polarization levels (about  $-20$  dB). And we find that the high cross-polarization radiation is mainly produced by the microstrip integrated balun rather than the dipole itself. The very limited method to lower the cross-polarization level of this kind of antennas is to reduce the substrate thickness. In this paper, to improve the low cross-polarized performance, firstly, an equivalent model is presented to analyze the cross-polarization radiation. Secondly, a novel structure with low cross-polarization is proposed. The microstrip integrated balun is enclosed by a center slotted cavity. The E-field of the microstrip integrated balun is transformed parallel to the dipole arms by the slot, so the radiation of the cross-polarized component is suppressed. Measured results show that this structure can achieve a bandwidth wider than 40% while reducing the cross-polarization level to less than  $-35$  dB within the frequency band.

## 1. Introduction

Microstrip integrated balun-fed printed dipole antenna (PDA) is proposed by Edward and Rees [1] in 1987, and it is widely used in the communication and radar systems [1–12], owing to their salient features such as light weight, wideband, low cost and ease of fabrication, and suitability for integration with circuit modules. In 1989, Proudfoot [2] designed a folded printed dipole. The radiation impedance can be adjusted from 70 ohms to 200 ohms. And Proudfoot also supposed that the high cross-polarization is caused by the microstrip integrated balun rather than the dipole itself. Now, many applications require low cross-polarization. Zhou et al. [12] proposed a double-layered structure to improve the cross-polarization. But its stripline feeding structure made it hard to feed by a coaxial connector.

In this paper, an equivalent model to analyze the cross-polarization of the microstrip integrated balun-fed PDA is presented. Based on the equivalent circuit [13] of the microstrip integrated balun, an impedance element is placed

in the center of the slotted balun to replace the dipole radiation impedance and fill the slot of the shorting slotline between the two dipole arms with metal to restrain the radiation of the dipole. The E-plane and H-plane cross-polarized patterns are compared. The accordant results validate that the cross-polarization is mainly radiated by the microstrip integrated balun rather than the dipole itself. Then the cross-polarization varying with the main parameters of the substrate is studied. The simulated results show that it has very limited improvement on the cross-polarization by varying the substrate parameters. To improve the cross-polarization performance, a printed dipole antenna whose microstrip integrated balun is enclosed by a center slotted cavity is proposed. The microstrip integrated balun is moved down [3], so the input impedance can be directly matched to 50 ohm. Furthermore, the cavity can be placed under the dipole arms. This structure can create the wide bandwidth characteristic while considerably suppressing the cross-polarized component. The antenna is simulated by Ansoft Corporation's high frequency structure simulator (HFSS).

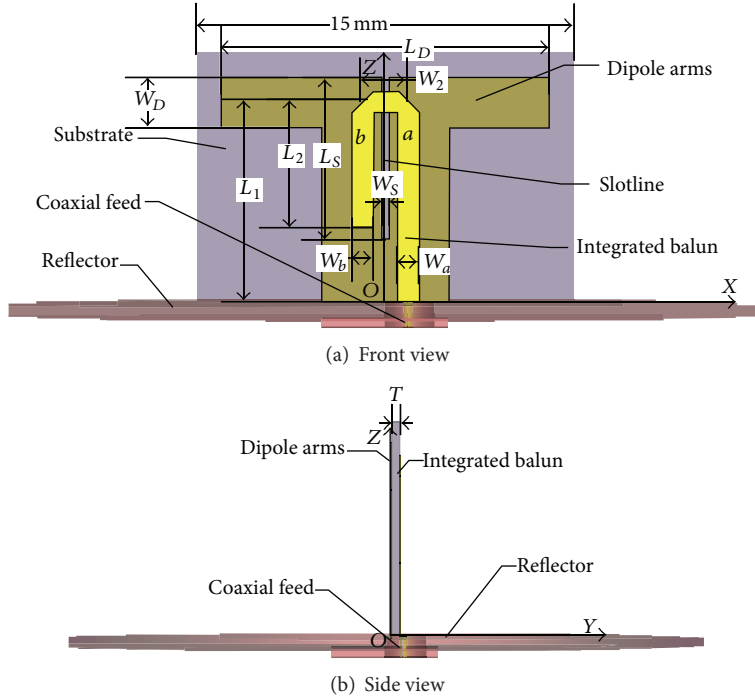


FIGURE 1: Geometry of the microstrip integrated balun-fed PDA.

## 2. Cross-Polarization Analysis

Due to the asymmetrical feeding structure, the  $Y$  directional E-field component could be activated between the microstrip integrated balun and the dipole arms. This part of electronic field can make a high level cross-polarization.

The geometry of the microstrip integrated balun-fed PDA is shown in Figure 1. The front view and side view of this antenna model are shown in Figure 1(a) and Figure 1(b), respectively. Microstrip integrated balun and dipole arms are printed on each side of the substrate. The antenna is placed on a circular reflector with a diameter of 30 mm and fed by a coaxial connector. The microstrip integrated balun has a microstrip line "a" with width  $W_a = 0.87$  mm, a microstrip line "b" with width  $W_b = 0.87$  mm, the balun with width  $W_2 = 1.8$  mm and length  $L_1 = 7.5$  mm, and match branch with length  $L_2 = 5$  mm. The substrate has the relative permittivity  $\epsilon_r = 2.2$  and thickness  $T = 0.5$  mm. The dipole has slotline width  $W_S = 0.3$  mm and slotline length  $L_S = 6.83$  mm and dipole arm width  $W_D = 2$  mm and length  $L_D = 13$  mm.

The equivalent circuit is shown in Figure 2. According to the transmission line theory, the input impedance can be written as

$$Z_{in} = -jZ_b \cot \theta_b + \frac{jZ_L Z_s \tan \theta_s}{Z_L + jZ_s \tan \theta_s}. \quad (1)$$

When the input impedance  $Z_{in}$  is equal to the characteristic impedance  $Z_a$  of the microstrip line "a", the feeding network can be well matched. We set the input impedance  $Z_{in}$  equal to the antenna radiation impedance  $Z_L$ . So the length of the shorting slotline  $\theta_s$  and the length of "b" segment  $\theta_b$  are

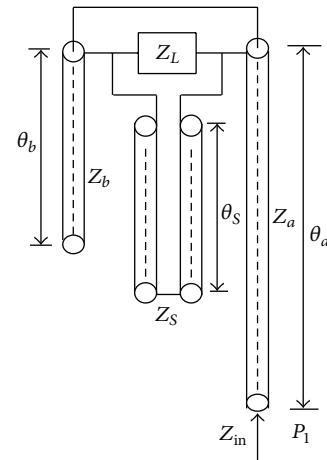


FIGURE 2: The equivalent circuit of the microstrip integrated balun.

both setting to a quarter waveguide wavelength. So formula (1) can be rewritten as

$$Z_{in} = Z_L. \quad (2)$$

The current in "a" segment of the integrated balun is a pure travelling wave, and the current in "b" segment is a standing wave. So we can suppose that the cross-polarization radiation of this antenna is mainly produced by the sum of the cross-polarized radiation of the "a" segment and the "b" segment.

To verify that the cross-polarization is mainly radiated by the microstrip integrated balun, the radiation of the dipole needs to be restrained. Meanwhile, the current distribution

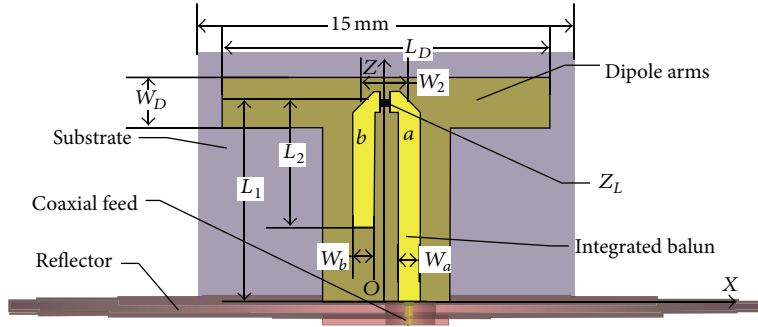


FIGURE 3: Geometry of the modified model.

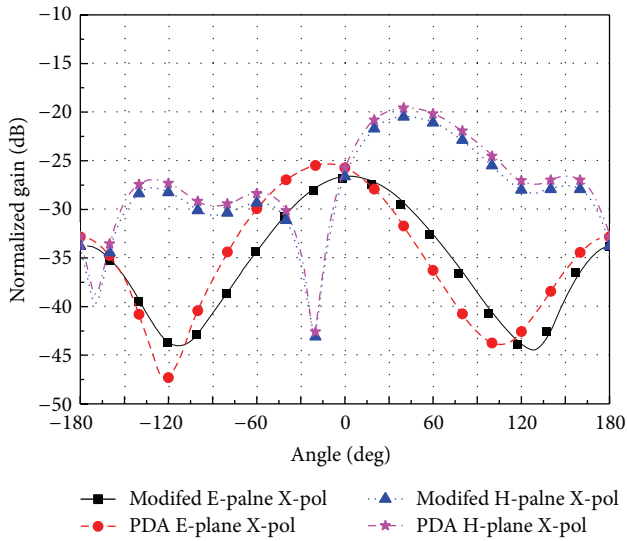


FIGURE 4: Cross-polarization radiation pattern of the conventional PDA and modified model at 10 GHz.

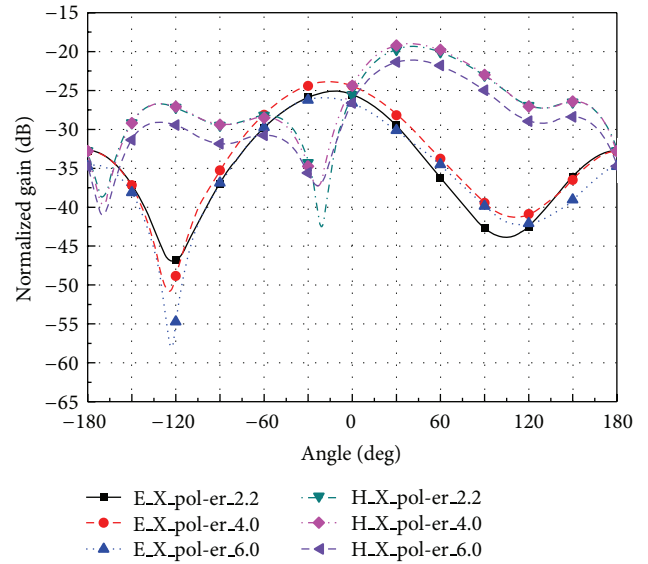


FIGURE 5: Cross-polarization pattern with different relative permittivity.

of the microstrip integrated balun should be well remained. Firstly, the shorting slotline is filled with metal. So the radiation from dipole is suppressed, and moreover, the boundary condition can be well maintained. Secondly, a narrow slot is cut at the middle of the microstrip integrated balun, and then an impedance element with impedance  $Z_L$  is placed in this slot. According to the equivalent circuit analysis above, the current distribution in the integrated balun will be maintained. The geometry of the modified model is shown in Figure 3.

The H-plane and E-plane cross-polarization radiation patterns of the conventional PDA and the modified model are compared in Figure 4. It shows that both H-plane cross-polarization and E-plane cross-polarization of the modified model agreed well with the conventional PDAs. Because the coupling effect between the slotline and the integrated balun is considered in the modified model, the cross-polarization levels are a little bit lower than the conventional PDAs. These results prove that the cross-polarization of the microstrip integrated balun-fed PDA is mainly radiated by the microstrip integrated balun.

### 3. Cross-Polarization Varies with Substrate Parameters

To design a PDA, the selection of the substrate is very important. While the parameters of the substrate are decided, the geometry of this antenna can be decided too. For example, when the substrate parameters are obtained, the width and the waveguide wavelength of the microstrip line can be calculated [14] at a given frequency (10 GHz in this paper). The thickness and the relative permittivity are the two key parameters, so in this section we will analyze the relations between the cross-polarization and these two substrate parameters, respectively.

*3.1. Cross-Polarization Varies with the Substrate Relative Permittivity.* In Table 1, we keep the substrate thickness  $T = 0.5$  mm, and then some main dimensions are calculated at 10 GHz with different relative permittivity  $\epsilon_r$  (2.2, 4.0, and 6.0). The corresponding cross-polarization far-field patterns are shown in Figure 5. And the cross-polarized levels versus

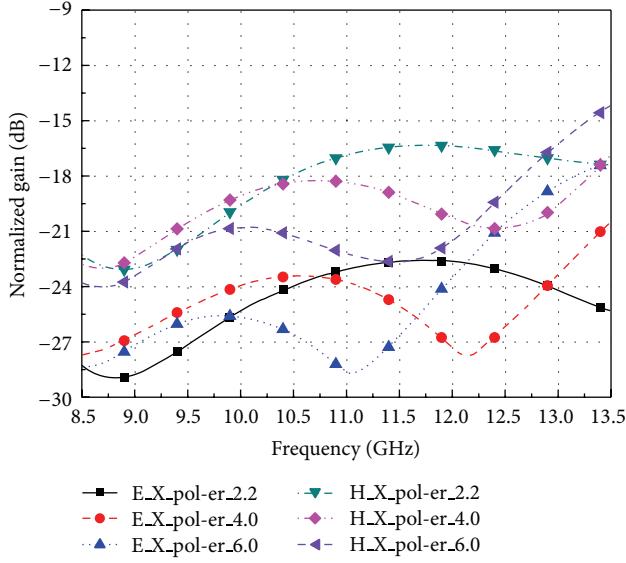


FIGURE 6: Cross-polarized level versus frequency with different relative permittivity.

TABLE 1: Dimensions vary with the relative permittivity.

er	$L_2$ (mm)	$W_a$ (mm)	$L_S$ (mm)	$L_D$ (mm)
2.2	5.0	0.87	6.83	13.6
4	3.9	0.54	5.88	12.6
6	3.3	0.37	5.14	11.5

frequency with different relative permittivity are plotted in Figure 6. As we can see, the cross-polarization varies little with the substrate permittivity. And there is no certain relationship between the cross-polarization and the substrate permittivity. The higher relative permittivity can increase the electrical length between the microstrip line and the ground, so more energy can be released. But the higher relative permittivity also reduces the geometrical size of the microstrip line, so the radiation ability will be weakened. Due to these two reasons, the cross-polarization cannot be suppressed by changing the substrate permittivity.

**3.2. Cross-Polarization Variations with the Substrate Thickness.** In Table 2, we keep the substrate relative permittivity on 2.2, and then some main dimensions are calculated at 10 GHz with different substrate thicknesses (0.3 mm, 0.5 mm, and 0.7 mm). The corresponding cross-polarization far-field patterns are shown in Figure 7, and the cross-polarized levels versus frequency with different substrate thicknesses are plotted in Figure 8. The results show that the cross-polarization levels are reduced while the substrate thickness is thinned. The cross-polarized levels have about 5 dB increase throughout the band while the substrate thickness varies from 0.3 mm to 0.7 mm. This is because the thinner the substrate is, the less the energy can be radiated from the microstrip integrated balun. However, the substrate thickness cannot be too thin, or the antenna mechanical performance will be too weak for application.

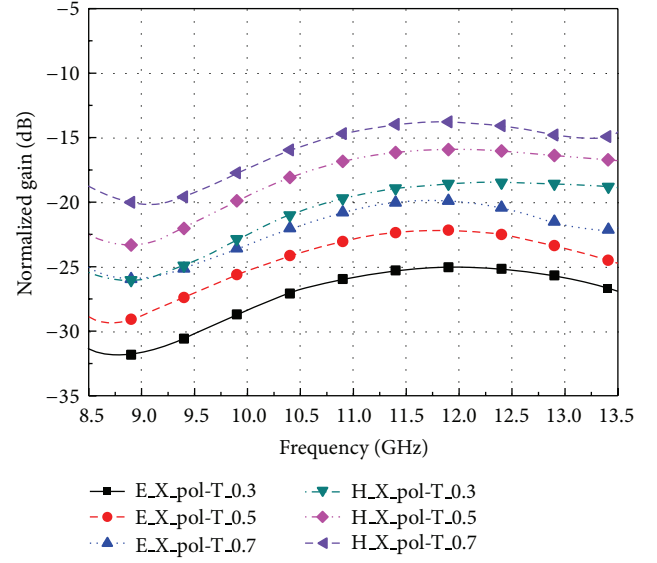


FIGURE 7: Cross-polarized levels versus frequency with different substrate thicknesses.

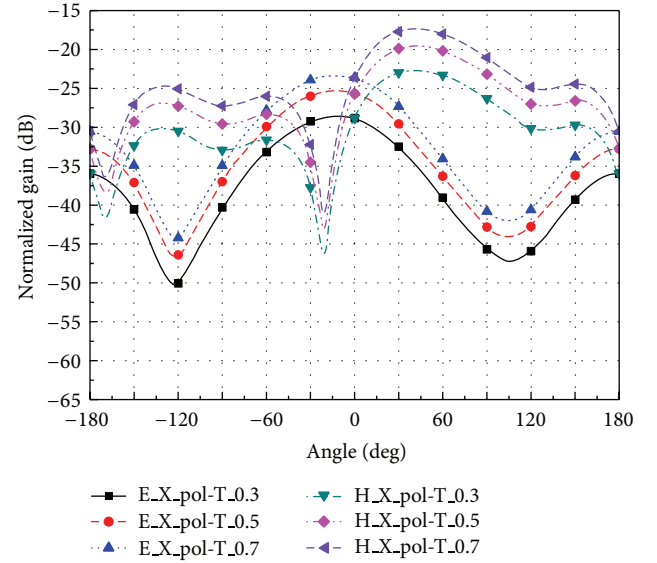


FIGURE 8: Cross-polarization far-field pattern with different substrate thicknesses.

TABLE 2: Dimensions vary with the substrate thickness.

$T$ (mm)	$L_2$ (mm)	$W_a$ (mm)	$L_S$ (mm)	$L_D$ (mm)
0.3	5.0	0.52	6.98	13.9
0.5	5.0	0.87	6.83	13.6
0.7	5.0	1.24	6.75	13.4

According to the above study, we can conclude that the cross-polarization of the microstrip integrated balun-fed PDA is mainly radiated from the microstrip integrated balun, and thinning the substrate can reduce the cross-polarization level. But the suppression of the cross-polarization is very limited.

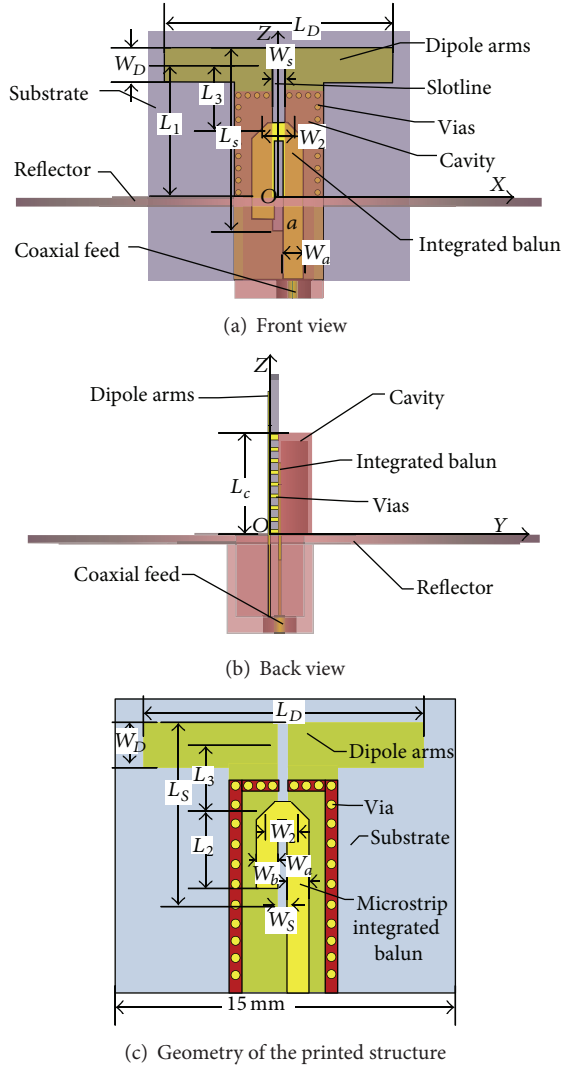


FIGURE 9: Antenna configuration.

#### 4. Configuration of the Improved Antenna

In this section we propose a novel structure to greatly suppress the cross-polarization. The improved structure is shown in Figure 9. Figures 9(a) and 9(b) show the front view and side view of the antenna, respectively. Figure 9(c) shows the geometry of the printed dipole. The microstrip integrated balun is moved down  $L_3$ . The microstrip integrated balun is enclosed by a slotted cavity with a height  $L_c$ . This cavity is formed by a semicylinder, a series of vias, and the ground of the microstrip integrated balun. The vias are closed to each other. So the EM-field in the working band cannot leak from the substrate side. The width of the slotline is equal to the width of the shorting line. So the radiation EM-field of the microstrip integrated balun is transformed by these slots. The E-field on the slot is parallel to the dipole arms, so the radiation polarization direction of the slot is parallel to the main polarization direction of the dipole. And the cross-polarization could be greatly suppressed. The attractive

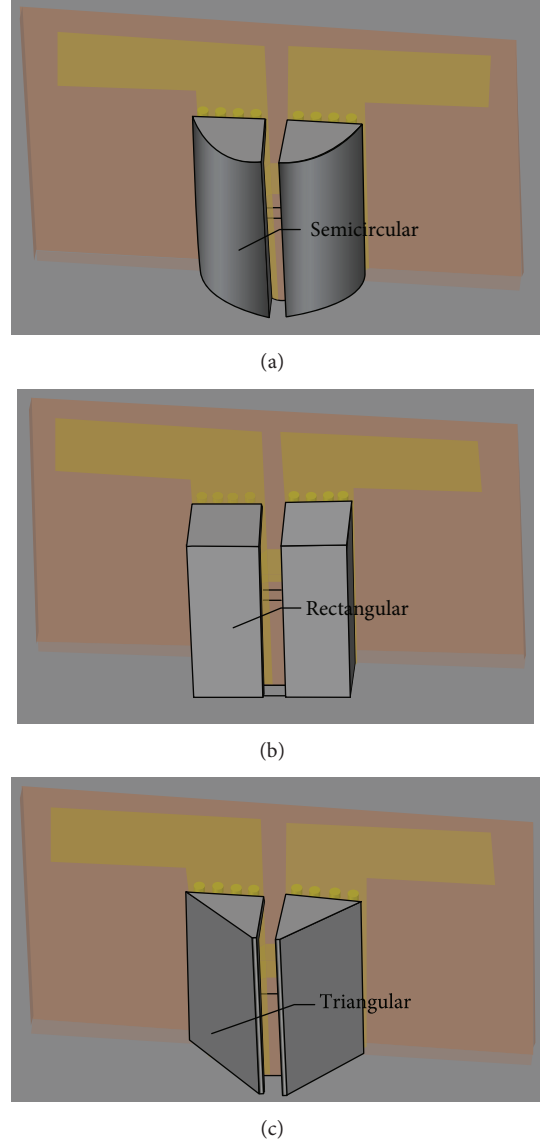


FIGURE 10: Three different kinds of slotted cavities.

features of this proposed structure will be verified by the following simulations and measurements.

The cross-polarized levels of three different slotted cavities, as shown in Figure 10 (semicircular, rectangular, and triangular), are compared. The results are shown in Figure 11. It shows that the gains throughout the band are the same. And compared to the conventional PDA (analyzed in foregoing section), all these results have lower cross-polarized levels. Figure 11 also shows that the triangular and semicircular cavities have better cross-polarized level than the rectangular one. This is due to the fact that the triangular and semicircular cavities have taper boundary condition, and such boundaries have smaller coupling effects with the dipole arms than the rectangular boundary. Then the Y-directional E-field is weaker. So the cross-polarization component can be greatly suppressed.

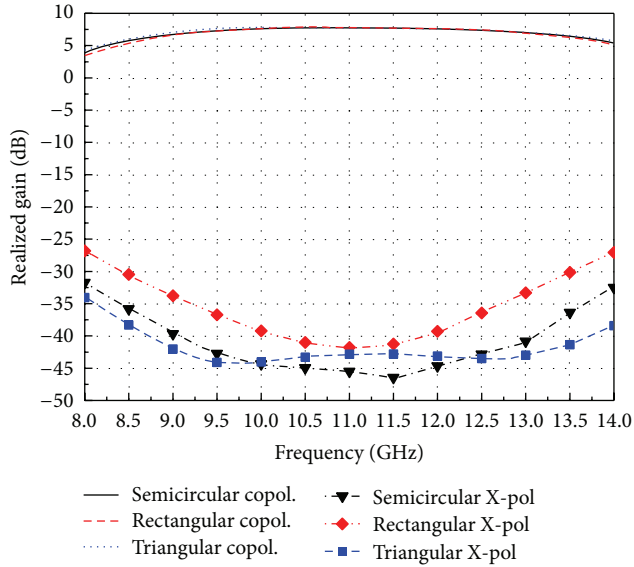
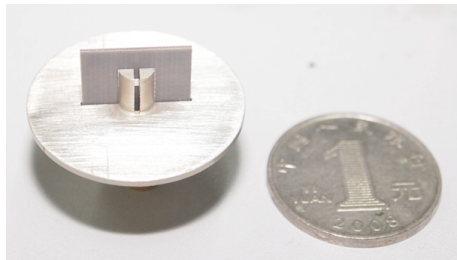
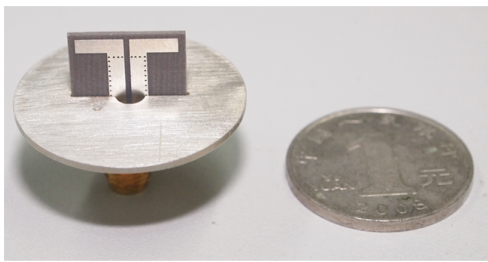


FIGURE 11: Main polarized levels and cross-polarized levels versus frequency with different slotted cavities.



(a)



(b)

FIGURE 12: Photo of the fabricated antenna.

## 5. Fabrication and Test

This improved antenna is fabricated, as shown in Figure 12. The dipole arms and balun are printed on a dielectric substrate with relative permittivity  $\epsilon_r = 2.2$ , thickness  $T = 0.5$  mm, and loss tangent of 0.001. The circular ground plane with a diameter of 30 mm is placed below the dipole arms. And some main dimensions are listed as follows:  $L_D = 13$  mm,  $W_D = 2$  mm,  $L_S = 10.5$  mm,  $W_S = 0.7$  mm,  $W_a = 1.2$  mm,  $W_2 = 1.8$  mm,  $L_1 = 8.0$  mm,  $L_3 = 4$  mm, and  $L_C = 6.5$  mm.

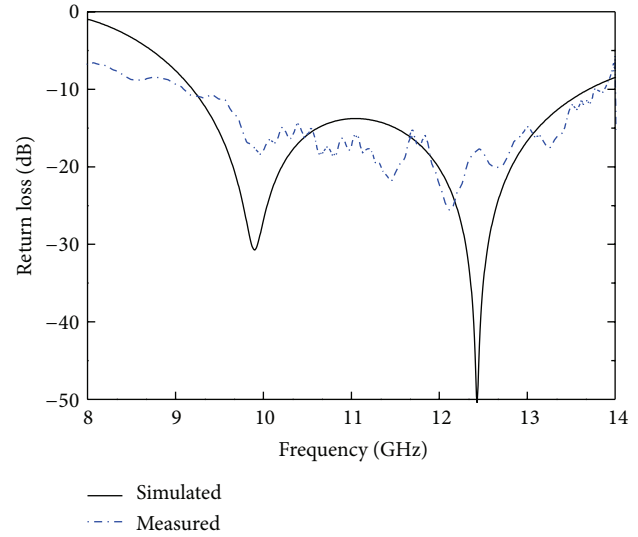


FIGURE 13: Return loss versus frequency.

Figure 13 shows the simulated and measured return loss in solid line and dashed line, respectively. The results show that  $-10$  dB return loss bandwidths are wider than 40%. It is observed that this improved structure can maintain the wide bandwidth feature.

The E-plane and H-plane radiation patterns at 10 GHz are plotted in Figures 14(a) and 14(b), respectively. It is observed that the measured copolarized radiation patterns in both E-plane and H-plane agreed well with the simulated results. But the measured E-plane and H-plane cross-polarized pattern are about 5 dB and 18 dB higher than the simulated result, respectively. This is because the cross-polarized level probably reaches to the lower limit of the measured system.

Figure 15 plots the realized gain and the cross-polarization levels (the maximum cross-polarization level of the E-plane and H-plane in the beam is between  $-90^\circ$  and  $90^\circ$ ) versus frequency. It shows that both simulated and measured results have even wider 3 dB realized gain bandwidth than the  $-10$  dB return loss bandwidth. The tested cross-polarization level is almost below  $-35$  dB at the band (8.5–13.5 GHz).

## 6. Conclusion

An equivalent model for analyzing the cross-polarization of the microstrip integrated balun-fed PDA is presented. And the cross-polarizations of the equivalent model and the conventional model are compared. The E-plane and H-plane cross-polarization patterns agreed well with the conventional one. It is demonstrated that the cross-polarization is mainly radiated from the microstrip integrated balun rather than the dipole itself. The cross-polarization varying with the substrate parameters of thicknesses and relative permittivity is analyzed. The results show that the cross-polarized level can be reduced by thinning the substrate, but the cross-polarization suppression is very limited. And the variation

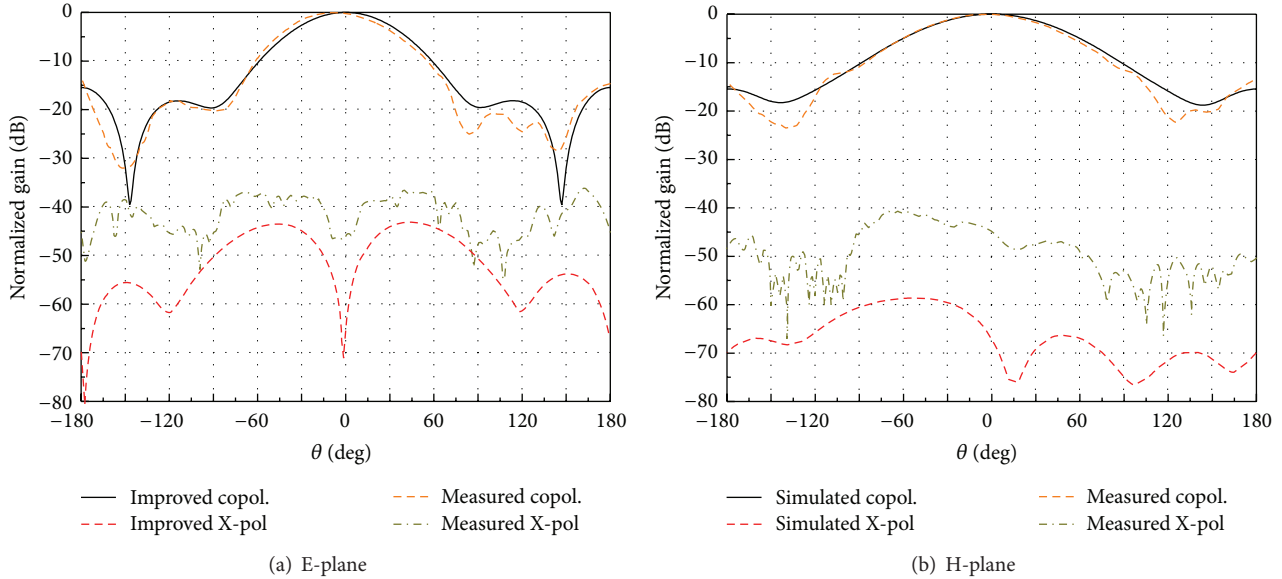


FIGURE 14: Far-field pattern at 10 GHz.

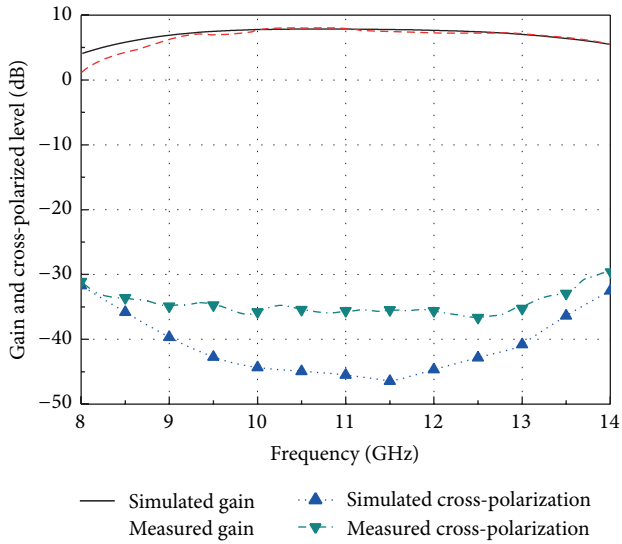


FIGURE 15: Realized gain and the cross-polarization level versus frequency.

of the substrate permittivity has few effects on the cross-polarization. In order to meet the low cross-polarization demands of some applications, such as the low sidelobe arrays and dual polarized arrays, an improved printed dipole element is designed. The microstrip integrated balun is enclosed by a center slotted cavity. And three different kinds of slotted cavities are compared. The simulated results show that the taper boundary (triangular or semicircular) can possess better low cross-polarized performance. An antenna with semicircular cavity is fabricated and tested. The simulated and measured results are compared. It achieves a relative bandwidth wider than 40% and a cross-polarization level lower than  $-35$  dB within the band. The results show that

this novel structure can maintain the wideband characteristic while the cross-polarization is restrained. This improved microstrip integrated balun-fed PDA can be easily extended to a large array and is suitable for the applications with a low cross-polarization requirement.

### Conflict of Interests

The authors have no conflict of interests.

### Acknowledgment

This paper is partially supported by the National Science Foundation of China (Grant no. 61302017).

### References

- [1] B. Edward and D. Rees, "A broadband printed dipole with integrated balun," *Microwave Journal*, vol. 30, no. 5, pp. 339–344, 1987.
- [2] P. M. Proudfoot, "A printed circuit folded dipole with integrated balun," In-House Report RADC-TR-89-237, 1989.
- [3] R. L. Li, T. Wu, B. Pan, K. Lim, J. Laskar, and M. M. Tentzeris, "Equivalent-circuit analysis of a broadband printed dipole with adjusted Integrated balun and an array for base station applications," *IEEE Transactions on Antennas and Propagation*, vol. 57, no. 7, pp. 2180–2184, 2009.
- [4] Y. Cai, Y. J. Guo, and P.-Y. Qin, "Frequency switchable printed Yagi-Uda dipole sub-array for base station antennas," *IEEE Transactions on Antennas and Propagation*, vol. 60, no. 3, pp. 1639–1642, 2012.
- [5] P. Lindberg, E. Ojefors, Z. Barna, A. Thornell-Pers, and A. Rydberg, "Dual wideband printed dipole antenna with integrated balun," *IET Microwaves, Antennas & Propagation*, vol. 1, no. 3, pp. 707–711, 2007.

- [6] A. Vallecchi, J. R. de Luis, F. Capolino, and F. de Flaviis, "Low profile fully planar folded dipole antenna on a high impedance surface," *IEEE Transactions on Antennas and Propagation*, vol. 60, no. 1, pp. 51–62, 2012.
- [7] Y. Wen, Z. H. Xue, S. M. Yang, W. Ren, and W. M. Li, "Design and analysis of a 3 GHz printed dipole antenna," in *Proceedings of the 4th International Conference on Microwave and Millimeter Wave Technology (ICMMT '04)*, pp. 8–11, Nanjing, China, August 2004.
- [8] Z. G. Fan, S. Qiao, J. T. Huangfu, and L. X. Ran, "A miniaturized printed dipole antenna with V-shaped ground for 2.45 GHz RFID readers," *Progress in Electromagnetics Research*, vol. 71, pp. 149–158, 2007.
- [9] M. Scott, "A printed dipole for wide-scanning array application," in *Proceedings of the 11th International Conference on Antenna and Propagation*, vol. 1, no. 480, pp. 37–40, Manchester, UK, 2001.
- [10] K.-L. Wong, F.-R. Hsiao, and C.-L. Tang, "A low-profile omnidirectional circularly polarized antenna for WLAN access point," in *Proceedings of the IEEE Antennas and Propagation Society Symposium*, vol. 3, pp. 2580–2583, Monterey, Calif, USA, June 2004.
- [11] H.-R. Chuang and L.-C. Kuo, "3-D FDTD design analysis of a 2.4-GHz polarization-diversity printed dipole antenna with integrated balun and polarization-switching circuit for WLAN and wireless communication applications," *IEEE Transactions on Microwave Theory and Techniques*, vol. 51, no. 2, pp. 374–381, 2003.
- [12] Z.-W. Zhou, S.-W. Yang, and Z.-P. Nie, "A novel broadband printed dipole antenna with low cross-polarization," *IEEE Transactions on Antennas and Propagation*, vol. 55, no. 11, pp. 3091–3093, 2007.
- [13] W. K. Roberts, "A new wide-band balun," *Proceedings of the IRE*, vol. 45, no. 12, pp. 1628–1631, 1957.
- [14] R. K. Hoffman, *Handbook of Microwave Integrated Circuits*, Artech House, Norwood, Mass, USA, 1987.

## Research Article

# A New Agile Radiating System Called Electromagnetic Band Gap Matrix Antenna

**Hussein Abou Taam,<sup>1</sup> Moustapha Salah Toubet,<sup>1</sup> Thierry Monediere,<sup>1</sup> Bernard Jecko,<sup>1</sup> and Mohammad Rammal<sup>2</sup>**

<sup>1</sup> OSA Department, XLIM, UMR CNRS 7252, 87000 Limoges, France

<sup>2</sup> GRIT Department, IUT, Lebanese University, Saïda, Lebanon

Correspondence should be addressed to Hussein Abou Taam; [hk\\_doc@hotmail.com](mailto:hk_doc@hotmail.com)

Received 16 October 2013; Revised 20 February 2014; Accepted 24 February 2014; Published 25 March 2014

Academic Editor: Xiuping Li

Copyright © 2014 Hussein Abou Taam et al. This is an open access article distributed under the Creative Commons Attribution License, which permits unrestricted use, distribution, and reproduction in any medium, provided the original work is properly cited.

Civil and military applications are increasingly in need for agile antenna devices which respond to wireless telecommunications, radars, and electronic warfare requirements. The objective of this paper is to design a new agile antenna system called electromagnetic band gap (EBG) matrix. The working principle of this antenna is based on the radiating aperture theory and constitutes the subject of an accepted CNRS patent. In order to highlight the interest and the originality of this antenna, we present a comparison between it and a classical patch array only for the (one-dimensional) 1D configuration by using a rigorous full wave simulation (CST Microwave software). In addition, EBG matrix antenna can be controlled by specific synthesis algorithms. These algorithms use inside their optimization loop an analysis procedure to evaluate the radiation pattern. The analysis procedure is described and validated at the end of this paper.

## 1. Introduction

A generic EBG antenna consists of a cavity created by a frequency selective surface (FSS) at the top and a metallic ground plane at the bottom. The energy is coupled to the cavity using a fed antenna such as a dipole, slot, or patch [1, 2]. The EBG antenna has aroused a growing interest of researchers in the last few years due to its capacity to enhance the directivity of a single source, its potentiality in beam forming, its dual-band frequency, bandwidth enhancement, and its polarization diversity [3–6]. Among the papers found in different literatures, a recent study presented in [7] showed that it is possible to limit the radiating aperture of an EBG antenna by inserting 2 metallic walls (along a single direction) in order to obtain an elliptical radiating aperture. Therefore, the proposed idea in this paper is to limit the radiating aperture by inserting 4 metallic walls (in two perpendicular directions) at the antenna's edges in order to obtain a homogeneous square aperture. This new structure is called "Pixel" and constitutes the elementary antenna of the EBG matrix.

The aim of this work is to present an EBG matrix design. The working principle of this antenna constitutes the subject

of an accepted CNRS patent [8]. The EBG matrix is based on the radiating aperture theory which is not the case in different array concept that is based on an ordinary array law. In order to highlight the interest and the originality of the EBG matrix, a comparison is made between a 1D EBG matrix and a linear classical antenna array (e.g., patch array). This comparison shows that the EBG matrix is a loosely coupled system and it is very efficient for beam steering applications.

In addition, the paper shows that the agile EBG matrix can be controlled by using specific algorithms in order to respond to imposed radiation objectives. These algorithms use inside their optimization loop an analysis procedure to evaluate the radiation patterns, for each iteration. The analysis procedure is described and validated in order to verify the EBG matrix working principle.

## 2. Working Principle of the Antenna

The EBG matrix works similarly to a radiating aperture antenna. The concept is based on generating a radiating surface for any desired shape. Based on the radiating aperture

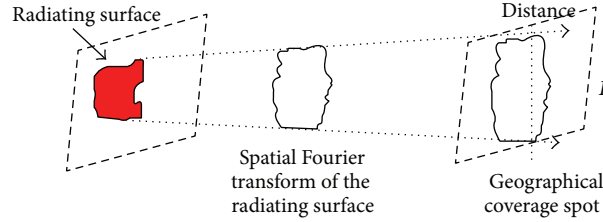


FIGURE 1: Schematic representation of the radiating aperture antenna working principle.

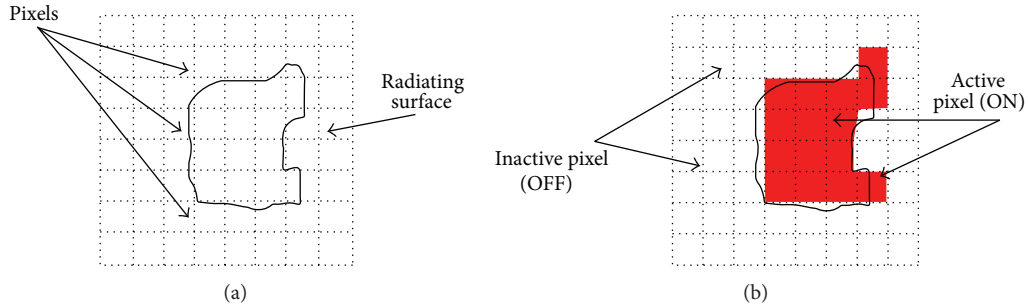


FIGURE 2: (a) Radiating surface pixilated by the antenna elements (b) and generation of the desired radiating surface.

theory, this radiating surface creates radiation patterns to ensure a given geographical coverage (Figure 1). To recall, the general analytical equation of the radiated electric field obtained at an observation point  $P$  of the space from a radiating surface is presented in (1). Equation (2) looks like a spatial Fourier transform which transforms the  $(x, y)$  coordinates of the near electric field distribution  $E_s(x, y)$  existing on the radiating surface into  $(\theta, \varphi)$  ones on the space at the point  $P$  (equivalent principle).

Indeed, the desired radiating surface must be pixilated by introducing elementary antenna pixels which form a planar matrix antenna (Figure 2(a)). The desired radiating surface is built by activating the corresponding pixels as shown in Figure 2(b). In the simple case, the pixels are fed using only switch devices (ON State: red pixels and OFF State: white pixels). However, in a sophisticated case, each pixel can be fed by given weights in amplitude and phase using variable amplifiers and variable phase shifters. Consider the following:

$$\vec{E}(p) = \frac{jk}{4\pi} \psi(R) (1 + \cos \theta) \left( \cos \varphi \vec{e}_\theta - \sin \varphi \vec{e}_\varphi \right) F, \quad (1)$$

$$F = \iint_s E_s(x, y) e^{j(kx \sin \theta \cos \varphi + ky \sin \theta \sin \varphi)} ds. \quad (2)$$

In order to generate any desired shape of the radiating surface, it is very advantageous to have an antenna system which is formed by special radiating elements. These elements, according to their states, should give a good approximation of the desired radiating surface. Indeed, each element must generate a square and quasi-uniform radiating aperture which is limited to the element's dimensions. Therefore, an EBG antenna called "Pixel" is designed and presented in the next section.

### 3. Elementary Pixel

The studied EBG elementary antenna is similar to a classical EBG antenna acting as a resonant cavity formed between the ground plane and the frequency selective surface (FSS) placed above it in the  $z$  direction [1, 2], as shown in Figure 3. It usually generates on its roof a circular radiating aperture as shown in Figure 3(c). The feeding system is constituted of a patch placed above the dielectric substrate (permittivity = 4.4) and located at the EBG antenna center.

The aim is to confine the electric field distribution in the cavity, in order to modify the circular radiating aperture into a homogenous square one. To carry this out, four vertical metallic walls are inserted in the resonant cavity at the edges (Figure 4(a)). This is possible due to the radial evanescent mode existing in the EBG cavity prohibiting thereby any catastrophic transverse resonance. A square radiating aperture is obtained with a good uniformity (Figure 4(b)). The EBG cavity with metallic walls is called "pixel" and constitutes the elementary antenna of the EBG matrix which is presented in the next section.

### 4. Conception of EBG Matrix

The proposed idea of designing an EBG matrix is to associate several joint identical pixels along two directions to form 2D EBG matrix or along a single direction to form 1D EBG matrix. This approach is illustrated in Figures 5(a) and 5(b) that show, respectively, 2D EBG matrix formed by  $N * M$  pixels and 1D EBG matrix formed by  $N * 1$  pixels.

Therefore, two designed configurations are presented for the EBG matrix antenna. They can be used to form any desired shape for the radiating surface corresponding to an imposed radiation pattern for geographical coverage

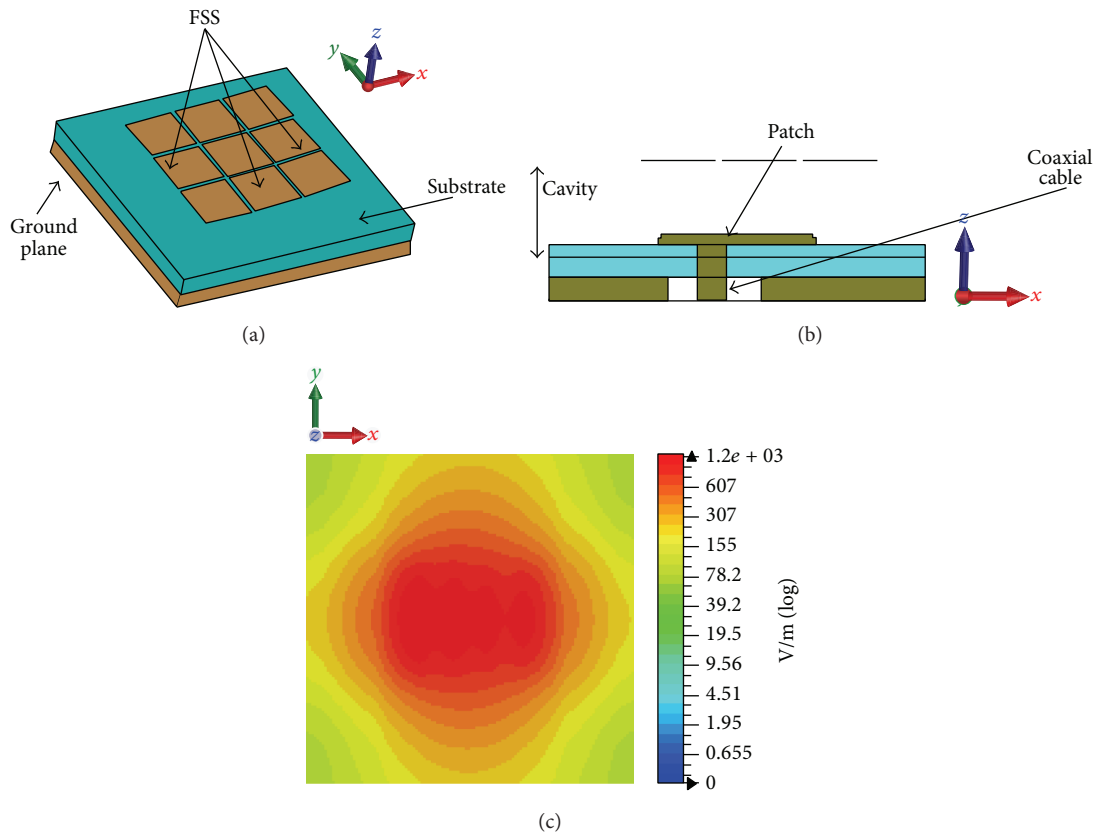


FIGURE 3: Elementary EBG antenna, perspective view (a), inside view (cut-plane at the middle along  $(0y)$ ) (b), and associated near electric field distribution  $E_s(x, y)$  (c).

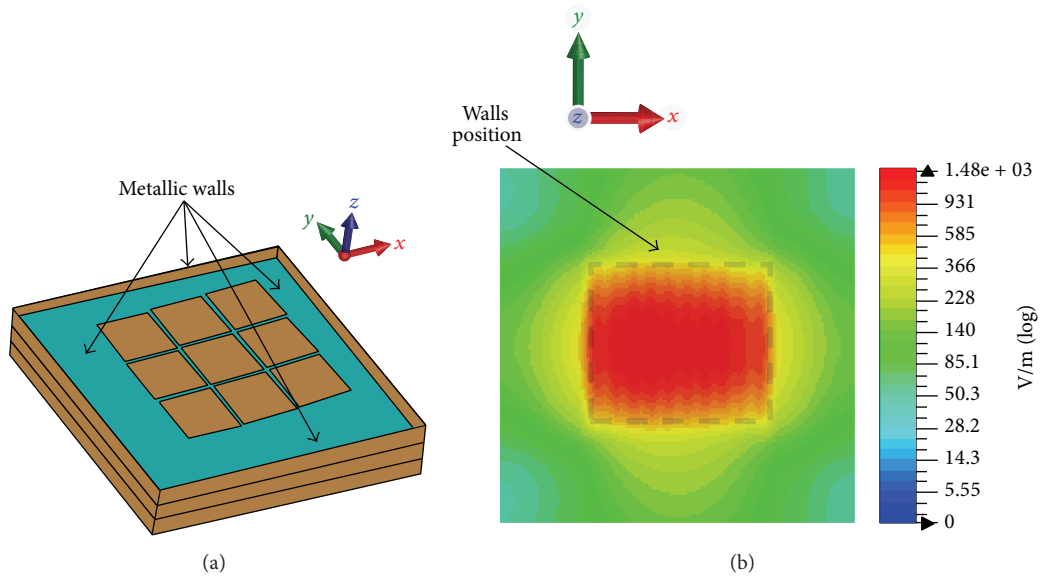


FIGURE 4: Elementary EBG antenna with walls (a) and associated square radiating aperture with quasi-uniform electric field distribution  $E_s(x, y)$  (b).

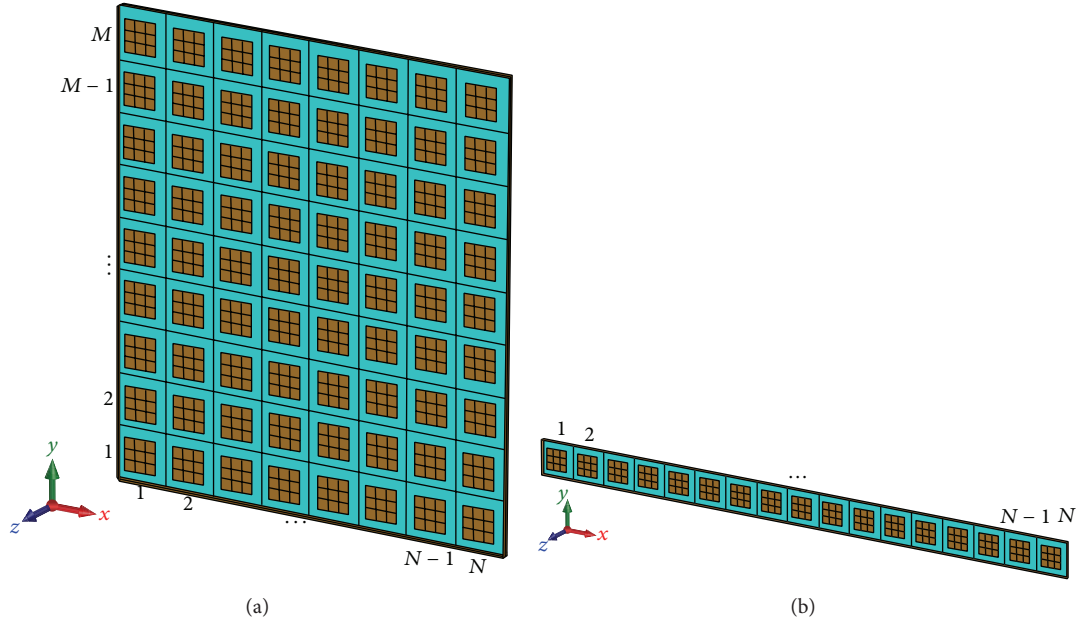


FIGURE 5: 2D EBG matrix formed by  $N * M$  pixels (a) and 1D EBG matrix formed by  $N * 1$  pixels (b).

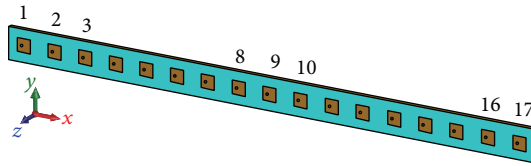


FIGURE 6: Patch array formed by 17 elements spaced by  $0.5 \lambda$ .

application. Nevertheless, this paper presents a study on the second configuration (Figure 5(b)) in order to highlight the interest and the originality of the EBG matrix, especially for beam steering applications. A comparison is made between a 1D EBG matrix ( $N = 17$ ; element spacing =  $0.5 \lambda$ ) and a classical linear array (e.g., patch array).

## 5. Special Radiating Surface for EBG Matrix

For a linear patch array (Figure 6) which presents the same elements number (17 elements) and the same element spacing ( $0.5 \lambda$ ) of the 1D EBG matrix (Figure 5(b)), the elementary radiating aperture overlaps the neighboring elements, which induces a significant mutual coupling. The originality of the 1D EBG matrix is to limit each elementary radiating aperture at the pixel's dimensions in order not to disturb the neighboring pixels [9]. In addition, the formed radiating aperture is square, equiamplitude, and equiphase along the pixel's dimensions (Figure 7(b)), which is not the case for the patch array (Figure 7(a)). A global uniform radiating surface (equiamplitude and equiphase) is formed by the association of the jointed and limited elementary radiating apertures when all the pixels are fed (Figure 7(c)). 1D EBG matrix does not act like a classical array but it is considered a special radiating surface. Noting that, the radiation pattern can be

practically obtained, by a spatial Fourier transform (1) of the radiating surface, according to the radiating aperture theory.

The first observation which appears in the 1D EBG matrix is the weak mutual coupling between neighboring pixels for small element spacing [9]. Indeed, the presence of metallic walls at the pixel's edges and the presence of the EBG mode inside each pixel's cavity insure a good isolation between neighboring pixels, making them independent from each other. The feeding of the central element (number 9) of the two structures gives us the matching coefficients of the central element (Figure 8(a)) and the mutual coupling level with the neighboring ones (Figure 8(b)). In addition, the obtained results are compared with a 1D array of cavity-backed patches to illustrate the effect of the EBG mode inside the pixel's cavity. The results show that the mutual coupling level for the EBG matrix is much better than the other structures. The mutual coupling level for the EBG matrix is less than  $-24$  dB at the working frequency of 8 GHz.

In the next section, we present an important property which appears in 1D EBG matrix, which is the possibility to achieve a good beam steering along a wide angular range.

## 6. Beam Steering with EBG Matrix

In order to highlight the advantage of the EBG matrix in the beam steering application, a comparison is made between

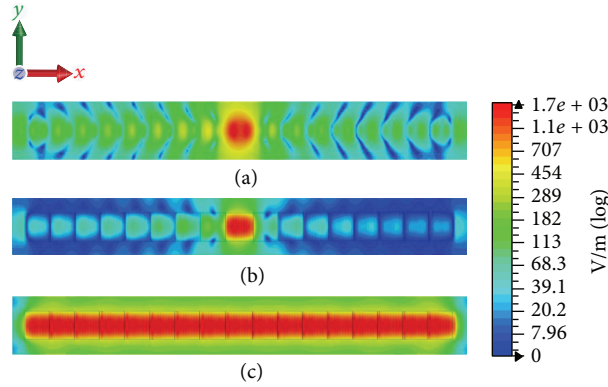


FIGURE 7: Cartography of electric field distribution: (a) central patch is fed; (b) central EBG pixel is fed; (c) all EBG pixels of the matrix are fed.

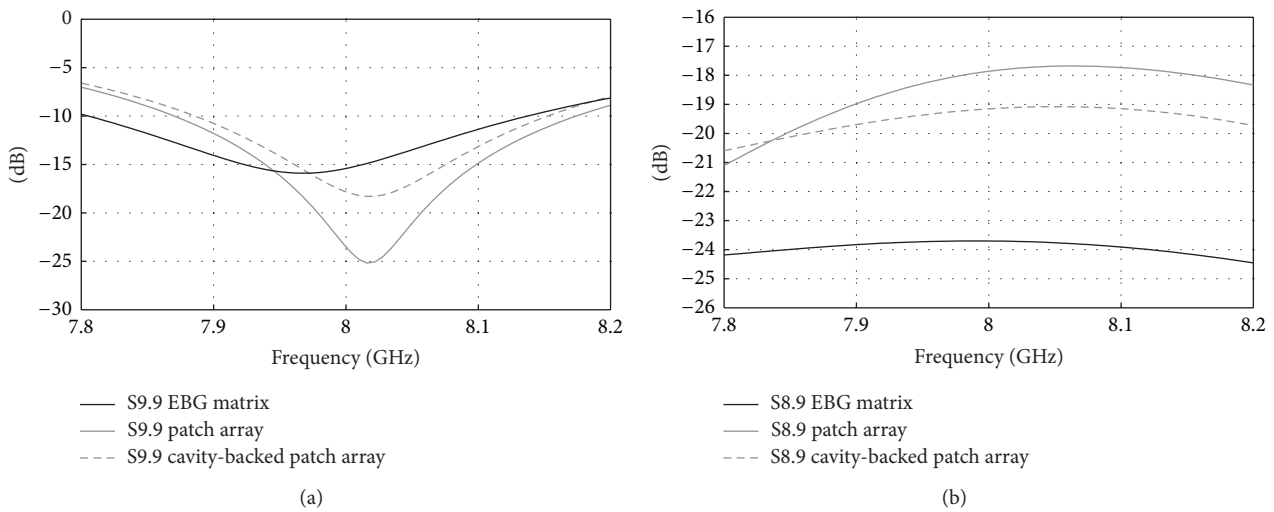


FIGURE 8: (a) Matching coefficients of the central element (b) and coupling coefficients between the central element and the first left neighboring.

the two structures (EBG matrix and patch array) already presented in the previous section. The main idea is to show that the 1D EBG matrix is an efficient system for high scanning angles.

Figure 9(a) presents the radiation patterns of the two structures when each radiating element is fed in equiamplitude and equiphase. In this case, quasi-identical radiation patterns are obtained with the same gain of 18 dB at the broadside direction due to the fact that the two structures have the same dimensions. If the main lobes are steered to a high angle of 70°, the results are different (Figure 9(b)). The maximum gain is more conserved with the EBG matrix than the patch array. Indeed, the gap of the gain between the ones obtained for  $\theta$  equal to 0° and  $\theta$  equal to 70° is 3 dB for the 1D EBG matrix and 7 dB for the patch array. Concerning the side lobe levels, they are more reduced for the 1D EBG matrix for beam steering case (Figure 9(b)). In order to be more explicit and in the case of EBG matrix, the side lobes levels (SLL) are lower than 11 dB relatively to the maximum gain. However, in the case of patch array, the SLL are lower than 7 dB relatively to the maximum gain.

Finally, the back radiation is also reduced with a 1D EBG matrix. It is, respectively, lower than 13 dB and 6 dB, relatively to the maximum gain for the EBG matrix and the patch array. All these performances are due to the radiating surface magnitude of the EBG matrix which is less degraded than the patch array design after beam steering, because of the isolation between the pixels and the better conservation of the radiating surface efficiency obtained at the broadside direction which is already presented in Figure 7(c).

Thus, Figure 10 presents the maximum gain value evolution versus the scanning angle value for the two structures to fully understand this advantage. These results show a better conservation of the maximum gain for the EBG matrix regardless of the scanning angle, and more specifically for high scanning angles.

### 7. Analysis Procedure

As all agile antenna systems, the EBG matrix antenna can be controlled by using specific synthesis algorithms which will enable the antenna radiation to follow imposed radiation

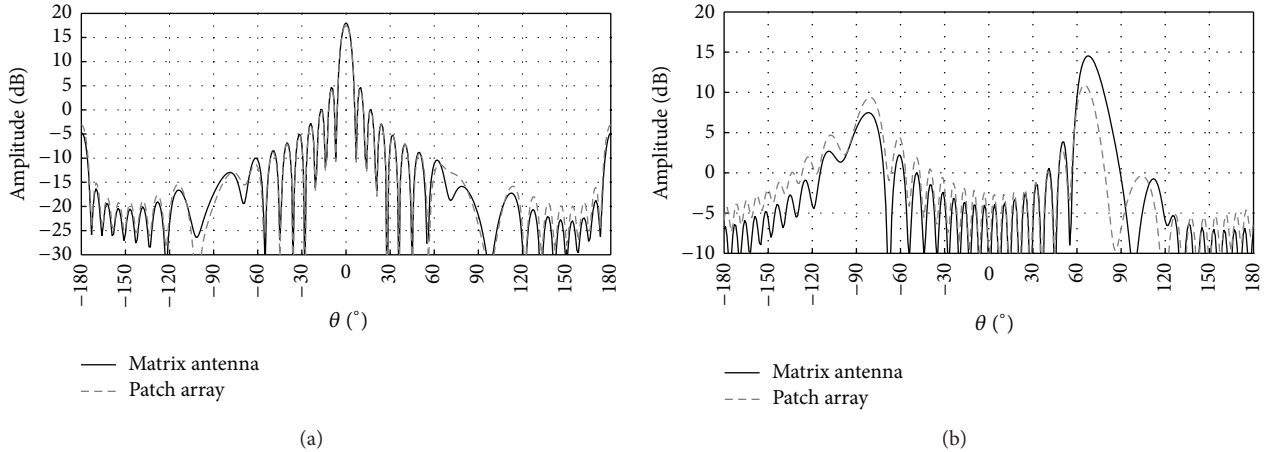


FIGURE 9: Comparison of radiation patterns between EBG matrix and patch array (a) at the broadside direction and (b) after beam steering of  $70^\circ$ .

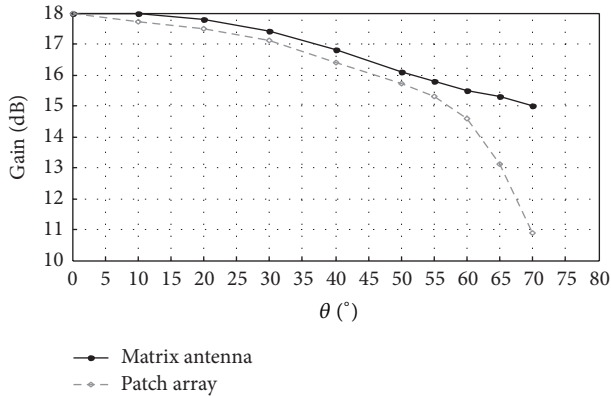


FIGURE 10: Evolution of the maximum gain value versus scanning angle value.

patterns. In the optimization loop of these algorithms, an analysis procedure is necessary to evaluate the radiation pattern, for each iteration. However, it is not possible to use rigorous simulation software inside the synthesis loop due to the time burden. Therefore, it will be necessary to model an efficient analysis tool to replace the rigorous simulation software.

The analysis procedure is based on the radiating aperture theory. The radiation patterns are calculated, according to (1) and (2), from the near electric field distribution  $E_s(x, y)$  existing on the radiating surface. Indeed, the originality of the EBG matrix is that each pixel generates a uniform radiating aperture isolated and independent from the neighboring ones as in Figure 7(b) leading to obtaining of the same elementary radiating apertures  $E_s(x, y)$  regardless of the pixel position. The analysis procedure is modeled by using Matlab software. The analysis code imports the near electric field distribution  $E_s(x, y)$  from one pixel (obtained by rigorous full wave simulation once for all) and evaluates the global radiation pattern of the EBG matrix taking into consideration the weights applied on the input pixels.

Therefore, in order to validate the analysis procedure, a comparison is made between results calculated by the analysis code and others obtained by a rigorous full wave simulation using CST Microwave software. Figure 11 shows two cases of figures (broadside direction in Figure 11(a) and steered direction at  $-50^\circ$  in Figure 11(b)). A perfect agreement is obtained except for the back radiation area due to the fact that the analytical code cannot consider the diffraction at structure edges. However, we would like to mention that the analysis procedure is described and validated but the synthesis algorithm constitutes a future perspective.

## 8. Conclusion

In this paper, a new antenna system called EBG matrix is presented. The principle of this antenna constitutes the subject of an accepted CNRS patent [8]. The originality is the special radiating aperture formed by each pixel of the matrix. The radiating aperture of each pixel is square, equiamplitude, and equiphase regardless of its position in the EBG matrix.

The fact that the radiating aperture is confined in the pixel's cavity and does not run over the pixel's dimensions insures isolation between neighboring elements. Moreover, the later isolation leads to obtaining a low mutual coupling in the EBG matrix making this antenna system more advantageous than the classical antenna array. In addition to that, this paper shows that 1D EBG matrix is a very efficient system for high steering angles, because the main lobe gain is more conserved with accepted side lobes and back radiation levels, making the antenna system more flexible.

The EBG matrix can be controlled by specific synthesis algorithms which use inside their optimization loop an analysis procedure to evaluate the radiation pattern for each iteration. The proposed analysis procedure is based on the radiating aperture theory. It is described and validated in this paper. The synthesis algorithm constitutes for us a future perspective.

Finally, due to the complexity, the number and the cost of the structures considered in this paper were not

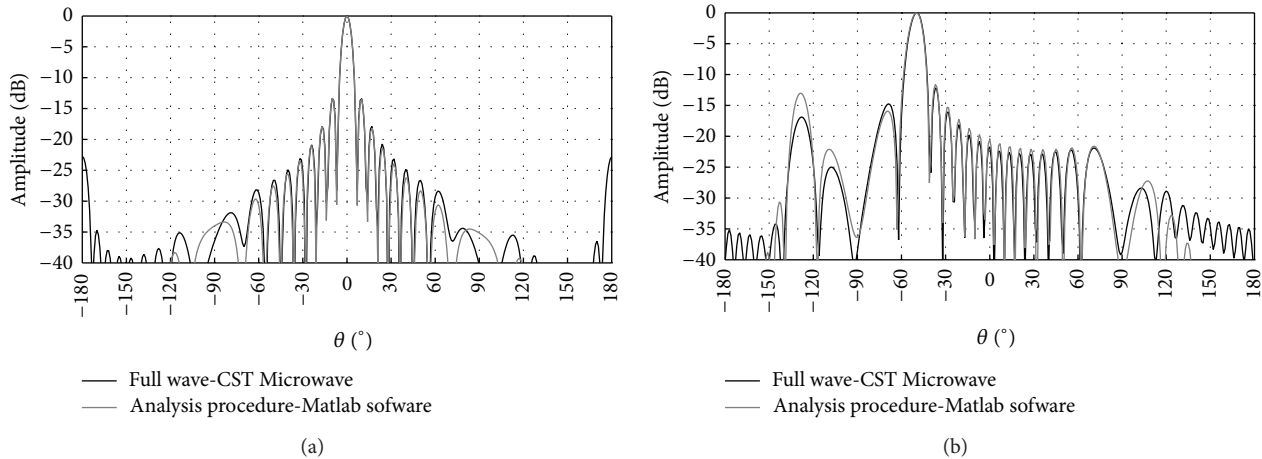


FIGURE 11: Comparison of normalized radiation patterns: (a) broadside radiation and (b) steering radiation at  $-50^\circ$ .

manufactured yet. The presented results are only theoretical and obtained using a full wave simulation (CST Microwave Studio). Therefore, the approach which consists of using simulation software is considered very reliable since several publications [2, 6] show that the measurement results are almost identical to those simulated considering the manufacturing imperfections. This novel design provides more flexibility and can be used in geographical coverage, beam forming, and beam steering applications.

### Conflict of Interests

The authors declare that there is no conflict of interests regarding the publication of this paper.

### References

- [1] N. G. Alexopoulos and D. R. Jackson, "Fundamental superstrate effects on printed circuit antennas," *IEEE Transactions on Antennas and Propagation*, vol. AP-32, no. 8, pp. 807–816, 1984.
- [2] A. P. Feresidis, G. Goussetis, S. Wang, and J. C. Vardaxoglou, "Artificial magnetic conductor surfaces and their application to low-profile high-gain planar antennas," *IEEE Transactions on Antennas and Propagation*, vol. 53, no. 1, pp. 209–215, 2005.
- [3] H. Y. Yang and N. G. Alexopoulos, "Gain enhancement methods for printed circuit antennas through multiple superstrates," *IEEE Transactions on Antennas and Propagation*, vol. 35, no. 7, pp. 860–863, 1987.
- [4] H. Boutayeb and T. A. Denidni, "Metallic cylindrical EBG structures with defects: Directivity analysis and design optimization," *IEEE Transactions on Antennas and Propagation*, vol. 55, no. 11, pp. 3356–3361, 2007.
- [5] Y. J. Lee, J. Yeo, R. Mittra, and W. S. Park, "Design of a Frequency Selective Surface (FSS) type superstrate for dualband directivity enhancement of microstrip patch antennas," in *Proceedings of the IEEE Antennas and Propagation Society International Symposium and USNC/URSI Meeting*, pp. 2–5, Washington, DC, USA, July 2005.
- [6] H. Yi and S.-W. Qu, "A novel dual-band circularly polarized antenna based on electromagnetic band-gap structure," *IEEE Antennas and Wireless Propagation Letters*, vol. 12, pp. 1149–1152, 2013.
- [7] M. Hajj, E. Rodes, D. Serhal et al., "Metallic EBG sectoral antenna for base stations," in *Proceedings of the 19th International Conference on Applied Electromagnetics and Communications (ICECom '07)*, pp. 1–4, September 2007.
- [8] B. Jecko, M. Hajj, R. Chantalat, and M. Salah Toubet, "Antenne élémentaire et antenne réseau mono ou bidimensionnelle correspondante," PCT Patent PCT/EP2012/076509, University of Limoges, Limoges, France, 2013.
- [9] M. Hajj, M. Salah Toubet, Y. Abdallah, R. Chantalat, and B. Jecko, "A novel beam scanning/directivity reconfigurable m-EBG antenna array," *Progress in Electromagnetics Research C*, vol. 29, pp. 55–66, 2012.

## Research Article

# A Broadband Conformal Phased Array Antenna on Spherical Surface

Dan Sun,<sup>1,2</sup> Rong Shen,<sup>1,2</sup> and Xuequan Yan<sup>1,2</sup>

<sup>1</sup> AVIC LEIHUA Electronic Technology Research Institute, No. 796 Liang Xi Road, Jiangsu, Wuxi 214063, China

<sup>2</sup> Aviation Key Laboratory of Science and Technology on AISSS, No. 796 Liang Xi Road, Jiangsu, Wuxi 214063, China

Correspondence should be addressed to Dan Sun; [sun\\_dan@sina.com](mailto:sun_dan@sina.com)

Received 10 October 2013; Revised 29 January 2014; Accepted 24 February 2014; Published 24 March 2014

Academic Editor: Xiuping Li

Copyright © 2014 Dan Sun et al. This is an open access article distributed under the Creative Commons Attribution License, which permits unrestricted use, distribution, and reproduction in any medium, provided the original work is properly cited.

A Ku-band wideband conformal array antenna with  $13 \times 19$  elements is presented in the paper. The array has a spherical structure, and its element is a proximity-coupled stacked patches antenna with a cavity-backed ground plane. The stacked patches and the cavity produce multiple coupled resonances, which enhance the bandwidth of the element extremely. A simulated model with the reasonable dimensions is framed with the coupling analyses, and the effective simulated results and good computing efficiency are obtained simultaneously. The measured results of the center embedded element in the whole array show a bandwidth exceeding 40% (VSWR < 2), which is close to the simulated matching performance.

## 1. Introduction

Recently, active electronically scanned array (AESA) systems have been widely applied in aircrafts. However, the antenna arrays in these systems are basically planar, and it is difficult with these arrays to achieve the integration with platforms. Accordingly, the aerodynamic performance and the RCS of platforms are affected. One effective solution is to employ conformal phased arrays instead of planar arrays. Furthermore, conformal arrays can afford larger beam coverage range besides planar arrays. Hence, the designs of conformal array antennas have been an attractive research field, and many significant investigations have been reported, such as the conformal waveguide slot arrays [1] and the conformal microstrip patch arrays [1–11]. As compared to conformal waveguide slot arrays, conformal microstrip patch arrays have the advantage of lighter weight, smaller size, and better integration with aircrafts. Thus, a clear majority of conformal arrays are built up of microstrip patch antennas. However, most of the arrays in the papers referred to above use conventional microstrip antennas as the elements, and their bandwidths are narrow. Although some of them employ certain techniques for enhancing the bandwidths,

such as aperture-coupling [8], triple patch [9], proximity-coupling with cavity-backed configuration [10], and E-shaped patch [11], the capability of increasing the bandwidths with techniques is limited, and the largest bandwidth achieved in these arrays is only 27.6% [10].

In this paper, we extend the cavity-backed proximity-coupled stacked patches antenna in our previous work [12] into the design of a broadband spherical conformal phased array antenna working in Ku-band. The array antenna consists of 19 single-column arrays with 13 elements. To achieve a wideband response of the embedded elements, the influences of the mutual couplings on the matching are included in the optimization. The measured results of the center embedded element in the prototype array demonstrate that its bandwidth is 42% (VSWR < 2).

## 2. Array Antenna Configuration and Mutual Coupling Analyses

The array antenna is located on a spherical surface with a radius of about 153 mm, which is shown in Figure 1.

In the array, 19 single-column arrays are spaced  $5^\circ$  along the  $\varphi$ -direction, and there are 13 elements spaced  $4^\circ$

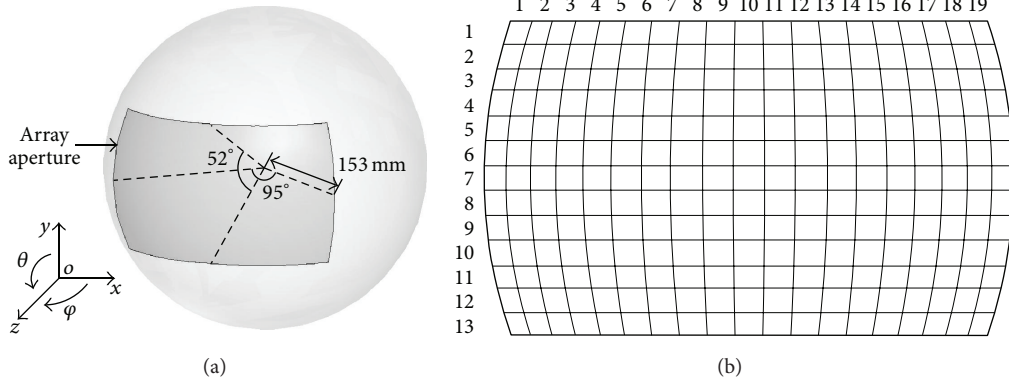


FIGURE 1: Sketch of the Ku-band spherical phased array antenna. (a) Geometry of the array. (b) Locations of the elements.

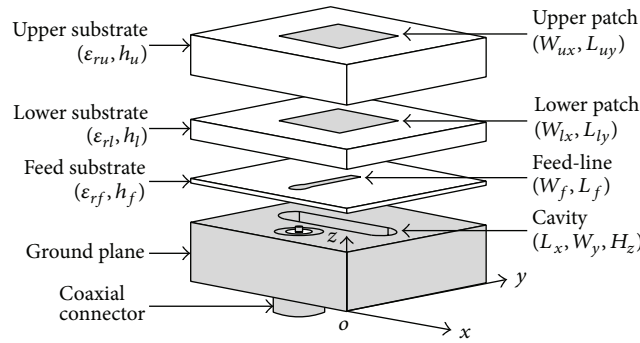


FIGURE 2: Geometry of the antenna element.

along the  $\theta$ -direction in each single-column array. The cross-sections of the conformal array antenna in  $xz$ - and  $yz$ -planes are two sectors with central angles of  $95^\circ$  and  $52^\circ$ , respectively. Its embedded elements are assembled piecewise in a smoothly spherical metallic frame. The polarization of the antenna element is  $\theta$  polarization, whose structure is depicted in Figure 2. The element is composed of two stacked patches, a cavity, a feed-line, and three substrate layers.  $L_f$  is the distance between the open circuit termination of the feed-line with  $W_f$  and the cavity surface center. The coaxial connector and the feed-line are vertically connected. The stacked patches and the cavity are to serve as three radiators with interactions, which affords a broadband solution [12].

Due to the limitation of the computing devices' capability, it is difficult to simulate the whole conformal array antenna with  $13 \times 19$  elements. Hence, it is needed to reduce the simulated array size for improving computing efficiency in case of ensuring the effectiveness of the results. In order to obtain the reasonable simulated array size, the mutual couplings among elements in the seventh single-row array and the tenth single-column array are simulated by HFSS, separately. The elements in the two arrays are the same. Arlon DiClad880 is used as the substrate material. Its dielectric constant is 2.2. The thicknesses of the three substrates are  $h_f = 0.254$  mm,  $h_l = 1.016$  mm, and  $h_u = 2.032$  mm. The other parameters are  $W_{lx} = L_{ly} = 4$  mm,  $W_{ux} = L_{uy} = 4.5$  mm,  $L_x = 7$  mm,  $W_y = 2$  mm,  $H_z = 2.2$  mm,  $W_f = 0.8$  mm,

and  $L_f = 1.3$  mm. The simulated results are revealed in Figure 3. The magnitude of the mutual coupling between the two elements is  $|S_{(i,j),(m,n)}|$ , where  $i$  and  $m$  as well as  $j$  and  $n$  are the row and the column numbers of the elements, respectively.

As can be seen from Figure 2, the  $\varphi$ -directed couplings decay rapidly with the increases of the distances between the two elements, and  $|S_{(7,10),(7,12)}|$  is already lower than  $-22$  dB in the lower frequency band. However, the  $\theta$ -directed couplings do not exhibit a similar behavior. The mutual couplings between the center embedded element and other elements in the tenth single-column array are not decreased obviously with the increases of their distances, and  $|S_{(7,10),(11,10)}|$  is still larger than  $-20$  dB in the lower frequency band. Accordingly, the effects of the mutual couplings on the matching of the embedded element in the  $\theta$ -direction are larger than those in the  $\varphi$ -direction. Considering these circumstances, a simulated array model with three single-column arrays composed of 9 elements is constructed.

### 3. Array Antenna Design and Results

Based on the proposed simulated model, the embedded element is optimized. In the optimization process, the parameters of the three substrates and the width of the feed-line are invariable and their values are the same as the instance in Figure 3. By optimizing other design parameters

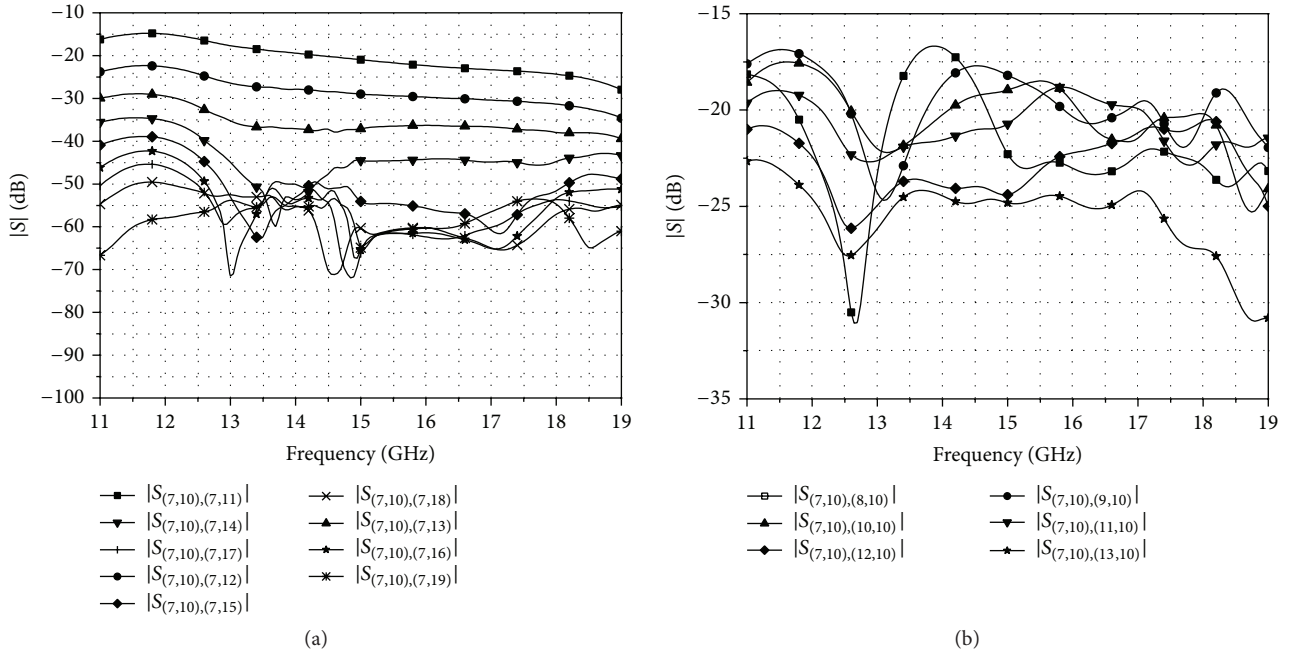


FIGURE 3: Mutual couplings between two separated elements. (a) Seventh single-row array. (b) Tenth single-column array.

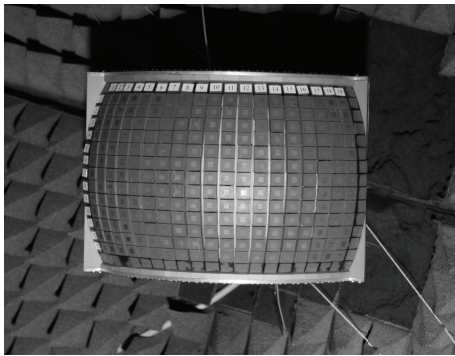


FIGURE 4: Prototype of spherical conformal phased array antenna.

of the embedded element, a great matching performance is achieved. Their values are listed as follows:  $W_{lx} = L_{ly} = 4.25$  mm,  $W_{ux} = L_{uy} = 4.3$  mm,  $L_x = 6$  mm,  $W_y = 1.8$  mm,  $H_z = 2.5$  mm, and  $L_f = 1.3$  mm. With these parameters, a  $13 \times 19$  prototype conformal array antenna is fabricated, which is shown in Figure 4.

Figure 5 shows the measured and the simulated results of the center embedded element VSWR and the magnitude of the mutual couplings between two neighboring elements. It can be seen that the measured bandwidth of VSWR below 2 is from 12 to 18.4 GHz (42.1%) and the simulated bandwidth is from 11.8 to 18.5 GHz (44.2%). Both of the measured and the simulated mutual couplings in the  $\theta$ -direction ( $|S_{(7,10),(8,10)}|$ ) are lower than  $-16$  dB, and the measured and the simulated mutual couplings in the  $\varphi$ -direction ( $|S_{(7,10),(7,11)}|$ ) are both lower than  $-18$  dB. Also, the measured and the simulated results are in agreement, which means it is effective that the

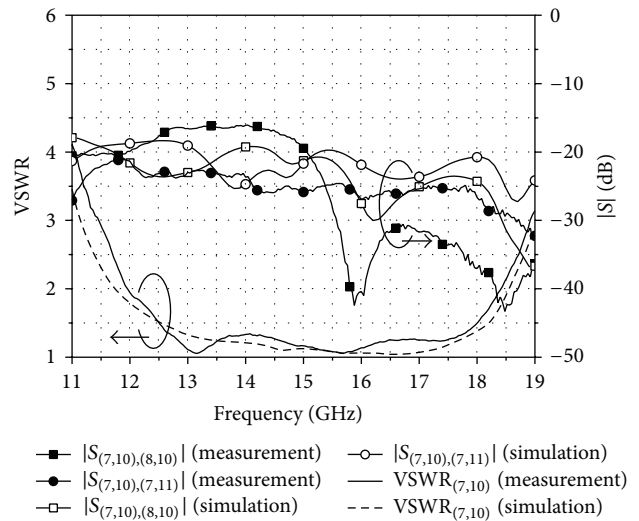


FIGURE 5: Measured and simulated results of VSWR and mutual couplings.

matching performance of the center embedded element in the whole array is estimated by simulating the small size array proposed above.

The radiation patterns of the center embedded element in the operation band are shown in Figure 6. The copolar patterns exhibit good symmetry, and the measured cross-polarization levels are less than  $-17$  dB. Due to the different sizes of the arrays and the ground planes of the simulated model and the actual prototype, there are different oscillating behaviors in the simulated and the measured patterns, especially in the E plane. Figure 7 reveals the gain of

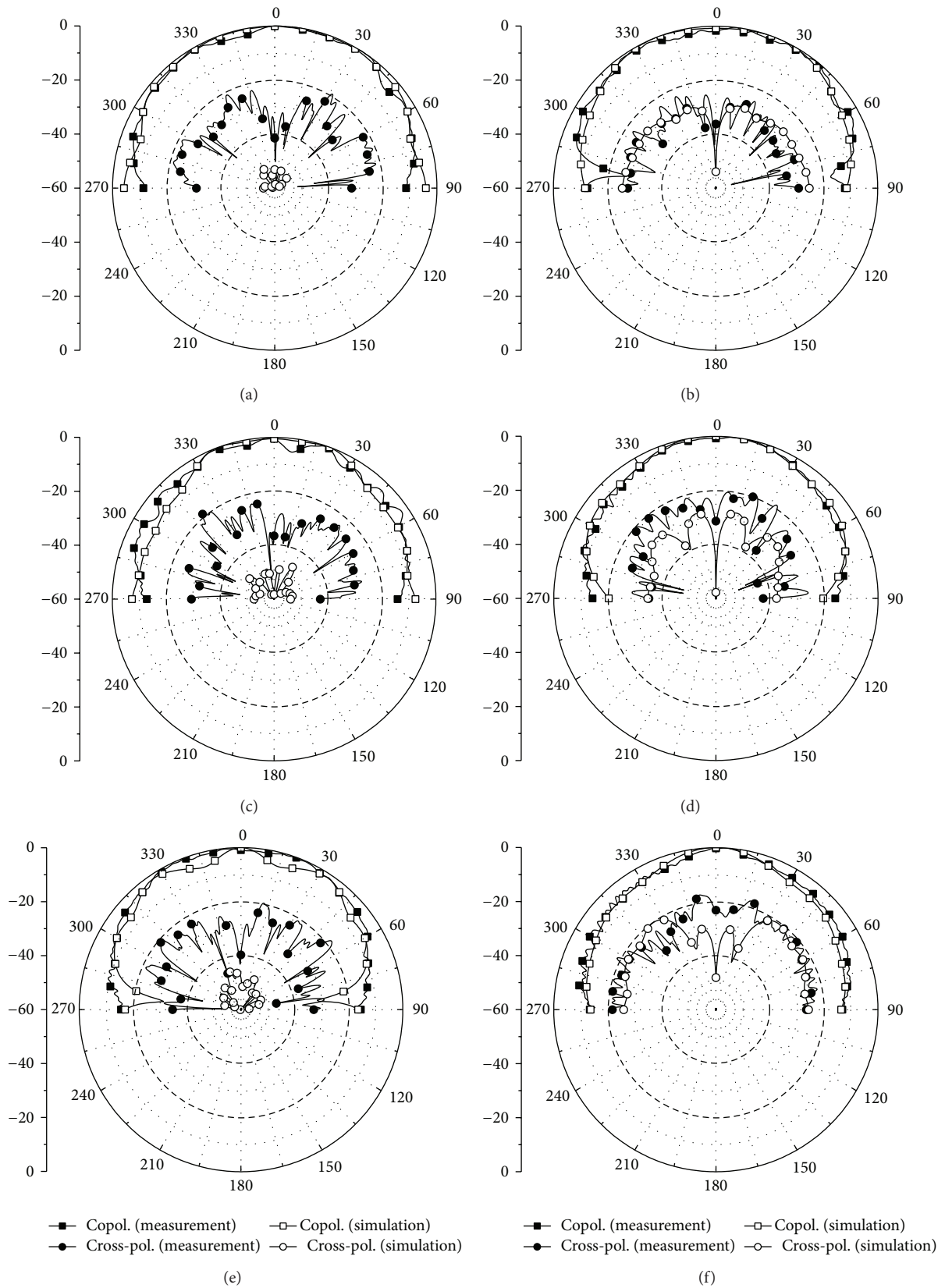


FIGURE 6: Measured and simulated radiation patterns of the central element at different frequencies. (a) E plane at 12 GHz. (b) H plane at 12 GHz. (c) E plane at 15 GHz. (d) H plane at 15 GHz. (e) E plane at 18 GHz. (f) H plane at 18 GHz.

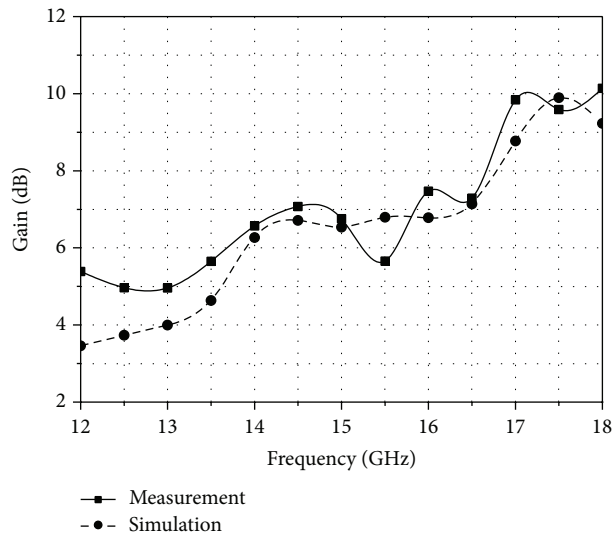


FIGURE 7: Measured and simulated gain of the center embedded element.

the center embedded element in the operation band. As can be seen from the measured and simulated results, the trends of the two curves are comparatively consistent. The measured and the simulated maximum gains are 10.1 dB at 18 GHz and 9.9 dB at 17.5 GHz, separately.

#### 4. Conclusion

A Ku-band spherical conformal phased array antenna has been designed in this paper. The simulated results of  $9 \times 3$  array estimate accurately the matching performances of the embedded element in the actual array. In the meantime, the method provides a nice computing efficiency. The center embedded element of the array exhibits an excellent broadband over 40% (VSWR < 2) and a good radiation performance, which indicates that the method is effective. The array is suitable for being applied to radar and communication systems in aircrafts and other mobile platforms with limited space.

#### Conflict of Interests

The authors declare that there is no conflict of interests regarding the publication of this paper.

#### References

- [1] Z. Sipus, P. Persson, M. Lanne et al., "Structuring research on conformal antennas a European collaboration," in *Proceedings of the 2nd European Conference on Antennas and Propagation (EuCAP '07)*, pp. 1–4, November 2007.
- [2] Q. Wu, M. Liu, and Z.-R. Feng, "A millimeter-wave conformal phased microstrip antenna array on a cylindrical surface," in *Proceedings of the IEEE International Symposium on Antennas and Propagation and USNC/URSI National Radio Science Meeting (APSURSI '08)*, pp. 1–4, July 2008.
- [3] J. C. Brégains, L. Castedo, and F. Ares-Pena, "A WiMAX conformal broad-beam antenna," *IEEE Antennas and Propagation Magazine*, vol. 52, no. 6, pp. 106–109, 2010.
- [4] Y. Zhou, Y. Bayram, F. Du, L. Dai, and J. L. Volakis, "Polymer-carbon nanotube sheets for conformal load bearing antennas," *IEEE Transactions on Antennas and Propagation*, vol. 58, no. 7, pp. 2169–2175, 2010.
- [5] D. T. Pham, H. Subbaraman, M. Y. Chen, X. Xu, and R. T. Chen, "Light weight and conformal 2-bit,  $1 \times 4$  phased-array antenna with CNT-TFT-based phase shifter on a flexible substrate," *IEEE Transactions on Antennas and Propagation*, vol. 59, no. 12, pp. 4553–4558, 2011.
- [6] C.-H. Ahn, Y.-J. Ren, and K. Chang, "A dual-polarized cylindrical conformal array antenna suitable for unmanned aerial vehicles," *International Journal of RF and Microwave Computer-Aided Engineering*, vol. 21, no. 1, pp. 91–98, 2011.
- [7] V. Semkin, M. Kyrö, V.-M. Kolmonen et al., "Conformal antenna array for 60 GHz applications," in *Proceedings of the 7th European Conference on Antennas and Propagation*, pp. 605–608, April 2013.
- [8] P. Knott, "Antenna design and beamforming for a conformal antenna array demonstrator," in *Proceedings of the IEEE Aerospace Conference*, pp. 1–7, March 2006.
- [9] P. Knott, "Design and experimental results of a spherical antenna array for a conformal array demonstrator," in *Proceedings of the 2nd International ITG Conference on Antennas (INICA '07)*, pp. 120–123, March 2007.
- [10] D. Sun, W. Dou, and L. You, "Application of novel cavity-backed proximity-coupled microstrip patch antenna to design broadband conformal phased array," *IEEE Antennas and Wireless Propagation Letters*, vol. 9, pp. 1010–1013, 2010.
- [11] J. K. H. Gamage, B. Holter, I. A. Jensen, K. Husby, and J. Kuhnle, "A wideband conformal antenna array for cognitive radio/MIMO applications," in *Proceedings of 5th European Conference on Antennas and Propagation (EUCAP '11)*, pp. 725–729, April 2011.
- [12] D. Sun, W. Dou, L. You, X. Yan, and R. Shen, "A broadband proximity-coupled stacked microstrip antenna with cavity-backed configuration," *IEEE Antennas and Wireless Propagation Letters*, vol. 10, pp. 1055–1058, 2011.

## Research Article

# Application of Novel Printed Dipole Antenna to Design Broadband Planar Phased Array

Jie Xu and Wenbin Dou

State Key Laboratory of Millimeter Waves, Southeast University, Nanjing 210096, China

Correspondence should be addressed to Jie Xu; [xujie15617953@163.com](mailto:xujie15617953@163.com)

Received 22 October 2013; Accepted 30 December 2013; Published 10 February 2014

Academic Editor: Shaoqiu Xiao

Copyright © 2014 J. Xu and W. Dou. This is an open access article distributed under the Creative Commons Attribution License, which permits unrestricted use, distribution, and reproduction in any medium, provided the original work is properly cited.

A broadband planar phased array consisting of 22 linear printed dipole antennas (PDA) is presented in this paper. The element is designed by a coax probe feeding mechanism with a ground plate configuration. The PDA with two arms placed on both sides of a substrate is realized. The inner conductor of the coaxial cable is connected to the PDA's upper arm, and the outer conductor is connected to the PDA's lower arm, so it eliminates the balun. The impedance bandwidth of the PDA array can be improved by increasing mutual coupling effect between the adjacent array elements. A dielectric layer, which is integrated on the surface of the antenna, is designed and fabricated to improve the impedance bandwidth and to shield the array. The measured results indicate the active VSWR is less than 3 over the frequency range of 4–20 GHz.

## 1. Introduction

In recent years, the demand for broadband phased arrays, which are capable of large scan volumes and suitable for conformal applications, is steadily increasing due to the desire to replace multiple sensors with a single multifunction aperture in a low-profile installation, provide higher data rates, and operate over a wide field of view. In general, the technology of phased array antenna which is based on Vivaldi antenna [1–3] or microstrip patch antenna [4, 5] is mature. Unfortunately, the Vivaldi antenna is not easy to be coplanar, and bandwidth of microstrip patch antenna is not wide.

To solve the problem, a methodology of forming broadband array from tightly-coupled, electrically small elements has been proven by other researchers [6–8]. Harris has demonstrated that the current sheet array (CSA) technology can be applied to a wide range of frequency bands and array sizes. The active VSWR is 3 or better over the entire 2–18 GHz band [9]. Furthermore, Durham invented a new CSA structure to solve the problem [10]. Each dipole antenna element comprises a medial feed portion, and a pair of legs extending outwardly therefrom, and adjacent legs of adjacent dipole antenna elements include respective spaced apart end portions. A respective impedance element is electrically connected between the spaced apart end portions of adjacent

legs of adjacent dipole antenna elements for providing increased capacitive coupling therebetween. However, there is a shortcoming in the structure. Balun is needed to achieve the connection between the element and the coax probe in the antenna structure, which is hard to design when the space between the elements is small.

In order to eliminate the balun, the paper gives another method to form broadband array from tightly coupled elements. The structure is different from the CSA. First, the inner conductor of the coaxial cable is connected to the PDA's upper arm, and the outer conductor is connected to the PDA's lower arm, so eliminate the balun. Second, the implementation of the interelement coupling was accomplished using flat capacitors. In this paper, a planar linear phased array antenna with 22 elements is designed and fabricated. The measured results indicate the active VSWR is less than 3 over the frequency range of 4–20 GHz.

## 2. Antenna Element Design

The structure of the center antenna element in infinite array along  $y$ -direction is shown in Figure 1. The antenna element is composed of a dielectric layer, PDA, a feeding coaxial cable, and a ground plate. The element is designed by a coax probe

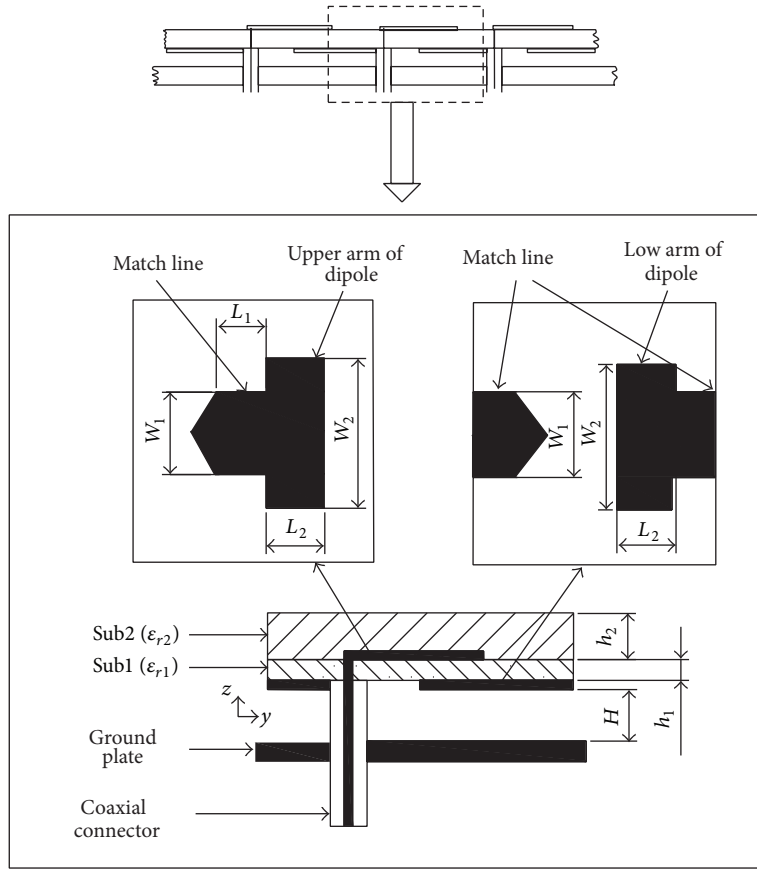


FIGURE 1: Structure of the center antenna element in infinite array.

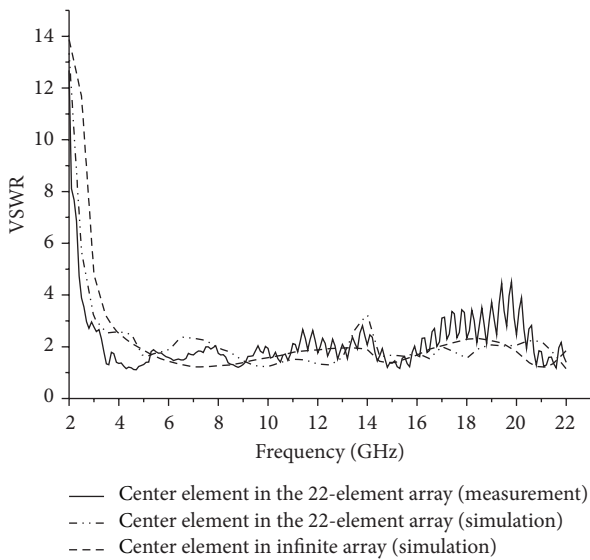
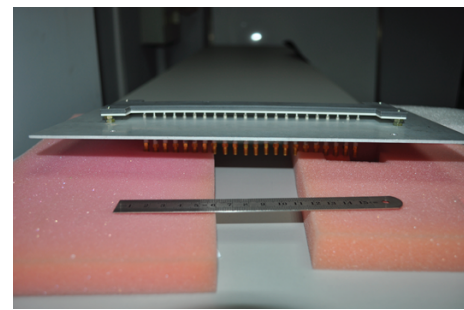
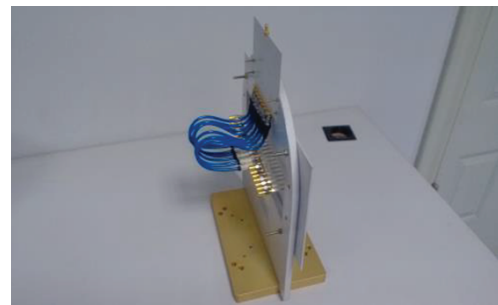


FIGURE 2: Simulated active VSWR of the center element in infinite array.

feeding mechanism with a ground plate configuration. The PDA with two arms placed on both sides of a substrate is realized. The inner conductor of the coaxial cable is



(a)



(b)

FIGURE 3: Prototype planar phased array antenna. (a) Array antenna and (b) Array antenna with the power divider.

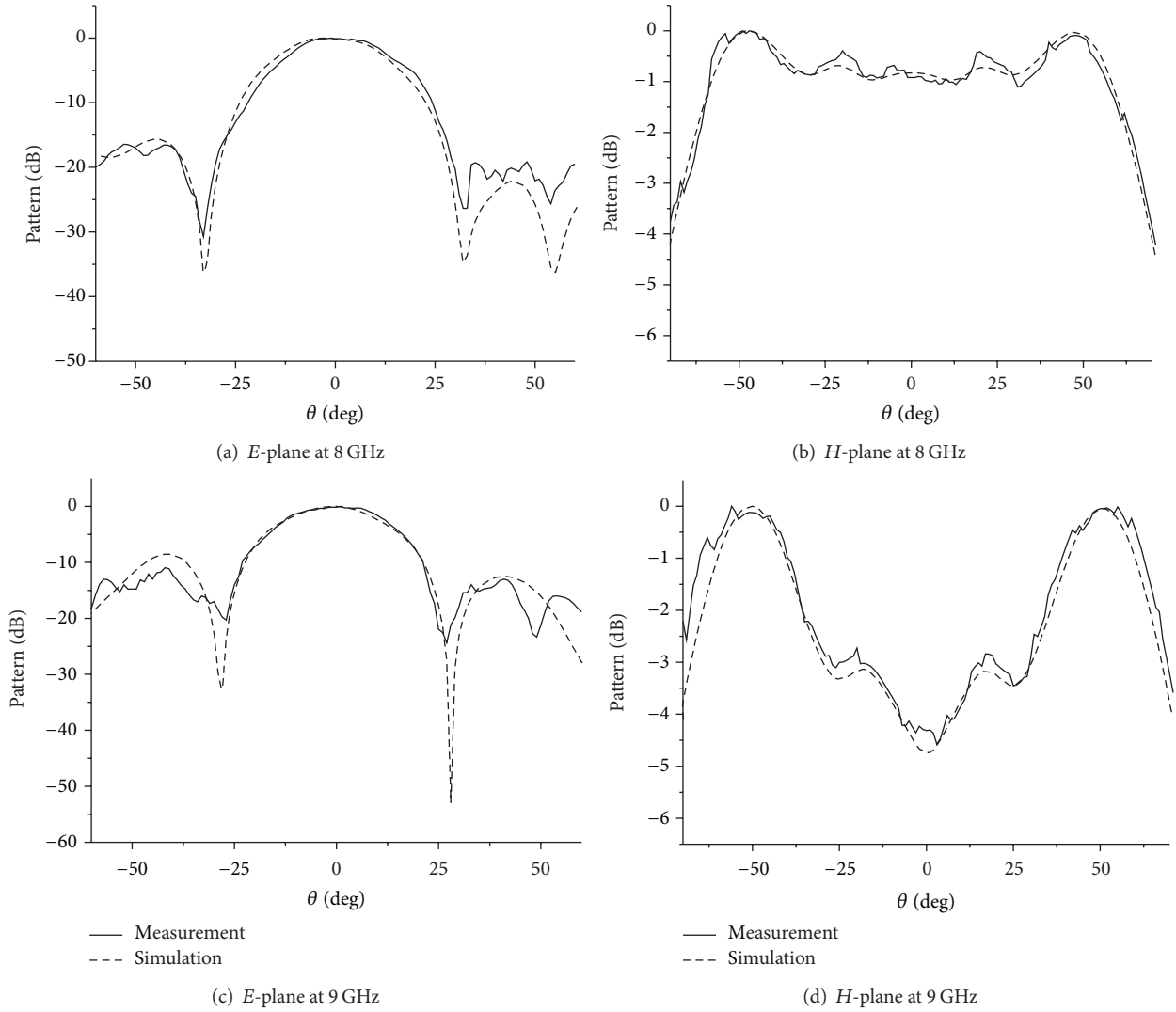


FIGURE 4: Measured and simulated radiation patterns of the center linear 8-element array at different frequencies. (a) *E*-plane at 8 GHz. (b) *H*-plane at 8 GHz. (c) *E*-plane at 9 GHz. (d) *H*-plane at 9 GHz.

connected to the PDA's upper arm, and the outer conductor is connected to the PDA's lower arm, so it eliminates the balun.

The parameters of two substrate layers are  $h_1$ ,  $h_2$ ,  $\epsilon_1$ , and  $\epsilon_2$ , respectively. The size of match line is  $W_1 \times L_1$ , and the size of arm is  $W_2 \times L_2$ . The distance between its PDA and ground plate is  $H$ . The antenna is symmetrically relative to the center antenna. Besides, there is a feed coaxial cable located in the center line of the antenna.

The arms of adjacent array elements constitute flat capacitors, which improve the impedance bandwidth by operating strong capacitive-couple effect. However, there are some differences between this type of elements and the antenna mentioned in [9]. First, the inner conductor of the coaxial cable is connected to the PDA's upper arm, and the outer conductor is connected to the PDA's lower arm, so eliminate the balun. Second, the implementation of the interelement coupling is accomplished using flat capacitors as shown in Figure 1, while the CSA is using interdigital capacitors in [9].

The design way is performed using the periodic moment method (PMM) code, which can analyze infinitely periodic planar structures comprised of thin wires and lumped circuit element surrounded by dielectric layers [10].

To analyze the effects of the mutual coupling on the matching of the center element in infinite array, the active VSWR of the center element within the mutual coupling effect is simulated by HFSS. By adjusting the thickness of Sub2 and the size of the match line, the discontinuity will be compensated, which leads to a nice performance of impedance match. The optimized thickness of Sub2 is 4 mm, and the size of the match line is 8.5 mm  $\times$  1.5 mm. The other parameters are as follows:  $H = 6$  mm,  $h_1 = 1.5$  mm, and  $\epsilon_1 = 3.35$ ,  $h_2 = 4$  mm,  $\epsilon_2 = 2.2$ . The length of the periodical center element in infinite array is 8.7 mm. The array lattice of 8.7 mm allows the main beam to be scanned between  $-30^\circ$  and  $30^\circ$  over the frequency of 4–20 GHz without grating lobes. So the center element can be simulated easily in an infinite

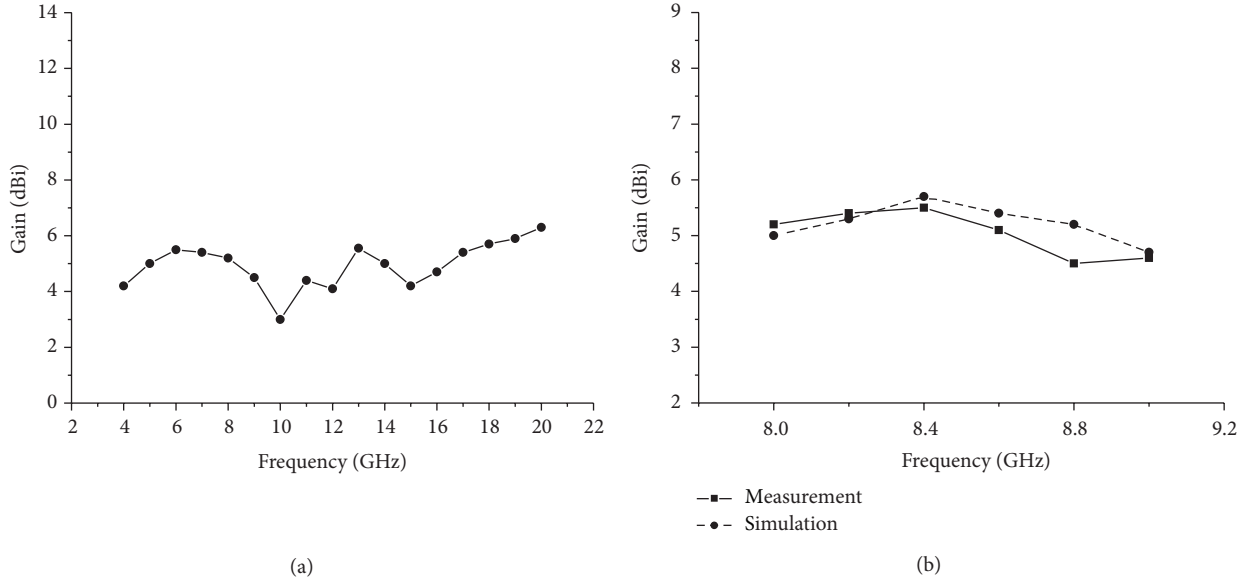


FIGURE 5: (a) Simulated gain of the center 8-element array over the range of 4–20 GHz. (b) Measured and simulated gain of the center 8-element array from 8 GHz to 9 GHz.

environment. As can be seen from the results in Figure 2, the operation bandwidth (the active VSWR < 3) of the center element in infinite array is from 4 to 20 GHz.

### 3. Planar Phased Array Antenna Construction and Measured Results

A prototype planar antenna built up by 22 elements proposed in Section 2 is fabricated along the  $y$ -direction, which is shown in Figure 3. The space between the element is 8.7 mm. Each element is equal, and its parameters are the same as the above antenna element. The measured and simulated active VSWR of the center embedded in 22-element array is shown in Figure 2. The measured bandwidth of VSWR less than 3 is from 4 to 20 GHz. Compared to the simulated result, there is a certain fluctuation in high frequency due to the material of Sub2 (FB4M), which can do well only under 12 GHz. What is more, these results indicate that the matching characteristic of the center element in large array can be estimated through the center element in infinite array, which is advantageous to decrease the difficulty of the model construction and the requirements for the computing devices. The fabrication and construction errors will also result in the deterioration of the antenna performance. The errors are mainly caused by the displacement of the layers in this antenna.

In order to verify the center 8-element linear array's radiation characteristic (the rest element match to the load), 8-way power divider is designed and processed over the frequency range of 8 GHz-9 GHz. The radiation of the center linear array is measured with an 8-way power divider, whose results are shown in Figure 4. The measured results are similar to the simulated results, which present a pretty radiation characteristic at  $f = 8$  GHz and  $f = 9$  GHz. The maximum relative sidelobe level in the  $E$ -plane is  $-16.5$  dB

at  $f = 8$  GHz and  $-12.5$  dB at  $f = 9$  GHz. Because of the bandwidth limit of the power divider (range of 8-9 GHz), the paper gives the simulated gain of the center 8-element array over the range of 4–20 GHz and only gives the measured gain of 8-element array from 8 GHz to 9 GHz, whose results are shown in Figure 5. The simulated gain is comparatively stable in the operation bandwidth, and the maximum value is 6.45 dBi at 20 GHz. The measured gain (8-9 GHz) is similar to the simulated results.

### 4. Conclusions

The novel ground-backed PDA represents a significant departure from the conventional approach to phased array design, which is utilized for the element due to its ability to compensate for the impedance variation with frequency. The structure is different from the CSA. First, the inner conductor of the coaxial cable is connected to the PDA's upper arm, and the outer conductor is connected to the PDA's lower arm, so eliminate the balun. Second, the implementation of the interelement coupling was accomplished using flat capacitors. The measured results indicate that the array has a wide bandwidth and a pretty radiation. It is adapted to build up the planar phased array systems.

### Conflict of Interests

The authors declare that there is no conflict of interests regarding the publication of this paper.

### References

- [1] W. Mohuchy, P. A. Beyerle, and A. B. MacFarland, "4.5:1 bandwidth microstrip notch array measured performance,"

- in *Proceedings of the IEEE Antennas and Propagation Society International Symposium*, pp. 444–447, July 2001.
- [2] M. Kragalott, W. R. Pickles, and M. S. Kluskens, “Design of a 5:1 bandwidth stripline notch array from FDTD analysis,” *IEEE Transactions on Antennas and Propagation*, vol. 48, no. 11, pp. 1733–1740, 2000.
  - [3] R. Thomas Dover, J. Irion II, D. T. McGrathm, and N. Schuneman, “Ultra-wideband arrays Phased Array Systems and Technology,” in *Proceedings of the International Symposium on Phased Array Systems and Technology*, vol. 1, pp. 387–392, 2003.
  - [4] A. M. Ferendeci, “Conformal wide bandwidth antennas and arrays,” in *Proceedings of the 3rd IEEE International Symposium on Microwave, Antenna, Propagation and EMC Technologies for Wireless Communications (MAPE '09)*, pp. k7–k10, October 2009.
  - [5] M. Geissler, F. Woetzel, M. Bottcher et al., “Design and test of an L-band phased array for maritime satcom,” in *Proceedings of the 5th European Conference on Antennas and Propagation (EUCAP '11)*, pp. 2871–2875, April 2011.
  - [6] B. A. Munk, *Frequency Selective Surfaces: Theory and Design*, chapters 3-4, Wiley-Interscience, New York, NY, USA, 2000.
  - [7] J. G. Maloney, M. P. Kesler, P. L. H. Harms, and G. S. Smith, “Fragmented aperture antennas and broadband antenna ground planes,” US Patent 6,323,809, November 2001.
  - [8] S. H. Wi, Y. S. Lee, and J. G. Yook, “Wideband microstrip patch antenna with U-shaped parasitic elements,” *IEEE Transactions on Antennas and Propagation*, vol. 55, no. 4, pp. 1196–1199, 2007.
  - [9] W. A. Davis, J. R. Nealy, G. F. Ricciardi, and W. L. Stutzman, “Techniques for the measurement of the impedance of wide-band balanced antennas,” in *Proceedings of the IEEE Antenna Measurement Techniques Association Symposium*, November 1995.
  - [10] T. E. Durham, G. K. Gothard, A. M. Jones, and J. Kralovec, “Phased array antenna with discrete capacitive coupling and associated methods,” US Patent 6,856,297, February 2005.

## Research Article

# A Stacked Microstrip Antenna Array with Fractal Patches

**Xueyao Ren, Xing Chen, Yufeng Liu, Wei Jin, and Kama Huang**

*College of Electronics and Information, Sichuan University, Chengdu 610064, China*

Correspondence should be addressed to Xing Chen; [chenxingscu@163.com](mailto:chenxingscu@163.com)

Received 22 October 2013; Revised 26 November 2013; Accepted 16 December 2013; Published 9 February 2014

Academic Editor: Xiuping Li

Copyright © 2014 Xueyao Ren et al. This is an open access article distributed under the Creative Commons Attribution License, which permits unrestricted use, distribution, and reproduction in any medium, provided the original work is properly cited.

A novel microstrip antenna array, which utilizes Giuseppe Peano fractal shaped patches as its radiation elements and adopts a two-layer stacked structure for achieving both wideband and high-gain properties, is proposed. Parametric study estimates that the proposed antenna's size can be arbitrarily adjusted by changing the fractal proportion while high aperture efficiency is maintained. Two prototypes with  $2 \times 2$  and  $4 \times 4$  fractal patches, respectively, on each layer are designed, fabricated, and measured. Both simulation and measurement results demonstrate that the proposed antenna possesses encouraging performances of wideband, high directivity, and high aperture efficiency simultaneously; for example, for the two prototypes, their  $S_{11} < -10$  dB impedance bandwidths are 23.49% and 18.49%, respectively; at the working frequency of 5.8 GHz, their directivities are 12.2 dBi and 18.2 dBi, and their corresponding aperture efficiencies are up to 91.0% and 90.5%, respectively.

## 1. Introduction

Directional antennas with high radiation gain are key devices in many practical applications such as the remote wireless communication. Due to their attractive features like low weight, low profile, small size, and being easy to manufacture, employing microstrip antennas to form array is a widely adopted method to design directional antennas with high gain. However, it is well known that microstrip antennas have an intrinsically narrow bandwidth [1], typically a small percent of the center frequency. In view of the explosive growth of the wireless system and the booming demand for a variety of new wireless applications, it is important to design directional antennas with both wideband and high gain to cover a wide frequency range. Indeed, there are countless researches proposed in the literature to design microstrip antennas with high gain or wide bandwidth, but few of them are for both properties together.

To tackle the narrow bandwidth problem of microstrip antennas, various techniques have been proposed. Among them is stacking one or several parasitic layers on a microstrip antenna [2], and various methods have been widely used. For example, the 8-layer stacked patch unit assembly allows for great bandwidth which is more than 50% of the center frequency [3] and the use of high dielectric constant substrate

for the driven layer and low dielectric constant substrate for the superstrate can offer more than 25% on bandwidth [4, 5]. The intrinsic properties of fractal geometries are conducive to the miniaturization of antenna size and realization of multiband or broadband characteristics [6, 7]; L-shape slot loaded broadband patch antenna for enhancing the gain without affecting the broadband impedance matching characteristics [8]; the artificial magnetic conductor structures are employed as the antenna magnetic ground plane for bandwidth enhancement and radiation gain improvement of patch antenna [9]. A dipole antenna with a double electromagnetic band gap (EBG) reflector is presented for wide operating bandwidth and high gain [10]. However, there are some defects in the designs. Some of them have high profile; some of them require special materials and increase the production costs; some of them have complex structures, which increase the difficulty in manufacture. More details are shown in Table 1.

In this work, a novel microstrip antenna array, which employs a two-layer stacked structure and Giuseppe Peano fractal shaped patches for realizing both wideband and high gain properties, is proposed, analyzed, and measured. The remainder of the paper is organized as follows. Section 2 introduces the configuration of the proposed antenna array. A parametric study is presented in Section 3. Simulated and

TABLE 1: Detailed data of the antennas mentioned previously.

Literature number	Number of layer	Number of array elements	Gain (dBi)	Bandwidth	Profile	Manufacture difficulty	Cost
[3]	8	1	7.4	52%	High	Hard	High
[4]	2	4	12.4	25.6%	Low	Easy	High
[5]	2	1	—	35%	Low	Easy	High
[8]	2	1	8.3	20%	Low	Easy	Low
[9]	4	4	15.95	20.45%	High	Hard	High
[10]	4	1	8.5	44.4%	High	Easy	Low

measured properties of two prototypes with  $2 \times 2$  and  $4 \times 4$  fractal patches, respectively, on each layer are given in Section 4. Conclusions are stated in Section 5.

## 2. Antenna Configuration

Fractals are geometrical shapes, which are self-similar, repeating themselves at different scales. With the development of the fractal theory, the nature of fractal geometries has been exploited in many fields of engineering and science, including antenna design. The utilization of fractal geometries in antenna design has led to the evolution of a new class of antennas called fractal shaped antennas.

The Giuseppe Peano fractal is a class of fractal geometries. Its recursive procedure is shown in Figure 1. A Giuseppe Peano starts from a segment with length  $f_2$  and allows its central part with length  $f_1$  to break into two zigzag sections; it is constructed iteratively by growing new zigzag sections that have a specific length ratio  $n = f_2/f_1$  with respect to their parent section.

As depicted in Figure 2, when the Giuseppe Peano fractal is applied to the edges of the square patch, this fractal patch with different sections resonates at different frequencies which together to form a wide working frequency band.

The configuration of the proposed microstrip antenna array is illustrated in Figure 3. This antenna utilizes a two-layer stacked structure, containing a radiation layer and a parasitic layer. Each layer is printed on a PCB (printed circuit board) with relative permittivity  $\epsilon_r = 2.55$  and thickness  $h = 1$  mm. The two layers are separated by air with distance of  $h_z = 3.2$  mm.

On the top surface of the radiation layer, some Giuseppe Peano fractal shaped patches are etched periodically. They act as radiators and are connected to a microstrip corporate feeding network to form an array. On the bottom surface of the parasitic layer, the same patches as that on the radiation layer are also etched. Those patches are parasitic elements for enhancing the bandwidth and gain of the antenna array.

This antenna is fed from a  $50 \Omega$  coaxial connector. The microstrip corporate feeding network consists of a serial of  $T$ -junctions to deliver electromagnetic energy uniformly and multiple-section quarter-wavelength impedance transformers to achieve impedance match and is used to provide equal amplitude and in-phase excitation to all fractal shaped patches.

From Figure 3, we can see that  $L_s = 2 \times (D + L)$ ,  $X = (D - L_0 - W_1)/2Lt = (D + L - W_2)/2$ , and  $L_3 = (D + L) -$

$2 \times (L_1 + L_2) - W_1$ . Finally, the structural parameters of this antenna are optimized by Genetic Algorithm (GA) [11, 12] as follows:  $D = 16.46$  mm,  $L = 14.71$  mm,  $L_r = 16.06$  mm,  $W_1 = 2.27$  mm,  $W_2 = 2.07$  mm,  $W_3 = 1.77$  mm,  $L_0 = 1.38$  mm,  $L_1 = 3.66$  mm,  $L_2 = 8.20$  mm, and  $h_z = 3.19$  mm. The total area of the antenna is  $62.34 \times 62.34$  mm<sup>2</sup>.

## 3. Parametric Study

Here, we investigate the effect of the antenna's parameters on its performance characteristics. In this section, the proposed antenna works at 5.8 GHz, has  $2 \times 2$  and fractal  $4 \times 4$  patches on the radiation and parasitic layers, respectively, and adopts second iteration Giuseppe Peano fractal patches.

*3.1. Effect of the Fractal Proportion.* The Fractal proportion  $n$  is defined as

$$n = \frac{f_2}{f_1}, \quad (1)$$

which can be seen from Figure 1. The greater the  $n$  is, the closer to square patch the Peano fractal radiator is.

The  $2 \times 2$  square patches antenna array which works at the same frequency of 5.8 GHz is illustrated in Figure 4. Each layer is printed on a PCB with relative permittivity  $\epsilon_r = 2.55$  and thickness  $h = 1$  mm, the same as the fractal ones.

The structural parameters of this antenna which is optimized by GA are as follows:  $D = 29.50$  mm,  $L = 15.02$  mm,  $L_r = 17.30$  mm,  $W_1 = 3.72$  mm,  $W_2 = 2.78$  mm,  $W_3 = 2.18$  mm,  $L_0 = 1.52$  mm,  $L_1 = 3.40$  mm,  $L_2 = 13.27$  mm, and  $h_z = 3.48$  mm. The simulated reflection coefficient and simulated directivity are given by Figures 5 and 6, respectively.

It is obvious that the  $S_{11} < -10$  dB impedance bandwidth is about 14.02% (from 5.37 GHz to 6.18 GHz). At its working frequency of 5.8 GHz, the antenna has an input reflection coefficient of  $-22.65$  dB, which estimates that a good impedance match has been achieved.

Different  $2 \times 2$  array antennas of different fractal proportion ( $n = 2, n = 2.5, n = 3, n = 3.5, n = 4, \text{ and } n = 4.5$ ) which are also working at 5.8 GHz are optimized by GA. Figure 7 reveals the simulated reflection coefficient of different fractal proportion antenna arrays and Figure 8 reveals the simulated directivity.

From Table 2, one can observe that the fractal proportion has a great influence on the antenna performance. As fractal proportion  $n$  increases, the aperture area of the proposed

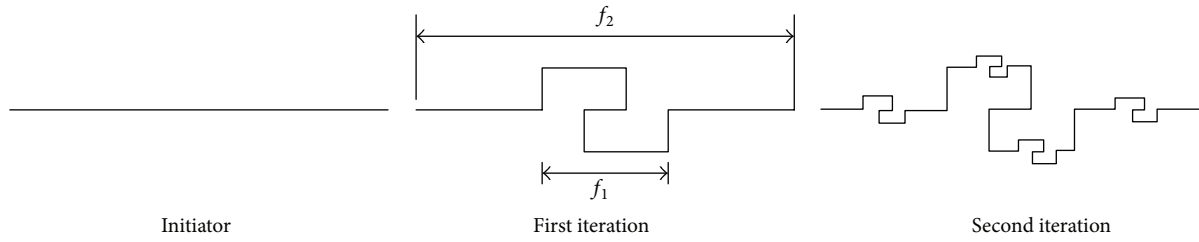


FIGURE 1: The recursive procedure of the Giuseppe Peano fractal.

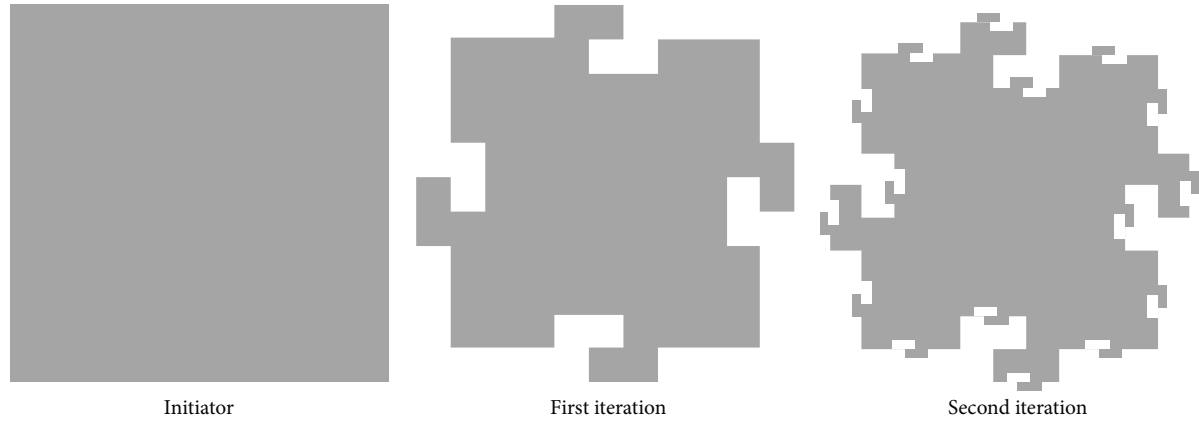
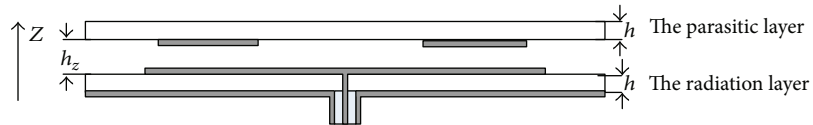
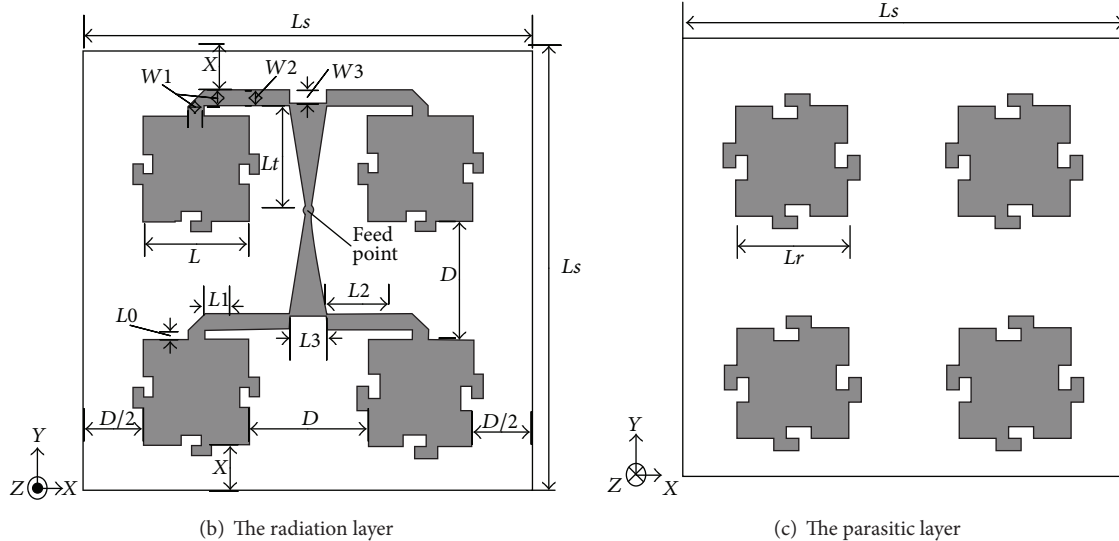


FIGURE 2: The Giuseppe Peano fractal patch.



■ Metal  
□ Dielectric

(a) The cross-section diagram



(b) The radiation layer

(c) The parasitic layer

FIGURE 3: Configuration of the proposed microstrip antenna array.

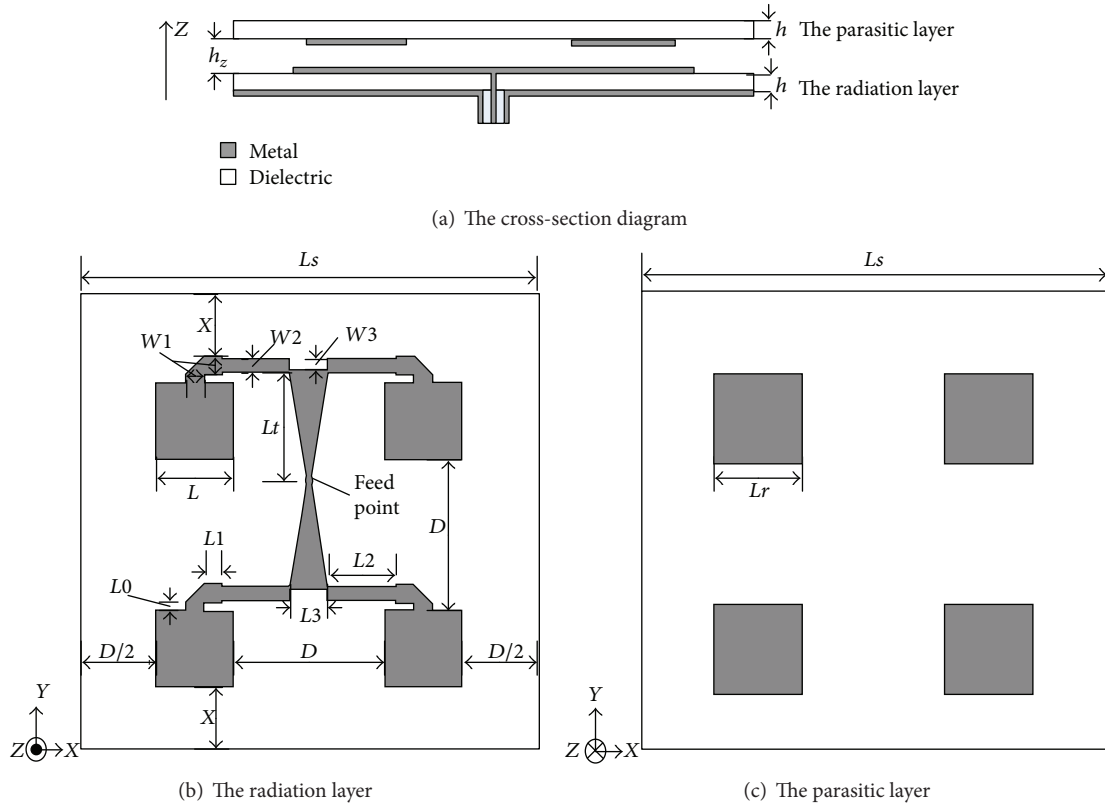


FIGURE 4: The configuration of the two-layer square patches  $2 \times 2$  antenna array.

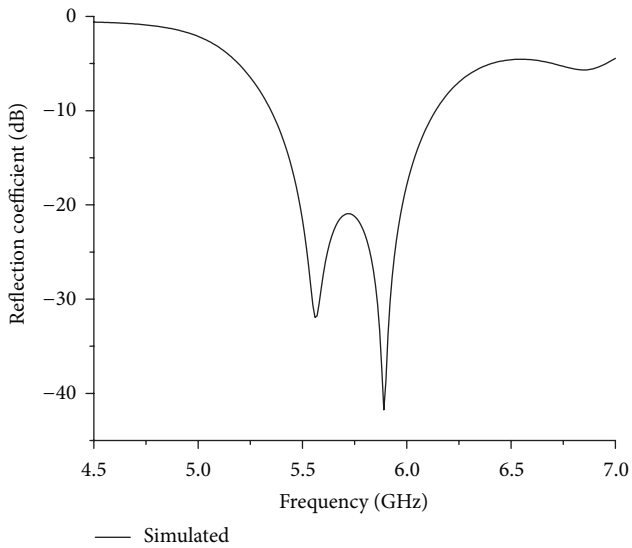


FIGURE 5: The simulated reflection coefficient of the square antenna array.

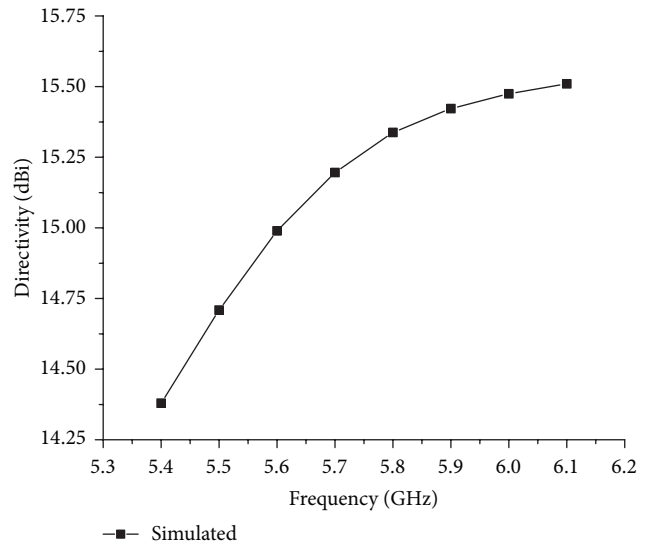


FIGURE 6: The simulated directivity as a function of frequency for the square patches antenna array.

antenna must increase for maintaining the same working frequency of 5.8 GHz. When the fractal proportion  $n = 3.5$ , the  $S_{11} < -10$  dB impedance bandwidth reaches 23.49% versus 14.02% of the square antenna array working at the same

frequency, the aperture area of proposed antenna is only 49% of the square patches antenna array's.

Another interesting observation worthwhile pointing out is the attainable aperture efficiency calculated only by the

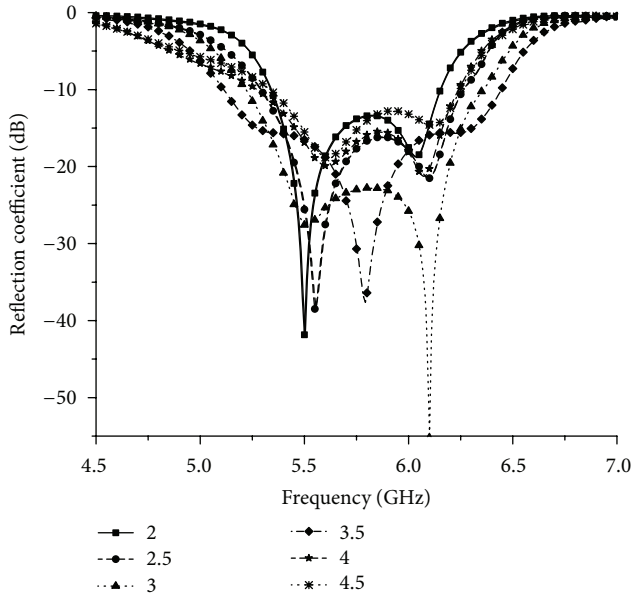


FIGURE 7: The simulated reflection coefficient of the different fractal proportion.

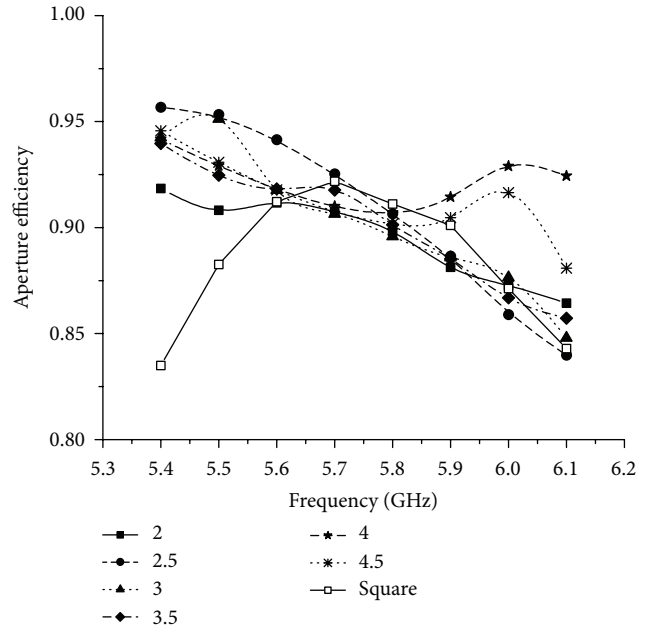


FIGURE 9: The simulated aperture efficiency of the different fractal proportion antenna array.

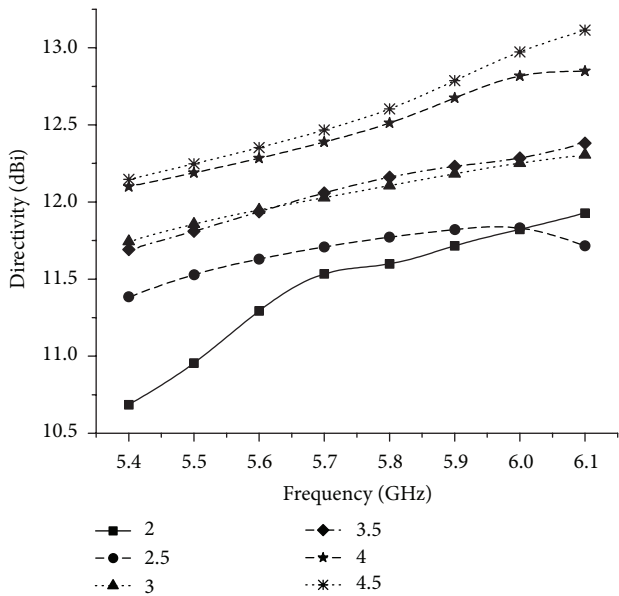


FIGURE 8: The simulated directivity as a function of frequency for the different fractal proportion.

directivity, shown in Figure 9. The vast majority of them are more than 85%. The average aperture efficiency (from 5.4 GHz to 6.1 GHz) is shown in Table 3.

Table 3 demonstrates that the average aperture efficiency of the Peano fractal antenna array is higher than that of the square antenna in the same working band. The maximum value of average aperture efficiency is obtained when the fractal proportion  $n = 4$ .

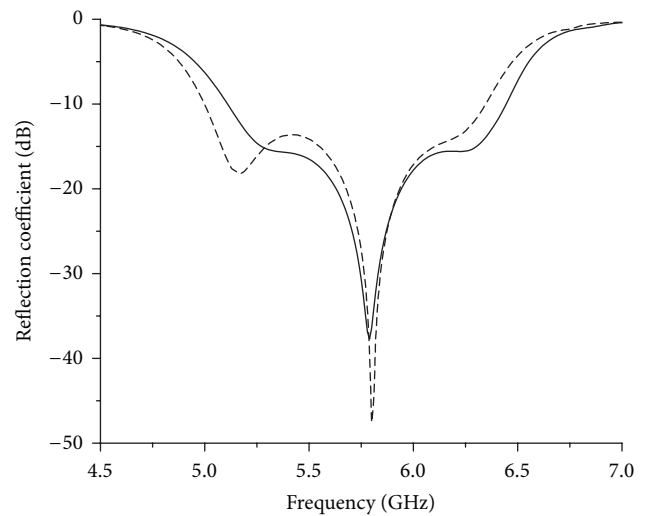


FIGURE 10: Comparison of the simulated reflection coefficient of the 1st iteration and 2nd iteration.

**3.2. Effect of Fractal Iteration.** First and second iteration are relatively applied to the edges of the square patch. All the parameters of the second iteration antenna array are set to be the same as the first one. The comparison of the reflection coefficient of these two antennas is drawn in Figure 10.

One can observe that the impedance bandwidth for  $S_{11} < -10$  dB is 24.18% (from 4.98 GHz to 6.35 GHz), which is much wider than that of square patches antenna array and slightly larger than that achieved in first iteration of the fractal patches antenna array. As the iteration of fractal geometry increases,

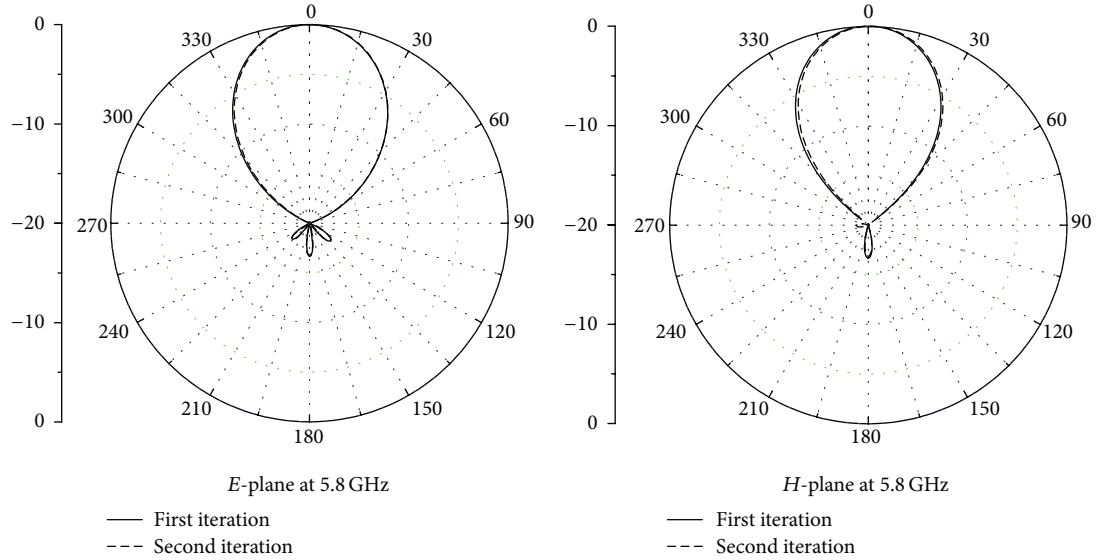


FIGURE 11: Comparison of the radiation patterns of the fractal iterations, 1st and 2nd.

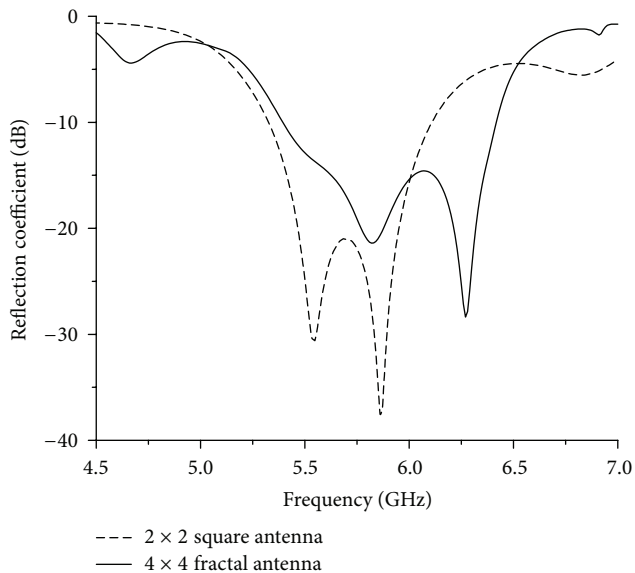


FIGURE 12: Comparison of the simulated reflection coefficient of the  $2 \times 2$  square patch antenna and the  $4 \times 4$  Giuseppe Peano fractal antenna.

its resonance frequency decreases, which may lead to an effective antenna miniaturization. However, for iterations higher than the second iteration, the antenna design becomes quite complicated and its fabrication becomes difficult. The comparison of simulated radiation patterns in the  $E$ -plane and  $H$ -plane of these two antennas is shown in Figure 11.

The comparison indicates that the influence of radiation patterns that comes from the fractal iteration is almost negligible.

TABLE 2: Details of different antennas.

$n$	$f_L$ (GHz)	$f_H$ (GHz)	$f_M$ (GHz)	$f_{\%}$	$L_s$ (cm)
2	5.33	6.23	5.78	15.57%	56.68
2.5	5.29	6.27	5.78	16.98%	59.43
3	5.21	6.37	5.79	20.03%	62.12
3.5	5.07	6.42	5.78	23.49%	62.34
4	5.28	6.30	5.79	17.62%	64.90
4.5	5.33	6.25	5.79	15.89%	65.40
Square	5.37	6.18	5.78	14.02%	89

TABLE 3

Fractal proportion $n$	Average aperture efficiency
2	89.53%
2.5	90.86%
3	90.30%
3.5	91%
4	92.18%
4.5	91.32%
Square	88.48%

**3.3. Effect of Array Elements Number.** In this part, a proposed antenna with  $4 \times 4$  Giuseppe Peano fractal radiated elements and working at 5.8 GHz is also optimized by GA.

Figure 12 compares the simulated reflection coefficient of the  $2 \times 2$  square patch antenna and that of the  $4 \times 4$  Giuseppe Peano fractal antenna. As known to all, when the number of array elements increases, the impedance bandwidth of the antenna array decreases because of the mutual coupling between the array elements [13, 14]. Although the element number of fractal antenna array is four times that in the square antenna, the impedance bandwidth for  $S_{11} < -10$  dB

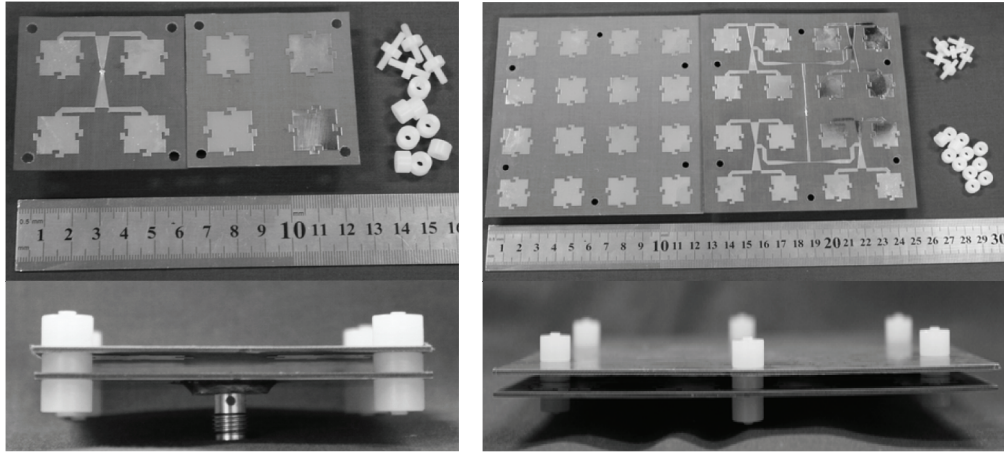


FIGURE 13: The both layers of the fabricated prototype antennas.

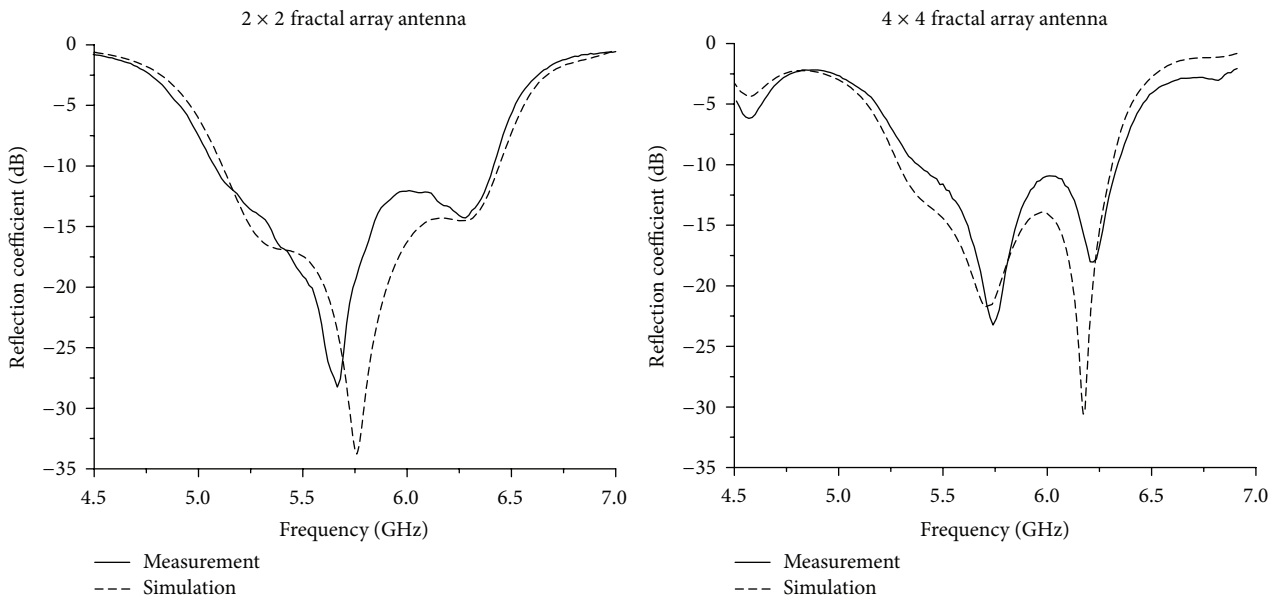


FIGURE 14: The measured and simulated reflection coefficients of the prototype antenna.

is 18.43% (from 5.32 GHz to 6.40 GHz), which is much wider than that of square patches antenna array introduced previously.

#### 4. Experimental Results

Two prototype antennas with  $2 \times 2$  and  $4 \times 4$  radiations elements, respectively, have been fabricated and measured, which are shown in Figure 13. Some glass sticks with a diameter of 5 mm are used for propping them up.

Figure 14 is the comparison of the measured and reflection coefficient of the prototype antennas, respectively.

The measured and simulated results are in good agreement. From the measurement, the  $S_{11} < -10$  dB impedance bandwidth of the antenna is about 23.49% (from 5.07 GHz to 6.42 GHz) for  $2 \times 2$  fractal array antenna and 18.19% (from 5.34 GHz to 6.41 GHz) for  $4 \times 4$  fractal array antenna,

respectively. At its working frequency of 5.8 GHz, the antenna has an input reflection coefficient of  $-16.95$  dB and  $-18.81$  dB, respectively, which estimates that a good impedance match has been achieved. Figures 15 and 16 depict the simulated and the measured radiation patterns at different frequencies within the effective frequency band.

#### 5. Conclusion

A novel Giuseppe Peano fractal antenna array is presented. Structural parameters of the proposed antenna are optimized by a parallel GA to achieve both high gain and wideband properties over a desirable frequency band with the center of 5.8 GHz. Two prototype antennas were fabricated and measured. The measurement results and the simulation results agree well and show that the optimized antenna array possess some encouraging properties.

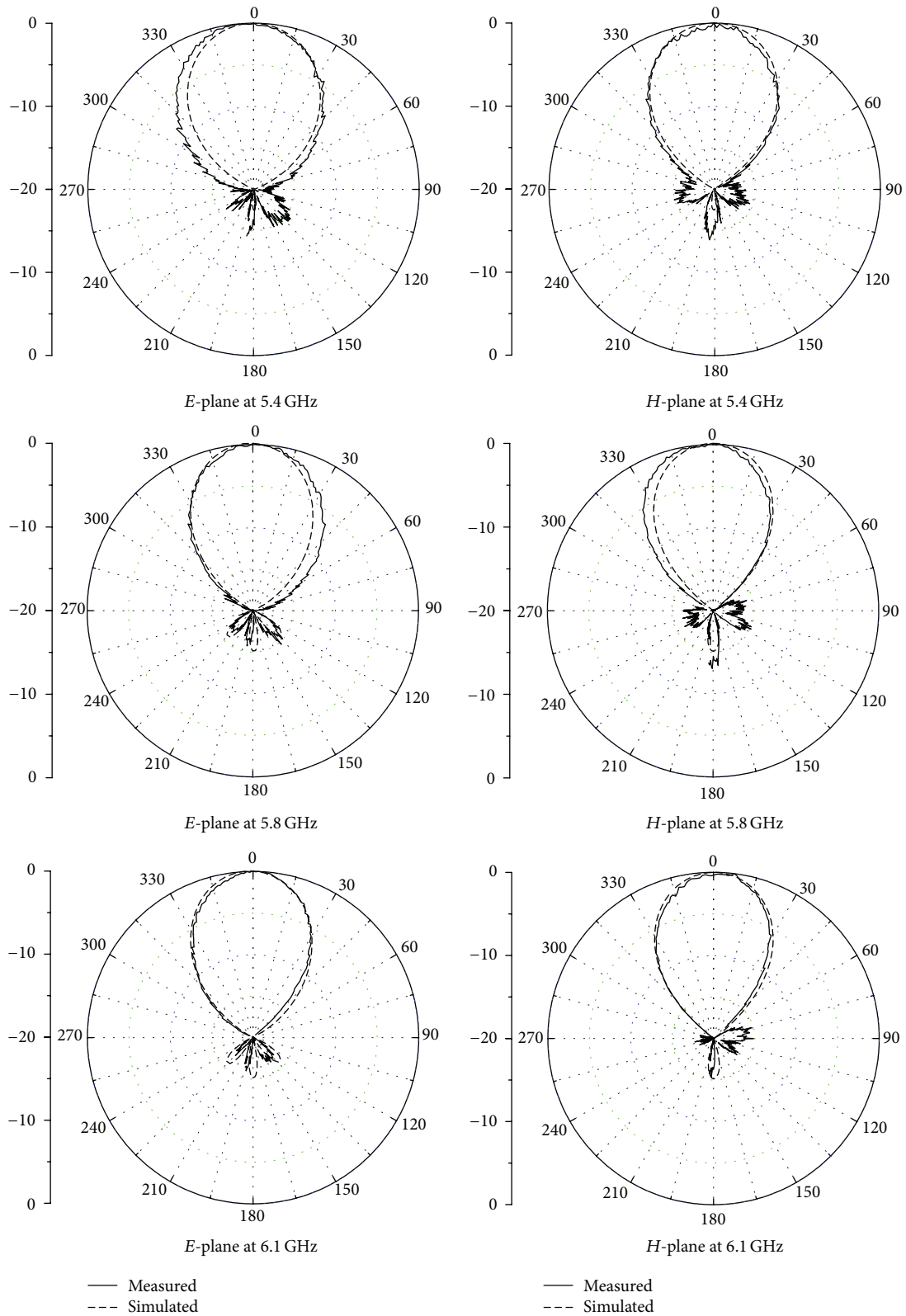


FIGURE 15: Measured and simulated radiation patterns on the *E*-plane and the *H*-plane at different frequencies of the  $2 \times 2$  fractal antenna array.

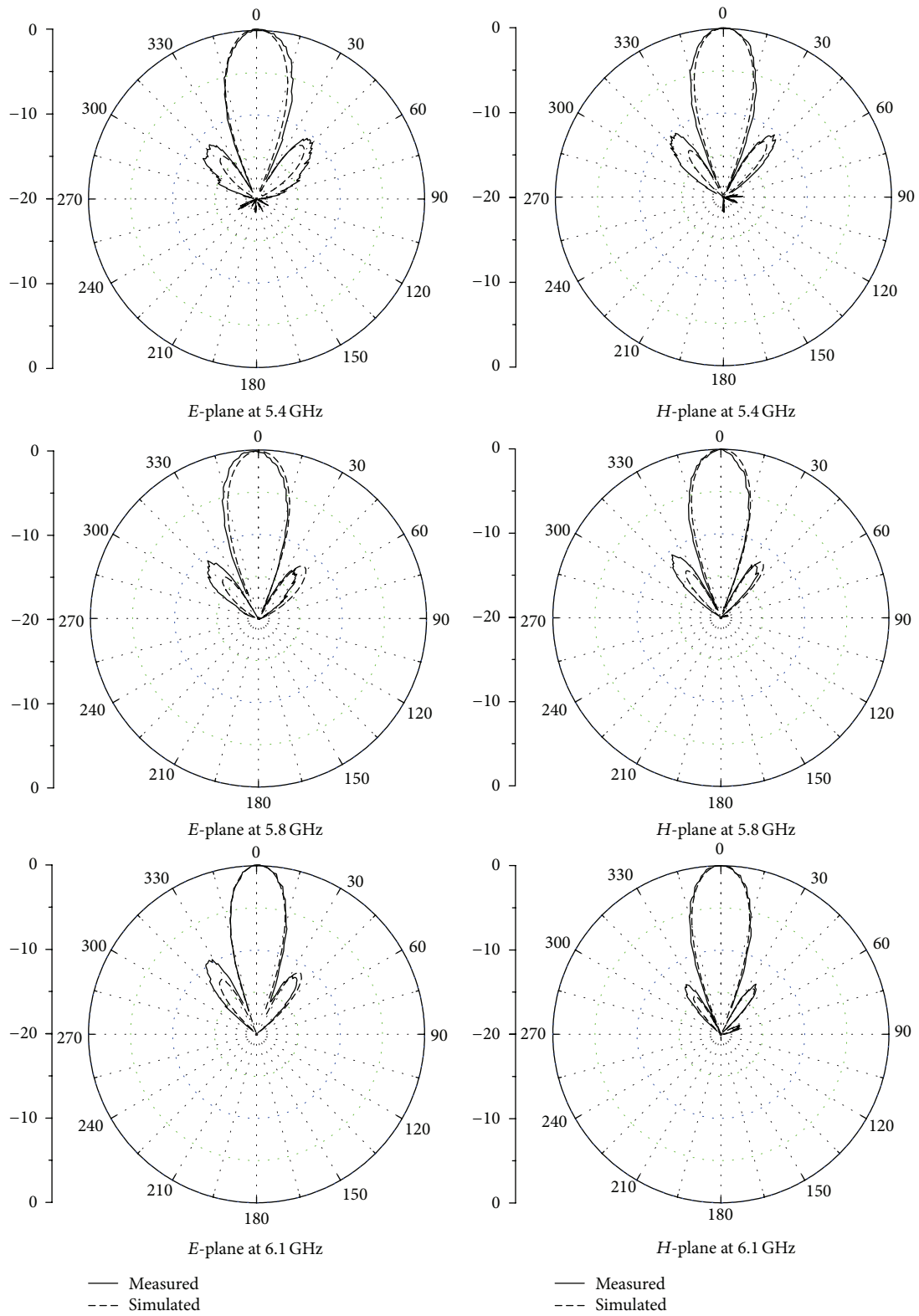


FIGURE 16: Measured and simulated radiation patterns on the *E*-plane and the *H*-plane at different frequencies of the  $4 \times 4$  fractal antenna array.

By comparing the proposed antenna with the square patches one, the important conclusions resulting from this study are as follows.

- (1) The Giuseppe Peano fractal configuration provides extremely high flexibility to achieve broadband performance while maintaining higher average aperture efficiency in the operating frequency band. Fractal proportion can be selected according to design requirements; for example, if the impedance bandwidth is a major consideration in design, the fractal proportion  $n$  close to 3.5 is comparatively suitable; if the design requires making full use of the high aperture efficiency to maintain the high directivity over the bandwidth, the value  $n$  approximating 4 is more reasonable.
- (2) In the case of the same number of array elements and the working frequency, the Giuseppe Peano fractal antenna array can more effectively reduce the required aperture area (reduce 51%) than the traditional square patches antenna array. As the iteration of fractal geometry increases, its resonance frequency decreases; this may lead to an effective miniaturization of antenna. At the same time, the radiation pattern is essentially unchanged.
- (3) Although the element number of fractal antenna array is four times that in square antenna, the impedance bandwidth for  $S_{11} < -10$  dB is 18.43% (from 5.32 GHz to 6.40 GHz), which is still much wider than that of square array antennas introduced previously (which is about 14.02% from 5.37 GHz to 6.18 GHz). This clearly showed that the introduction of fractal radiation unit can reduce the mutual coupling between the antenna elements.

Given the conclusion above, the merits of wideband and high aperture efficiency make the proposed antenna a good candidate for various applications.

## Conflict of Interests

The authors declare that there is no conflict of interests regarding the publication of this paper.

## References

- [1] D. M. Pozar, "Microstrip antennas," *Proceedings of the IEEE*, vol. 80, no. 1, pp. 79–91, 1992.
- [2] L. Xiuping, A. Yi, X. Xiaowen, and L. Xin, "Design of multi-layer microstrip antenna and arrays," *Journal of Electronics and Information Technology*, vol. 24, no. 8, 2002.
- [3] K. Ghorbani and R. B. Waterhouse, "Dual polarized wide-band aperture stacked patch antennas," *IEEE Transactions on Antennas and Propagation*, vol. 52, no. 8, pp. 2171–2175, 2004.
- [4] K. L. Chung and A. S. Mohan, "A circularly polarized stacked electromagnetically coupled patch antenna," *IEEE Transactions on Antennas and Propagation*, vol. 52, no. 5, pp. 1365–1369, 2004.
- [5] A. B. Nandgaonkar and S. B. Deosarkar, "Design of high gain two-layer electromagnetically coupled patch antenna in the ISM band," in *2007 International Conference on Electromagnetics in Advanced Applications (ICEAA '07)*, pp. 547–550, Torino, Italy, September 2007.
- [6] J. P. Gianvittorio and Y. Rahmat-Samii, "Fractal antennas: a novel antenna miniaturization technique, and applications," *IEEE Antennas and Propagation Magazine*, vol. 44, no. 1, pp. 20–36, 2002.
- [7] D. H. Werner and S. Ganguly, "An overview of fractal antenna engineering research," *IEEE Antennas and Propagation Magazine*, vol. 45, no. 1, pp. 38–57, 2003.
- [8] H. Parikh, S. Pandey, and K. Modh, "Wideband and high gain stacked microstrip antenna for Ku band application," in *Proceedings of the Nirma University International Conference on Engineering (NUICONE '12)*, pp. 1–5, 2012.
- [9] W. Yang, H. Wang, W. Che, and J. A. Wang, "Wideband and high-gain edge-fed patch antenna and array using artificial magnetic conductor structures," *IEEE Antennas and Propagation Letters*, vol. 12, pp. 769–772, 2013.
- [10] P. Y. Lau, K. K. O. Yung, and Z. N. Chen, "A wideband high gain double EBG reflector antenna," in *Proceedings of the 8th International Conference on Information, Communications and Signal Processing (ICICS '11)*, pp. 1–4, Singapore, December 2011.
- [11] X. Chen, K. Huang, and X.-B. Xu, "Automated design of a three-dimensional fishbone antenna using parallel genetic algorithm and NEC," *IEEE Antennas and Wireless Propagation Letters*, vol. 4, no. 1, pp. 425–428, 2005.
- [12] X. Chen, K. Huang, and X. B. Xu, "Microwave imaging of buried inhomogeneous objects using parallel genetic algorithm combined with FDTD method," *Progress in Electromagnetics Research*, vol. 53, pp. 283–298.
- [13] S. Edelberg and A. A. Oliner, "Mutual coupling effects in large antenna arrays," *IRE Transactions on Antennas and Propagation*, vol. 8, no. 3, pp. 286–297, 1960.
- [14] D. M. Pozar, "Input impedance and mutual coupling of rectangular microstrip antennas," *IEEE Transactions on Antennas and Propagation*, vol. 30, no. 6, pp. 1191–1196, 1982.